The Detection and Quantification of Nonyl Phenyl Ethoxylate Surfactant on Paracetamol Single Crystal Surfaces

Benjamin Thomas Tayler-Barrett

Submitted in accordance with the requirements for the degree of

Integrated

Master of Science

and

Doctor of Philosophy

The University of Leeds

School of Chemical and Process Engineering

Centre for Doctoral Training in Complex Particulate Products and Processes

September 2020

Intellectual Property and Copyright Declaration

The candidate confirms that the work submitted is his/her own and that appropriate credit has been given where reference has been made to the work of others.

The right of Benjamin Thomas Tayler-Barrett to be identified as Author of this work has been asserted by him in accordance with the Copyright, Designs and Patents Act 1988.

Creative Commons Attribution-NonCommercial-ShareAlike 4.0 International Public License

By exercising the Licensed Rights (defined below), You accept and agree to be bound by the terms and conditions of this Creative Commons Attribution-NonCommercial-ShareAlike 4.0 International Public License ("Public License"). To the extent this Public License may be interpreted as a contract, You are granted the Licensed Rights in consideration of Your acceptance of these terms and conditions, and the Licensor grants You such rights in consideration of benefits the Licensor receives from making the Licensed Material available under these terms and conditions.

Section 1 – Definitions.

Adapted Material means material subject to Copyright and Similar Rights that is derived from or based upon the Licensed Material and in which the Licensed Material is translated, altered, arranged, transformed, or otherwise modified in a manner requiring permission under the Copyright and Similar Rights held by the Licensor. For purposes of this Public License, where the Licensed Material is a musical work, performance, or sound recording, Adapted Material is always produced where the Licensed Material is synched in timed relation with a moving image. Adapter's License means the license You apply to Your Copyright and Similar Rights in Your contributions to Adapted Material in accordance with the terms and conditions of this Public License. BY-NC-SA Compatible License means a license listed at creativecommons.org/compatiblelicenses, approved by Creative Commons as essentially the equivalent of this Public License. Copyright and Similar Rights means copyright and/or similar rights closely related to copyright including, without limitation, performance, broadcast, sound recording, and Sui Generis Database Rights, without regard to how the rights are labeled or categorized. For purposes of this Public License, the rights specified in Section 2(b)(1)-(2) are not Copyright and Similar Rights. Effective Technological Measures means those measures that, in the absence of proper authority, may not be circumvented under laws fulfilling obligations under Article 11 of the WIPO Copyright Treaty adopted on December 20, 1996, and/or similar international agreements. Exceptions and Limitations means fair use, fair dealing, and/or any other exception or limitation to Copyright and Similar Rights that applies to Your use of the Licensed Material. License Elements means the license attributes listed in the name of a Creative Commons Public License. The License Elements of this Public License are Attribution, NonCommercial, and ShareAlike. Licensed Material means the artistic or literary work, database, or other material to which the Licensor applied this Public License. Licensed Rights means the rights granted to You subject to the terms and conditions of this Public License, which are limited to all Copyright and Similar Rights that apply to Your use of the Licensed Material and that the Licensor has authority to license. Licensor means the individual(s) or entity(ies) granting rights under

this Public License. NonCommercial means not primarily intended for or directed towards commercial advantage or monetary compensation. For purposes of this Public License, the exchange of the Licensed Material for other material subject to Copyright and Similar Rights by digital file-sharing or similar means is NonCommercial provided there is no payment of monetary compensation in connection with the exchange. Share means to provide material to the public by any means or process that requires permission under the Licensed Rights, such as reproduction, public display, public performance, distribution, dissemination, communication, or importation, and to make material available to the public including in ways that members of the public may access the material from a place and at a time individually chosen by them. Sui Generis Database Rights means rights other than copyright resulting from Directive 96/9/EC of the European Parliament and of the Council of 11 March 1996 on the legal protection of databases, as amended and/or succeeded, as well as other essentially equivalent rights anywhere in the world. You means the individual or entity exercising the Licensed Rights under this Public License. Your has a corresponding meaning.

Section 2 – Scope.

License grant. Subject to the terms and conditions of this Public License, the Licensor hereby grants You a worldwide, royalty-free, non-sublicensable, non-exclusive, irrevocable license to exercise the Licensed Rights in the Licensed Material to: reproduce and Share the Licensed Material, in whole or in part, for NonCommercial purposes only; and produce, reproduce, and Share Adapted Material for NonCommercial purposes only. Exceptions and Limitations. For the avoidance of doubt, where Exceptions and Limitations apply to Your use, this Public License does not apply, and You do not need to comply with its terms and conditions. Term. The term of this Public License is specified in Section 6(a). Media and formats; technical modifications allowed. The Licensor authorizes You to exercise the Licensed Rights in all media and formats whether now known or hereafter created, and to make technical modifications necessary to do so. The Licensor waives and/or agrees not to assert any right or authority to forbid You from making technical modifications necessary to exercise the Licensed Rights, including technical modifications necessary to circumvent Effective Technological Measures. For purposes of this Public License, simply making modifications authorized by this Section 2(a)(4) never produces Adapted Material. Downstream recipients. Offer from the Licensor – Licensed Material. Every recipient of the Licensed Material automatically receives an offer from the Licensor to exercise the Licensed Rights under the terms and conditions of this Public License. Additional offer from the Licensor – Adapted Material. Every recipient of Adapted Material from You automatically receives an offer from the Licensor to exercise the Licensed Rights in the Adapted Material under the conditions of the Adapter's License You apply. No downstream restrictions. You may not offer or impose any additional or different terms or conditions on, or apply any Effective Technological

Measures to, the Licensed Material if doing so restricts exercise of the Licensed Rights by any recipient of the Licensed Material. No endorsement. Nothing in this Public License constitutes or may be construed as permission to assert or imply that You are, or that Your use of the Licensed Material is, connected with, or sponsored, endorsed, or granted official status by, the Licensor or others designated to receive attribution as provided in Section 3(a)(1)(A)(i).

Other rights. Moral rights, such as the right of integrity, are not licensed under this Public License, nor are publicity, privacy, and/or other similar personality rights; however, to the extent possible, the Licensor waives and/or agrees not to assert any such rights held by the Licensor to the limited extent necessary to allow You to exercise the Licensed Rights, but not otherwise. Patent and trademark rights are not licensed under this Public License. To the extent possible, the Licensor waives any right to collect royalties from You for the exercise of the Licensed Rights, whether directly or through a collecting society under any voluntary or waivable statutory or compulsory licensing scheme. In all other cases the Licensor expressly reserves any right to collect such royalties, including when the Licensed Material is used other than for NonCommercial purposes.

Section 3 – License Conditions.

Your exercise of the Licensed Rights is expressly made subject to the following conditions. Attribution.

If You Share the Licensed Material (including in modified form), You must: retain the following if it is supplied by the Licensor with the Licensed Material: identification of the creator(s) of the Licensed Material and any others designated to receive attribution, in any reasonable manner requested by the Licensor (including by pseudonym if designated); a copyright notice; a notice that refers to this Public License; a notice that refers to the disclaimer of warranties; a URI or hyperlink to the Licensed Material to the extent reasonably practicable; indicate if You modified the Licensed Material and retain an indication of any previous modifications; and indicate the Licensed Material is licensed under this Public License, and include the text of, or the URI or hyperlink to, this Public License. You may satisfy the conditions in Section 3(a)(1) in any reasonable manner based on the medium, means, and context in which You Share the Licensed Material. For example, it may be reasonable to satisfy the conditions by providing a URI or hyperlink to a resource that includes the required information. If requested by the Licensor, You must remove any of the information required by Section 3(a)(1)(A) to the extent reasonably practicable. ShareAlike.

In addition to the conditions in Section 3(a), if You Share Adapted Material You produce, the following conditions also apply. The Adapter's License You apply must be a Creative Commons license with the same License Elements, this version or later, or a BY-NC-SA Compatible License. You must include the text of, or the URI or hyperlink to, the Adapter's License You apply. You may satisfy this condition in any reasonable manner based on the medium, means, and context in which You Share Adapted Material. You may not offer or impose any additional or different terms or conditions on, or apply any Effective Technological Measures to, Adapted Material that restrict exercise of the rights granted under the Adapter's License You apply.

Section 4 – Sui Generis Database Rights.

Where the Licensed Rights include Sui Generis Database Rights that apply to Your use of the Licensed Material:

for the avoidance of doubt, Section 2(a)(1) grants You the right to extract, reuse, reproduce, and Share all or a substantial portion of the contents of the database for NonCommercial purposes only; if You include all or a substantial portion of the database contents in a database in which You have Sui Generis Database Rights, then the database in which You have Sui Generis Database Rights (but not its individual contents) is Adapted Material, including for purposes of Section 3(b); and You must comply with the conditions in Section 3(a) if You Share all or a substantial portion of the contents of the database.

For the avoidance of doubt, this Section 4 supplements and does not replace Your obligations under this Public License where the Licensed Rights include other Copyright and Similar Rights.

Section 5 – Disclaimer of Warranties and Limitation of Liability.

Unless otherwise separately undertaken by the Licensor, to the extent possible, the Licensor offers the Licensed Material as-is and as-available, and makes no representations or warranties of any kind concerning the Licensed Material, whether express, implied, statutory, or other. This includes, without limitation, warranties of title, merchantability, fitness for a particular purpose, non-infringement, absence of latent or other defects, accuracy, or the presence or absence of errors, whether or not known or discoverable. Where disclaimers of warranties are not allowed in full or in part, this disclaimer may not apply to You. To the extent possible, in no event will the Licensor be liable to You on any legal theory (including, without limitation, negligence) or otherwise for any direct, special, indirect, incidental, consequential, punitive, exemplary, or other losses, costs, expenses, or damages arising out of this Public License or use of the Licensed Material, even if the Licensor has been advised of the possibility of such losses, costs, expenses, or damages. Where a limitation of liability is not allowed in full or in part, this limitation may not apply to You.

The disclaimer of warranties and limitation of liability provided above shall be interpreted in a manner that, to the extent possible, most closely approximates an absolute disclaimer and waiver of all liability.

Section 6 – Term and Termination.

This Public License applies for the term of the Copyright and Similar Rights licensed here. However, if You fail to comply with this Public License, then Your rights under this Public License terminate automatically.
Where Your right to use the Licensed Material has terminated under Section 6(a), it reinstates: automatically as of the date the violation is cured, provided it is cured within 30 days of Your discovery of the violation; or upon express reinstatement by the Licensor. For the avoidance of doubt, this Section 6(b) does not affect any right the Licensor may have to seek remedies for Your violations of this Public License. For the avoidance of doubt, the Licensor may also offer the Licensed Material under separate terms or conditions or stop distributing the Licensed Material at any time; however, doing so will not terminate this Public License. Sections 1, 5, 6, 7, and 8 survive termination of this Public License.

Section 7 – Other Terms and Conditions.

The Licensor shall not be bound by any additional or different terms or conditions communicated by You unless expressly agreed. Any arrangements, understandings, or agreements regarding the Licensed Material not stated herein are separate from and independent of the terms and conditions of this Public License.

Section 8 – Interpretation.

For the avoidance of doubt, this Public License does not, and shall not be interpreted to, reduce, limit, restrict, or impose conditions on any use of the Licensed Material that could lawfully be made without permission under this Public License. To the extent possible, if any provision of this Public License is deemed unenforceable, it shall be automatically reformed to the minimum extent necessary to make it enforceable. If the provision cannot be reformed, it shall be severed from this Public License without affecting the enforceability of the remaining terms and conditions. No term or condition of this Public License will be waived and no failure to comply consented to unless expressly agreed to by the Licensor. Nothing in this Public License constitutes or may be interpreted as a limitation upon, or waiver of, any privileges and immunities that apply to the Licensor or You, including from the legal processes of any jurisdiction or authority.

Acknowledgements

First and foremost, this work is dedicated to the memory of Brian Graves Barrett. Who always believed I was capable of more. Who convinced me to make the best decision of my life and go back into education. Who was so very proud when I called to tell you I had been accepted to a PhD program. I am, and remain eternally sorry that I could not finish quickly enough. Requiescat in pace, you earned your peace, grandad.

Secondly, to my darling fiancée, Georgina Peace, thank you, so very much. I love you more than I can put to words. In the times where this work nearly broke me, you were always there to pick me up and keep me steady.

Thank you, Professor Sven L.M. Schroeder, for being so patient, so encouraging, and so willing to let me travel whatever path my mind took me. Thank you for never spoon feeding, and for forcing us to figure things out for ourselves.

Thank you to Beth Willneff for your patience and guidance. Thank you for teaching me pretty much everything I know about XPS spectroscopy. Thank you for your good humour, and thank you for giving me a much greater appreciation for paint!

I would dearly like to thank all those who helped to make various beam times successful. To Hadeel Hussain, Sin-Yuen Chang, and Marc Tesch for being so welcoming and for teaching me how not to destroy UHV set-ups, and for giving of your knowledge and experience so freely.

To my colleagues, Abdul, Arturs, Bethan, Thoko, and Laila, thank you for your patience and the many interesting discussions. To the members of the CDT in Complex Particulate Products, Olivier, David, Tim, Andy, and Frans, thank you for a year of interesting study.

To my good friends Jonathon Carr, Daniel Thomas, Alex Moldovan, Jakub Janowiak, Tom Hardcastle, Allegra Hartley, and Ella Blanquet thank you. I owe you all more than I can ever hope to repay. Your friendship has been a constant source of joy and has kept me grounded and sane.

Finally, to Martin Callaghan, Mark Dixon, and Joanna Leng. Thank you, you inspired me more than I ever thought I could be. I learned a whole new discipline from you, and it turned into a career.

Benjamin Thomas Tayler-Barrett acknowledges a studentship funded through the EPSRC CDT in Complex Particulate Products and Processes (CP3-CDT) Grant number EP/L015285/1.

Special thanks also to Dr. John Hone, and Syngenta Ltd. for their kind sponsorship of this work.

Abstract

Much work has been done in the mechanisms of surfactant adsorption to inorganic compounds. Very little work has been on the molecular basis of these interactions, and almost no work has been on the molecular basis of surfactant adsorption to organic molecular crystals. A major reason for this, is that non-destructive techniques with sufficient surface sensitivity, on the order of $\leq$ 5nm, have not yet been made available to researchers. Until recently, the techniques that give information on this level require either destructive techniques, for example secondary ion mass spectrometry (SIMS), or conductive samples such as X-ray photoelectron spectroscopy (XPS), or are limited in the nature of atomic scale information that can be obtained, such as atomic force microscopy (AFM). Recent advances in the use of XPS equipment, such as near-ambient pressure XPS (NAP-XPS), have opened up this technique to researchers interested in the study of insulating organic compounds.

In terms of complex formulated products (CFPs), the tailoring of formulations by design would benefit from a detailed fundamental understanding of the relationship between molecular level properties and the performance of API physical forms, including inter-facial interactions with excipients. In this work the form I paracetamol single crystal and Tergitol NP-9 nonyl phenyl ethoxylate surfactant were used as model compounds. This model was then used to determine whether adsorbed Tergitol NP-9 could be detected and quantified at the paracetamol surface by NAP-XPS.

Tergitol NP-9 quantification was indeed found to be possible, in terms of relative contribution to XPS signal and it was possible to calculate layer thicknesses. This was initially made possible by supporting density functional theory calculations and XPS analysis of ultra pure samples, which was followed by the determination of a practical method for the removal of additional carbonaceous contamination from the paracetamol surface. Finally, outputs were used to calculated not only the layer thickness and relative contributions from Tergitol molecules, but it was also possible to determine the orientation and configuration of adsorbed Tergitol NP-9.

Contents

List of Tables

List of Figures

Chapter 1

Introduction

1.1 Motivation for Research

1.1.1 Complex Formulated Products

Complex formulated products (CFPs) form one of the cornerstones of modern society, from the coatings on walls and vehicles, to the feed stocks and protective compounds that supply the global demand for food, up to the food we eat and our methods of maintaining personal hygiene. They also form the bedrock of modern medicine and the foundations upon which our life expectancy depends, both through the security of food supply, and through the development and manufacture of modern pharmaceuticals. Though these brief descriptions are by no means exhaustive. CFPs can be defined as multi-component mixtures in which the physical properties of the mixture are as important as the desired function [1]. Examples of CFPs include, but are by no means limited to, pharmaceutical drug products, agrochemicals, paints & coatings, personal care products, fuel additives, and confectionary [2]. As a brief example, the principal ingredient in many antiperspirants is aluminium chlorohydrate (ACH) [3]. The application of pure ACH powder is a method that is known to produce irritation [4] and is best avoided. Consumers have the choice between multiple application methods, ranging from roll-on emulsions, aerosol suspensions, and wax based suspension sticks, to name but a few of the many that are manufactured. While there are some differences in the efficacy of these different applicator methods [5], the principal reason for the variation is consumer perception. This shifts the "value" of the manufactured product from the cost of materials to the end user. The value is instead placed in the perceived effect of the product, as opposed to the cost of its constituent ingredients. CFPs contributed large sums to the global economy. Table 1.1 shows a small selection of organisations involved in the sale and production of CFPs which together, contribute $289.8 billion to the global economy in 2015. As is evident from this selection of organisations, the importance of CFPs to the global economy cannot be exaggerated. To take a less economical viewpoint, the purpose of these products is to improve the consumer's quality of life. Therefore, as the science underlying them is better understood, the resultant improvements to the consumer's quality of life can likewise, not be exaggerated.

Table 1.1: CFP producing organisations and sales for 2015

Organisation	**Industry**	**Sales in 2015 ($Billion)**
Proctor & Gamble	Home & Personal Care	65.3 [6]
Pfizer	Pharmaceuticals	48.9 [7]
PPG* Industries	Paint & Coatings	15.3 [8]
Syngenta	Agrochemicals	13.4 [9]
Unilever	Home & Personal Care / Food	58.1 [10]
Nestlé	Foods	88.8 [11]

* PPG - Pittsburgh Paint & Glass

1.1.2 Active Compounds & Excipients

CFPs are often comprised of more than a single ingredient. For example, in the UK the non-steroidal anti-inflammatory ibuprofen is often taken by the general public as an analgesic for mild to moderate pain. Ibuprofen can be purchased over the counter (that is, in the absence of a prescription from a medical professional) and is inexpensive in the UK to do so. Very broadly, a CFP is made up of two categories of ingredient. They typically contain an active ingredient and one or more excipients. With the active compound being that which gives rise to the principal effect of the product. For example, the aforementioned ACH that prevents visible sweating [3], or the drugs paracetamol and ibuprofen which are common analgesics [12, 13]. In these examples, the molecules interact with either enzymes *in vivo* [12, 13], or with molecular components of sweat [5]. Figure 1.1 shows a representative example using the pharmaceutical active acyclovir, an active compound in a drug formulation, bound to the α-chain of the Herpes Simplex protein, Thymidine Kinase. The chain backbone is shown in red with the binding site amino acid side chains shown as sticks (PDB: 2KI5). Excipients are a vast array of compounds that are defined as having no pharmacological effect [14]. They are included in a formulation either to alter consumer perception, to aid in the manufacture of the CFP, or to alter the physico-chemical properties of the CFP [15]. These could be in the form of bulking agents [16], dispersants [17] or rheology modifiers [18]; though this is by no means an exhaustive list. While ibuprofen is the *active* ingredient there are many forms in which a member of the public can procure it, from liquid filled capsules, to solid tablets, to topical creams and gels. Each of these forms contains a number of *excipients*, that is additional ingredients to aid in either the manufacture of the particular form available, to aid in the dissolution of the active ingredient *in vivo*, or to prevent unwanted effects over the shelf life of the product (e.g. aggregation of the solid components of a dispersed product such as a topical cream). Both active ingredients and excipients can be either inorganic or organic compounds. For example, inorganics such as titanium dioxide or zinc oxide, are found in sun protection products [19, 20]. Organic compounds make up the clear majority of drug and agrochemical actives. While much work has been done to further an understanding of surfactant adsorption at the solid/liquid interface of inorganic compounds [21]; relatively little has been done with respect to organic compounds. Therefore, the focus of the rest of this text will be on surface/surfactant interactions at the organic crystal surface.

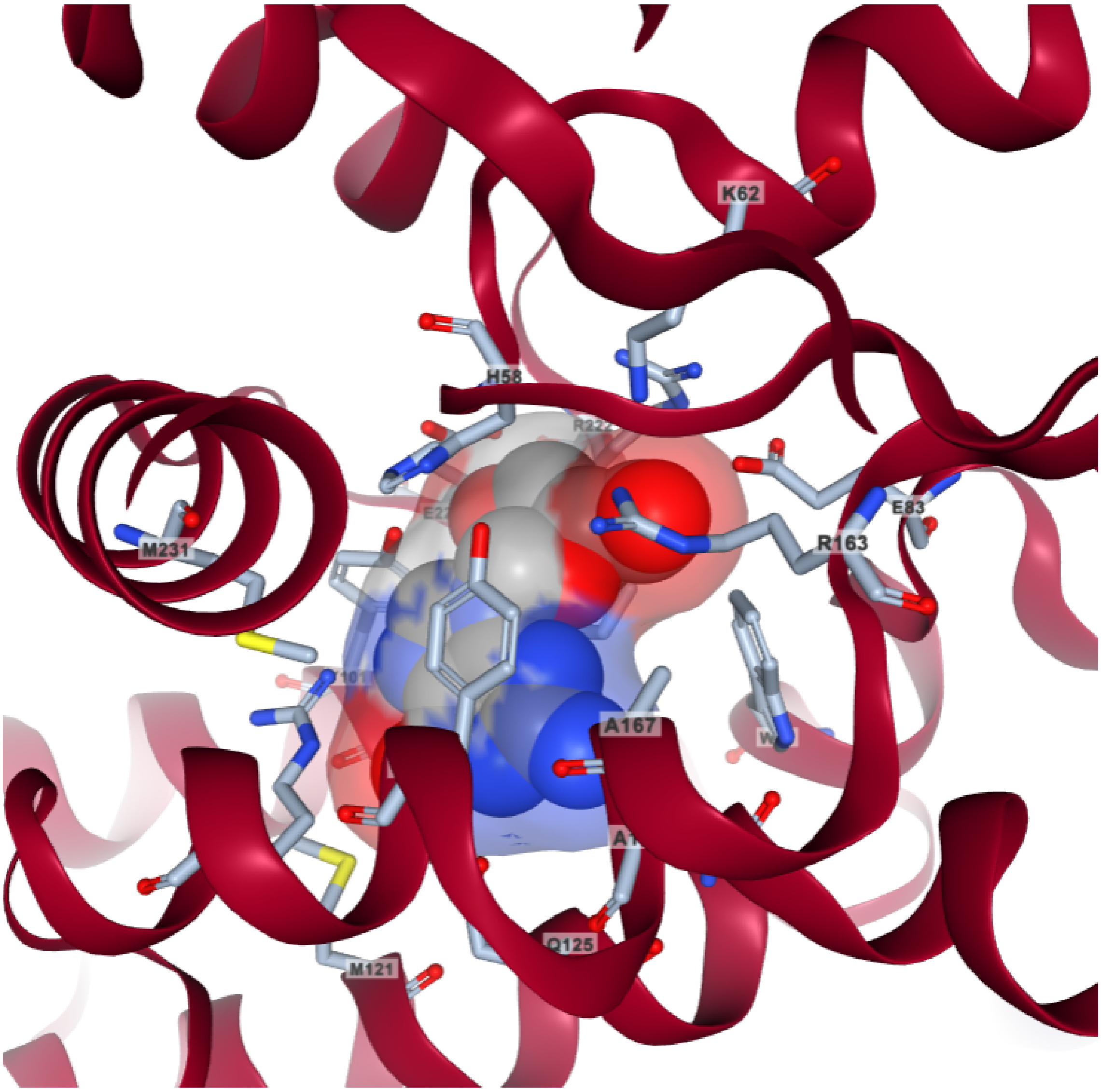

Figure 1.1: The drug active acyclovir in complex with Herpes Simplex Type-1 Thymidine Kinase

1.1.3 Suspensions and Suspension Stability

In order to produce viable CFPs from sparingly soluble organic crystalline actives, in products which are both safe and efficacious, the delivery method for the active component must be carefully considered. While many pharmaceuticals are delivered in the solid form, via tablets or capsules, some along with many agrochemical and cosmetic products are delivered in a fluid form. This may be as a phase separated emulsion or as a suspension. The focus of the rest of this work will be on the latter, and given the incompatibility of most organic solvents with living systems, it will specifically focus on aqueous suspensions.

1.1.4 Wetting

In order to ensure sparingly soluble organic crystals are stable in a solution a number of factors must be considered. Of major importance is the wetting of the crystal surfaces by the continuous phase. Van der Waals London-dispersion forces between hydrophobic surfaces will dominate over water adsorption and cause the suspended crystals to agglomerate [22]. The surface energetics of solid/liquid interfaces was first described in the early 1800s by Young, who determined that the relationship between contact angle (Θ_γ), solid surface energy (γ_{SV}), liquid/solid surface energy (γ_{SL}) and liquid/vapour (γ_{LV}) by [23, 24];

$$\gamma_{SV} - \gamma_{SL} = \gamma_{LV} \cos \Theta_\gamma \tag{1.1}$$

Of these, however, only the γ_{LV} and Θ_γ components can be measured. In the 1960s it was determined that by plotting $\cos \Theta$ vs γ_{LV} for a series of homologous fluids on a solid surface, produces rectilinear bands; With the intercept of the lower band at $\cos \Theta = 1$ being a critical surface tension of the solid (γ_C) [24]. This can then be incorporated into the equation 1.1 as;

$$\gamma_{SV} - \gamma_{SL} = \gamma_{LV} \cos \Theta_\gamma = (1)\, \gamma_C \tag{1.2}$$

Also in the 1960s, work was done to determine the remaining parameters, taking into account the contributions of both dispersion forces $\left(\gamma_L^d\right)$ and hydrogen bonding $\left(\gamma_L^h\right)$ to γ_{LV} and expressed mathematically as [25];

$$\gamma_{LV} = \gamma_L^d + \gamma_L^h \tag{1.3}$$

A further discussion of this was presented by Owens & Wendt, who described a system where both forces operate and expressed as [26];

$$\gamma_{SL} = \gamma_{SV} + \gamma_{LV} - 2\sqrt{\gamma_S^d \gamma_L^d} - 2\sqrt{\gamma_S^h \gamma_L^h} \tag{1.4}$$

where γ_S^d represents the contribution of dispersion forces from the solid and γ_S^h represents the contribution of hydrogen bonding from the solid. Which can be alternatively expressed as [26];

$$\gamma_{SL} = \left(\sqrt{\gamma_S^d} - \sqrt{\gamma_L^d}\right)^2 + \left(\sqrt{\gamma_S^h} - \sqrt{\gamma_L^h}\right)^2 \tag{1.5}$$

Heng and Williams used such a method to show the facet-specific wetting behaviour of water on monoclinic (form I) paracetamol crystals. Their data showed that of six facets, the surface tension ranged from 52.1 mJ/m^2 at the (010) surface, to 72.4 mJ/m^2 at the (001) surface with the surface tension at all six facets being [27, 28];

$$(001) > (011) > (201) > (110) > (010)$$

Thereby showing that the first barrier to the formulation of a stable organic crystal suspension, that is the wetting of the individual surfaces, can only be exquisitely controlled through the understanding of the facet-specific surface chemistry.

1.1.5 Particle Size and Shape

Typically, in the context of CFPs, the acceptable size of the active solids is related in some way to the function (or indeed the *perceived* function) of the product. The particle size distribution (PSD) in a suspension is largely dictated by the desired effect of the formulation. For example, if a pharmaceutical product is delivered as a suspension via the gastrointestinal tract, the suspended particles must fully dissolve for the molecules to be absorbed. Any that do not dissolve will not become bioavailable and will pass through the patient without being of any clinical value. Therefore, the maximum size of the particles must allow for complete dissolution. Alternatively, those used as inspiration drugs (inhaled) must be available for deposition within the alveoli in the lungs. These crystals must be no larger than 5 microns. This is by no means an exhaustive list, but simply highlights that the particulates must be designed in such a way as to optimise their end use; the suspension must be formulated to accommodate this.

To maintain a stable PSD in a suspension one must consider two preventative measures, one of which is inhibiting the particles from growing, the other is inhibiting particle dissolution. The primary method by which particles grow when in suspension is through the process of Ostwald ripening [22]. During this process, the particles with higher solubility dissolve and the material are deposited onto the less soluble particles [22]. The Ostwald-Freundlich equation [29, 30] shows that the smaller the particles, the more soluble they are. For two spherical particles of radii $r_1 > r_2$, the exponent of the Ostwald-Freundlich equation can be used to determine the rate of Ostwald ripening as a function of the difference in radius between the particles by [22];

$$\frac{RT}{V_c} \ln\left[\frac{X_{eq}(r_1)}{X_{eq}(r_2)}\right] = 2\gamma\left[\frac{1}{r_1} - \frac{1}{r_2}\right] \tag{1.6}$$

where R is the ideal gas constant, T is the absolute temperature, V_c is the volume of the dispersed crystals, X_{eq} is the solubility of surrounding a particle of radius r, and γ is the interfacial tension at the solid/liquid interface.

1.1.6 Sedimentation

Sedimentation is a result of the dispersed solid phase not remaining uniformly distributed throughout the liquid carrier phase. This occurs when the density of particulates in suspension is higher than that of the carrier fluid. Particle sedimentation in suspensions should also be considered, as it is generally undesirable to produce suspensions in which the dispersed phase does not remain uniformly dispersed throughout the formulation. Sedimentation is an effect produced by gravity, whereby the particles sink to the bottom of their container and become difficult to re-disperse. Particles small enough to have their dispersion governed by Brownian motion are less of a concern, but as seen in the above sections, this has repercussions on the rate of Ostwald ripening and the surface energy of the particles. When one compares the Brownian motion of the particles (kT, where k is Boltzmann constant and T is the temperature), to the effect of gravity on the particles, by Eqs. 1.7 (gravity force) & 1.8 [22];

$$\tfrac{4}{3}\pi r^3 \Delta\rho g L \tag{1.7}$$

where $\Delta\rho$ is the buoyancy of particle in the liquid medium, g is acceleration due to gravity, and L is height of the container.

$$\tfrac{4}{3}\pi r^3 \Delta\rho g L > kT \tag{1.8}$$

One can see that where Eq. 1.8 is true, sedimentation of the particles will occur [22].

1.1.7 Prevention of Particle Growth and Sedimentation

As can be seen from the above two subsections, the management of these factors in a CFP must be carefully considered. If for example, a particular PSD is required, and the PSD will result in sedimentation of the particulates, and the product must be delivered in suspension form, clearly this will start to cause problems. One of the simplest properties that can be altered is the inter-facial tension between the solid particulate surfaces and the liquid carrier. While one can optimise a process by which solid particulates are produced with a narrow PSD, this may not be enough to maintain the stability of the formulation for the entire duration of the product life cycle. Similarly, one may be lucky enough to be able to produce a formulation in which the solid particulates are of a PSD that keeps their motion governed by Brownian motion. For a multitude of reasons, this is not always the case. In fact, it may be the case that the system desired has a long, useful product life cycle, but the particulates must be of sufficient size to have their motion governed by the effect of gravity. Methods of dealing with the challenges must be focused on the properties that can be altered. In the case of preventing particle growth the simplest term that can be altered by formulation is the γ term. For clarity, this being the interfacial tension between the continuous phase and the solid particulates. Given that this is an intrinsic property of the system, some excipient must be added to the formulation to facilitate a change in γ. To achieve a change in γ, surface active agents (surfactants) can be added to the formulation. Surfactants are amphipathic molecules that contain a hydrophobic portion, usually some form of hydrocarbon, commonly referred to as the "tail" [31]. They also contain a hydrophilic group, either a polar or ionic species, commonly referred to as the "head" [31]. Figure 1.2 shows a representation of three surfactant molecules, stearic acid (left), benzalkonium chloride (middle, chloride ion not shown), and an ethoxylate surfactant (right).

For the purposes of this review, the following surface/surfactant interactions that are of interest are the adsorption of non-ionic surfactants to either polar or non-polar surfaces. Organic crystals often have surfaces with varying chemical compositions. For example, some surfaces may be hydrophilic in nature, and others hydrophobic. When considering surface/surfactant interactions particularly regarding a suspension formulation, the starting point should be to understand the adsorption isotherm. This can be calculated from equation 1.9 [31];

$$\Gamma_{tot} = \frac{\Delta C_s V}{mA} \tag{1.9}$$

where Γ_{tot} is the total surface concentration of adsorbed surfactant in mol/m^2, m is the mass in grams of adsorbent, V is the volume of the liquid phase, A is the surface area of the adsorbate in m^2/g, and ΔC_s is the difference in concentration of surfactant at zero adsorption to some concentration of adsorbed surfactant in the liquid phase [31]. The plot of Γ_{tot} as a function of C_s shows the adsorption isotherm. At Γ_{tot}^{∞} where a full monolayer has adsorbed to all available surfaces the area covered by a single surfactant

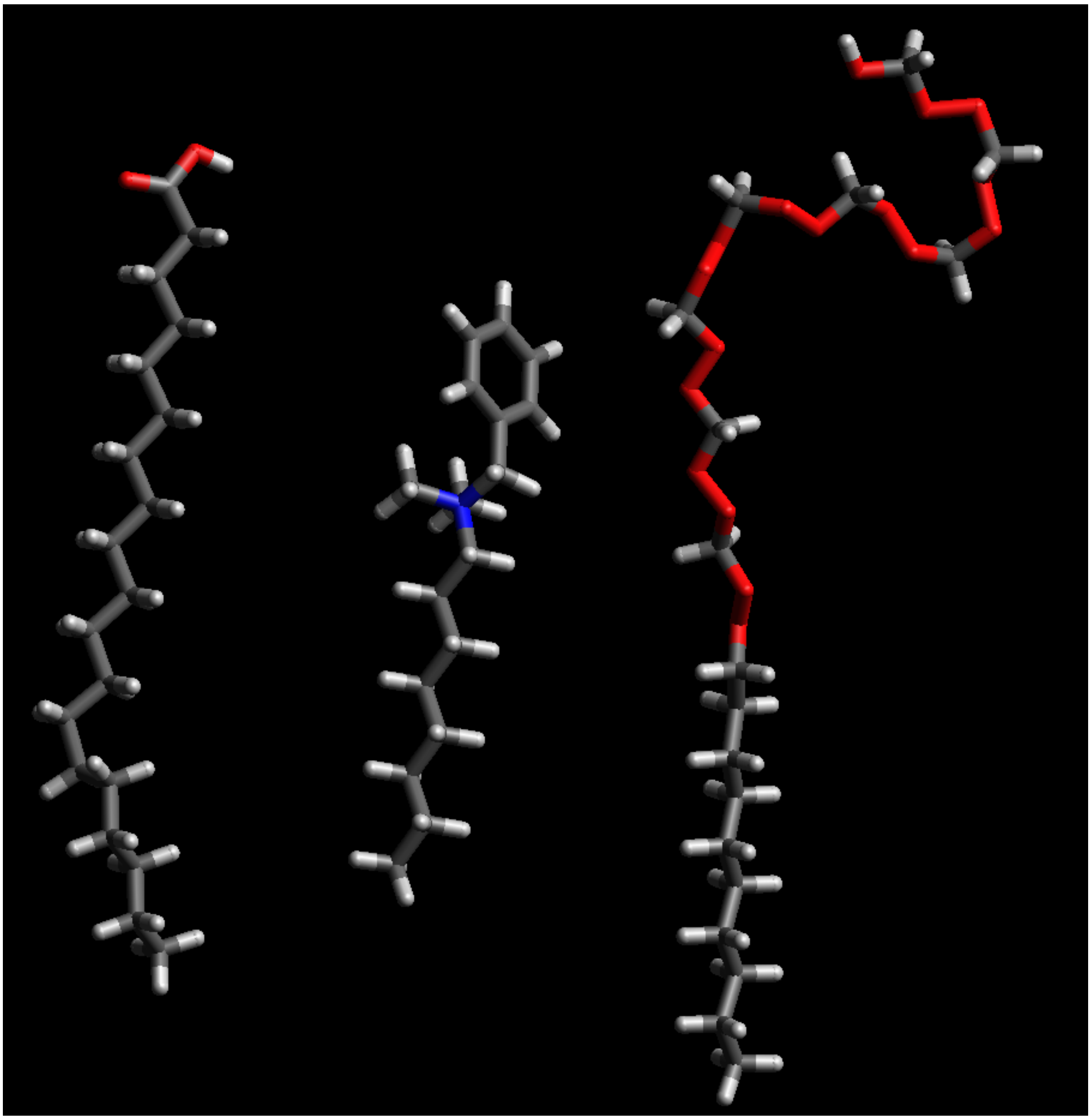

Figure 1.2: Stick representation of three surfactant molecules
Steric acid, benzalkonium chloride (chloride not shown), and an ethoxylate surfactant.

molecule can be calculated by [31];

$$A^{s} = \frac{10^{18}}{\Gamma^{\infty}_{tot}} n_{av} \tag{1.10}$$

where A_s is the area covered per surfactant molecule in nm_2 and n_{av} is Avogadro's constant [31].

While this is useful information, it cannot currently be analytically determined in a facet-specific manner. Nor can any information be obtained without recourse to experiment. When one considers that some high-value compounds, such as novel APIs, can run to very high production costs for relatively small amounts. It becomes increasingly necessary to have some means of calculating these isotherms if only to give an indication to experimentalists as to where their experiments should begin. Given that a great many organic crystalline systems are also surface heterogeneous, that is, for any given single crystal, the surfaces differ with respect to each other in terms of chemical composition. To the extent that some surfaces may be hydrophobic and others hydrophilic. If finesse is to be achieved in the formulation, one must have a measure of how these systems behave with respect to each available facet of the API. To calculate the theoretical facet-specific adsorption one must first have an expression that relates the surface specific concentration of surfactant to the thermodynamics of adsorption. The following equations allow one to determine this by theory.

The surface specific concentration of surfactant Γ_δ adsorbed can be written as [32];

$$\Gamma_\delta = IC^{\left(\frac{-\Delta G^o_{ads}}{RT}\right)} \tag{1.11}$$

where I is the chain length, C is bulk concentration, R is the ideal gas constant and T is the absolute temperature. ΔG^o_{ads} is the sum of the ΔG^o of all energetic contributions to adsorption [32]. To calculate ΔG^o_{ads} one is required to understand which forces have an impact on adsorption. Very generally, these can comprise, Van der Waals interactions with both the adsorbent surface, and with other surfactant molecules, hydrogen bonding, and Coulombic interactions [32]. Though there is also desolvation of the surfactant head group that must be overcome, and chemisorption that may need to be considered [32].

1.2 X-ray Spectroscopic Techniques for Surface Analysis

What is lacking in the aforementioned techniques, is made up for with a family of methods that fall under the umbrella of soft X-ray spectroscopy. So-called soft X-rays are comprised of electromagnetic radiation that fall within the energy range from about $\sim$100 eV to $\sim$2000 eV. The reason for their usefulness in the analysis of surfaces, is that these low energy X-rays are rapidly attenuated by interaction with matter. This rapid attenuation results in sample analysis depths on the order of single to double digit nanometre scales. It is for this reason they were identified as being ideal for studying surface adsorption. Two techniques, X-ray absorption spectroscopy (XAS) and X-ray photoelectron spectroscopy (XPS) are examples of soft X-ray spectroscopy. They both take advantage of the photoelectric effect, though in different ways.

1.2.1 X-ray Sources

Both the radiative and non-radiative processes can be taken advantage of in XAS techniques, indeed radiative energy loss can be taken advantage of in the generation of the X-rays that one uses to undertake the experimental work. There are currently known, two methods of generating X-rays suitable for use in techniques such as XAS and XPS, as well as other X-ray analytical methods. One is to generate them using laboratory sources. These utilise the previously mentioned radiative energy loss, by exciting a metal plate with a stream of electrons. The advantage of this method is that it is relatively inexpensive compared to the other method, and it is far more portable. That is, the X-ray source can be moved from laboratory to laboratory, or sold after some useful lifetime to offset the purchase cost. The disadvantages are firstly, that the intensity of the X-ray produced is orders of magnitude lower than that of the alternative method. Secondly, that the wavelength of the X-rays produced is characteristic of the metal used to produce them. That is, it is fixed. The alternative method alluded to is the use of synchrotron radiation to generate X-rays. Synchrotrons use a combination of linear accelerators, undulators, and bending magnets to keep electrons moving at near relativistic speeds, which causes them to continually emit energy in the form of electromagnetic waves. The advantages of X-rays produced by these systems are that they are orders of magnitude more brilliant than those produced by laboratory sources. The X-rays can also be fine tuned in terms of the wavelength.

A laboratory X-ray source typically comprises a metal anode and an electron source, in which the incoming energy hv is provided by electrons, which interact with the metal and the characteristic X-rays are produced as a result of the aforementioned radiative energy loss process. The exact metal used in the anode is determined by the energy requirements of that analysis being performed. Table 1.2.1 shows some commonly used elements and their characteristic Kα emitted X-ray energies [33]. The positive aspects of generating X-rays using a laboratory source are that obviously, they can be used in a standard laboratory. Relatively speaking they are a cheaper and more portable alternative to the use of a particle accelerator source. The negative aspect of these sources is that they produce X-rays of only a single photon energy. The most commonly used particle accelerator sources for XAS are synchrotron radiation sources, such as; the Diamond Light Source, UK; Alba, Catalonia; and the National Synchrotron Light Source II (NSLS-II), USA. Though they are by no means the only such facilities available for XAS studies. A synchrotron works by accelerating electrons to near the speed of light by application of a magnetic field. Electrons being matter, cannot reach the speed of light due to relativity and so upon a positive change in velocity instead lose energy by emission of X-ray photons. Though that is but a simple explanation of a rather more complex process. The velocity change is, very broadly, brought about as a function of two factors, one is the geometry of the system in which the electrons travel and the way in which they travel [34, 35, 36]. With respect to the geometry, there are two methods by which an electron can be accelerated, linearly or circularly [35]. When linearly accelerated, the speed and hence the energy of the electrons increases but the radiation generated does not increase in any appreciable way [35]. This can be made use of by bringing the electrons up to near relativistic speeds. With circularly accelerating electrons, however, the speed, and hence energy of the electrons is kept constant, but the velocity is constantly increasing. Under these conditions, the emitted radiation is considerably greater [35]. Modern synchrotron facilities make use of both acceleration methods. Typically, a high-voltage electron source is employed to introduce the electrons into a LINear ACcelerator (LINAC), that carries the electrons into a booster ring. This booster ring is a synchrotron itself, but is employed to bring the electrons up to the required speed. The electrons are then carried by a second LINAC to a second stage synchrotron known as a storage ring. It is from the storage ring that so-called beamlines, built to intersect tangentially to the storage ring, can syphon off the X-ray radiation for use at an experimental end-station. Figure 1.3 shows a cartoon diagram of the National synchrotron light source (NSLS-II) representative of a "generic" synchrotron facility. Where a high-voltage electron source (purple), introduces electrons to a LINAC (blue), these are accelerated into a booster ring comprising linear sections and circular sections. This both begins the process of generating X-ray radiation and

Table 1.2: Characteristic X-ray energies of commonly used elements

Element	**Kα-emission energy (eV)**
Mg	1253.6
Al	1486.6
Ti	4510.9
Cu	8047.8
Cr	5417.0

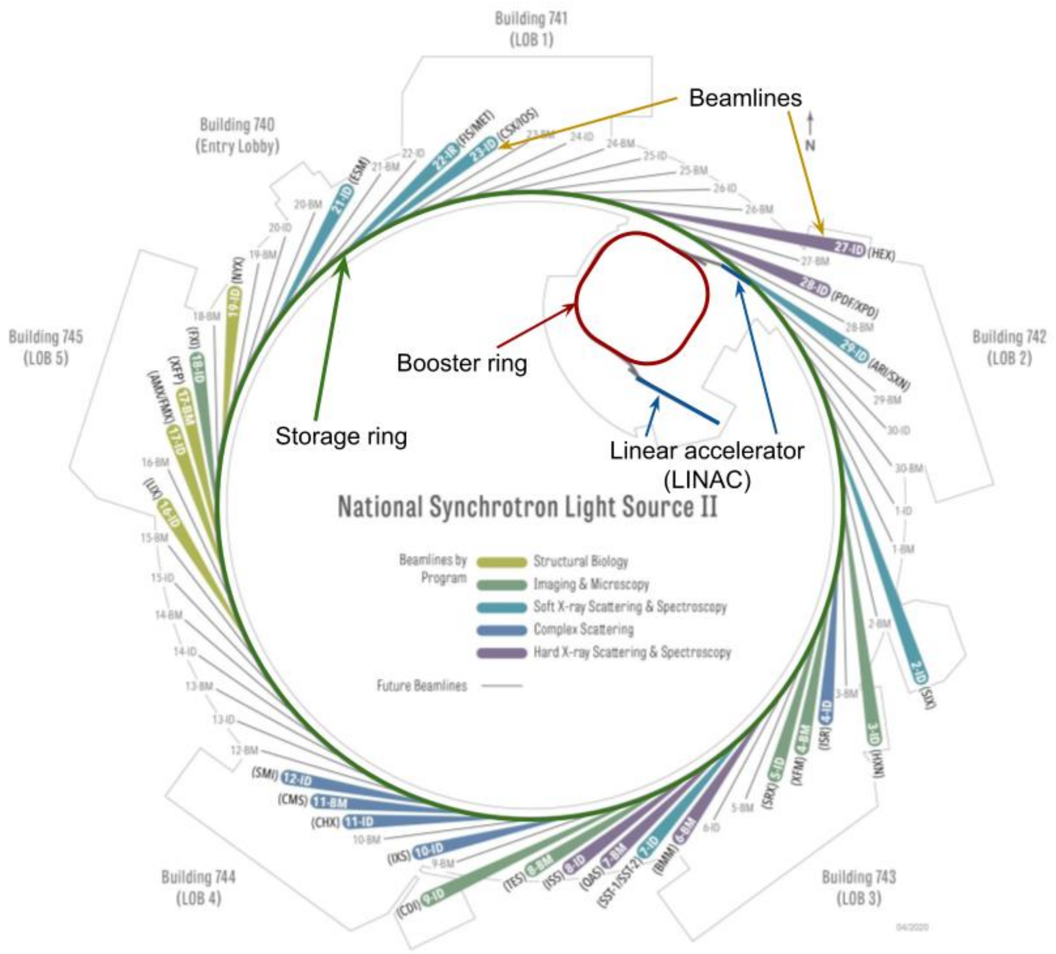

Figure 1.3: National Synchrotron Light Source II (USA) synchrotron radiation user facility [37]

brings the electrons up to speed, before being drawn into a second LINAC section to be introduced to the storage ring (green). From here, the X-ray radiation produced can be syphoned off by the beamlines (orange). A further development in synchrotron technology is the employment of undulators (or wigglers), undulators can be built into straight sections of any part of the synchrotron, including the application of straight sections in the storage ring [36]. Undulators employ a series of magnets in which the magnetic field alters its direction many times. The effect of this on the electron beam is to alter the trajectory from a linear beam to a sinusoidal beam [34]. The strength of the magnetic field is altered by changing the distance of the magnets from the beam, with the strength of the field being inversely proportional to the distance [34]. This allows a user to fine tune the wavelength of the emitted X-rays. The wavelength of the emitted X-rays being related to the energy by;

$$E = hv = \frac{hc}{\lambda} \tag{1.12}$$

where E is the energy of the X-ray photons, h is Planck's constant, v is the frequency of the X-ray wave, c is the speed of light in a vacuum, and λ is the wavelength.

The positive aspects, therefore, of using synchrotron light sources for experiments are that the energy of the X-rays used can be varied, and the X-rays themselves are orders of magnitude brighter than those produced in laboratory sources. This greatly reduces data acquisition time. The drawbacks are that with much brighter sources, any damage to the sample because of X-ray exposure is greatly amplified. An added drawback is that most synchrotron radiation sources are multi-user facilities that are greatly over-subscribed, meaning careful planning and preliminary work must be done before requesting time. Of course, the generation of X-rays by either method does not produce pure X-rays of a single energy. The metal in a laboratory source can also emit X-rays from other orbital interactions, such as Lα or Mα X-rays and synchrotron sources can also contain many energies in the storage ring. There are also other forms of energy that can be generated, such as breaking radiation from slowing particles so-called *bremsstrahlung*. While these other phenomena are not included within the purview of this work, they must still be accounted for by those doing experimental work involving the use of X-ray radiation. The issues of off wavelength X-rays can be solved by utilisation of a monochromator. Monochromators use an arrangement of mirrors and gratings to focus the X-ray beam and ensure that only X-rays of the desired energy pass through them and to the sample [38, 39, 40]. With XAS the method by which one generates the X-rays is not up for choice. The reason for this is that most of the techniques require the use of variable energy X-ray sources, i.e. synchrotron light. They also require some knowledge of the system being investigated for example X-ray diffraction, nuclear magnetic resonance or neutron scattering data. A typical XAS experiment involves exposing a sample to an X-ray beam and recording either the radiatively emitted X-ray photons produced, or the non-radiatively emitted electrons produced, as a function of increasing X-ray energy [41]. This results in a spectrum of either electron counts or photon counts vs. energy.

1.2.2 X-ray Absorption Spectroscopy

X-ray absorption spectroscopy (XAS) is an extremely powerful family of techniques that can be used to probe the nature of a variety of properties of atomic and molecular systems. The basic principle behind XAS techniques is that a sample is exposed to a source of X-ray photons, it absorbs some of these photons and is excited. In order to return to the ground state, some process results in the emission of either particles or photons [42, 43, 41]. The names of the techniques are derived from either the type of particle or photon emitted or the energy range relative to the atom type being probed.

First of these is the photoelectric effect, which occurs when an electron orbiting an atom is excited by interaction with an electromagnetic wave of energy higher than the binding energy of that electron to the nucleus of the atom in question. First explained by Albert Einstein in 1921 is the process by which a photon (in this case, an X-ray photon), interacts with an electron orbital and transfers its energy to an electron [44]. The electron is excited and if the interacting photon can transfer sufficient energy to it, the electron will leave the atom [44]. Figure 1.4 shows a cartoon representation of the photoelectric effect, where an incoming X-ray of energy hv (red wave) interacts with the 1s shell of an oxygen atom. This energy is transferred to a 1s electron with sufficient energy for the electron to escape the atom (purple arrow). The implication of the photoelectric effect, with respect to a non-valence orbital, is the generation of a "hole" in the orbital where the emitted electron resided. This leaves the atom in a relatively high energy state. To relax back down to a lower energy state, the atom can lose energy radiatively, by an electron from a higher orbital dropping into the hole accompanied by the emission of an X-ray photon [45]. Alternatively, the atom can lose energy non-radiatively by restructuring its electrons. This process was first observed by Pierre Auger in 1925 and is thus named the Auger process after him [46]. The principle behind the Auger process is that as an electron leaves the atom and produces a hole, an electron from the orbital above drops into this hole, while an electron from the shell above loses an electron [44]. For example, if the incident X-ray is of sufficient energy to eject a K-shell electron, an electron from the L_1-shell fills the resultant hole, while an L_2-shell electron is ejected from the atom. The radiative and non-radiative processes are illustrated in Figure 1.5. The image on the left shows the radiative energy loss of an oxygen atom as an incoming X-ray (red wave), excites an electron in the K-shell. An L-shell electron drops to fill the hole (dashed purple), and energy is radiated by the atom in the form of a characteristic X-ray (green wave). The image on the right shows the Auger process, where the relaxation of an L_1-shell electron (dashed purple), is accompanied by energy loss by ejection of an L_2-shell electron (dotted purple).

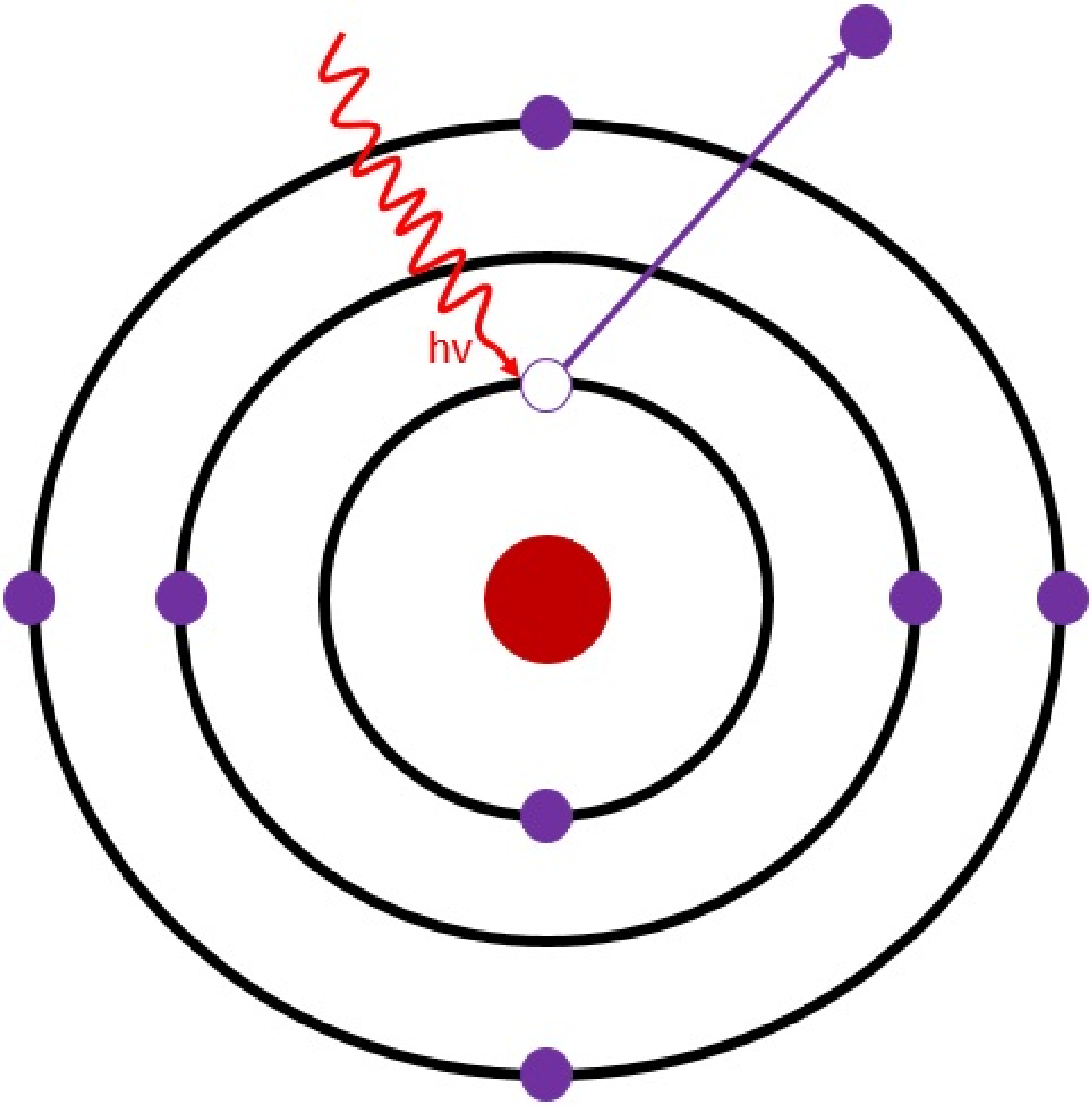

Figure 1.4: The photoelectric effect
In which the red wave represents an incoming photon.

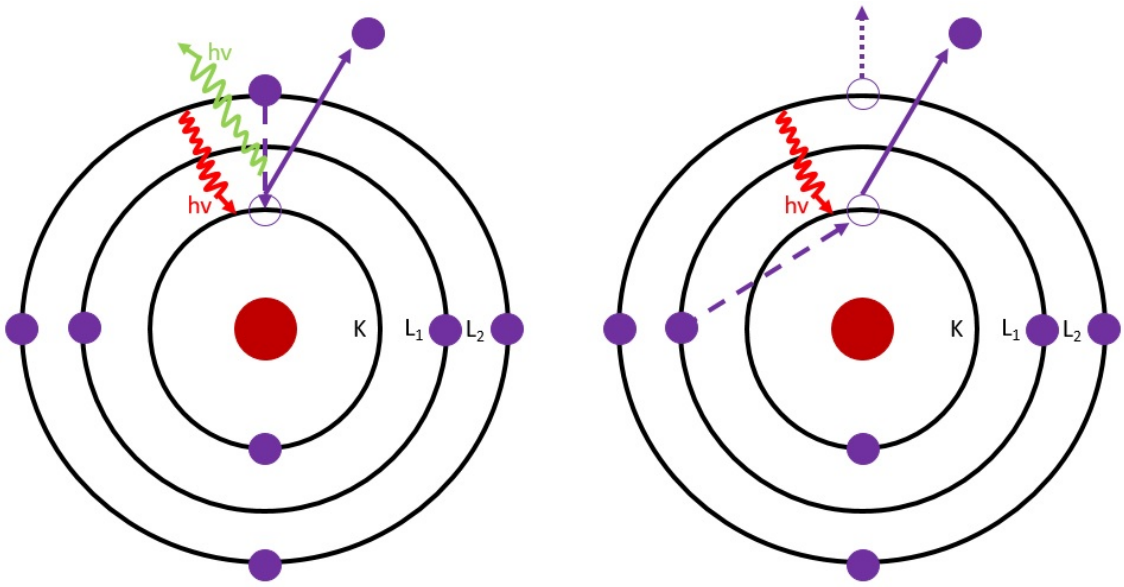

Figure 1.5: Radiative and non-radiative energy loss, respectively
In which the red wave represents an incoming photon and the green wave an emitted photon.

1.2.3 Near-Edge X-ray Absorption Fine Structure

Near-edge X-ray absorption fine structure spectroscopy (NEXAFS) is an X-ray analysis technique whereby the energy of incident X-rays is varied and the number of either electrons or photons emitted by the sample is counted. This could be either the total number of particles, or some partial number of them. These analyses are typically done around some expected ionisation edge for a specific atom class in a given molecule, for example, nitrogen at ∼400 eV. The two modes described are referred to as either fluorescence yield (FY) or electron yield (EY) and can be done as either partial or total (PFY, TFY, PEY, and TEY) [41, 47, 48]. In EY mode, electrons emitted by the excited samples are detected whereas in FY mode, fluorescence photons emitted by the sample are detected. Thereby taking advantage of either non-radiative energy loss or radiative energy loss, respectively. The chemical information obtainable from the NEXAFS technique is the bond structure and lengths, lowest unoccupied molecular orbital (LUMO) energy, as well as the energies of transitions to higher LUMO states. NEXAFS is highly sensitive to any changes in the environment of atoms being probed.

This spectrum can be broadly defined as having three dominant features, the ionisation edge of the atom being probed, the spectrum near (within around 20-50 eV) edge and everything beyond this [42, 41, 49]. The ionisation edge is the energy at which an electron from a stated orbital is imparted with enough energy to break free of the atom, or in plain language, the energy at which the photoelectric effect occurs. The spectrum near the edge is commonly referred to as either the X-ray absorption near edge structure (XANES) or near-edge X-ray absorption fine structure (NEXAFS) [41]. Beyond this region is known as the extended X-ray absorption fine structure (EXAFS)

[49]. While the EXAFS region and interpretation of the data are beyond the scope of this review, it can be described as the scattering of the released electron in the environment surrounding the atom from which it was released [49]. The information in the NEXAFS region of the spectra gives information on the electronic structure of the molecule containing the atom of interest, the ionisation edge, and the bond structure of the molecule around the atom [41]. Figure 1.6 shows a "generic" NEXAFS spectrum and its makeup [48]. The plot in the top right corner shows the spectrum as an output from the experiment. The energy diagram (bottom), shows a two-atom molecule in which the blue atom has been exited by the X-ray beam with enough energy to promote a 1s (K-shell) electron. First into a π^* orbital (orange arrow), then into Rydberg states (black arrow), then beyond the ionisation potential (blue arrow), and into σ^* continuum states. Finally, beyond these continuum states, the electron is excited to vacuum where it can undergo scattering with nearby atoms (EXAFS). The features in the spectrum are related to the electronic structure of the molecule being probed. With the first transitions being to π^* anti-bonding orbitals, though obviously, this only applies to molecules which contain double or triple bonds [41, 48]. This is followed by transitions to the molecule's Rydberg states. After this, the sharp rise in the spectrum is the ionisation potential of the molecule [41, 48]. Beyond this, the σ^* transitions appear in the spectra to the point that the photoelectron is completely free of the molecule. Assignment of these features to transitions within the molecule requires information on the molecular orbital structure of the system being studied. The molecular orbitals can be calculated computationally using quantum mechanics (QM) software [50, 51]. Where the first peak in the spectrum is the transition of the photoelectron to the lowest unoccupied molecular orbital (LUMO) allowed. What this means, is that for an atom x being probed in a molecule containing atoms x, y, and z, there must be some oscillator strength from atom x, to the wave function of the molecular orbital for it to appear in the NEXAFS spectrum. This follows from "Fermi's Golden Rule";

$$\sigma_\chi \propto |\langle \Psi_f | e \cdot p | \Psi_i \rangle|^2 \rho_f(E) \tag{1.13}$$

where σ_χ is the photoionisation cross section, Ψ_i is the wave function of the initial state, Ψ_f is the wave function of the final state, e represents the electric field vector, p is a dipole transition operator and $\rho_f(E)$ is the energy density of the final state [41, 48].

In a NEXAFS experiment, analysis depth is tightly coupled to the escape depth of any photons or electrons from the surface, it is therefore an ideal technique for doing surface analysis. The key drawback to this technique, is that it works well only in combination with additional techniques. For example, with X-ray diffraction, which gives information on which atoms are present in a given system, and their relative positions with respect to each other.

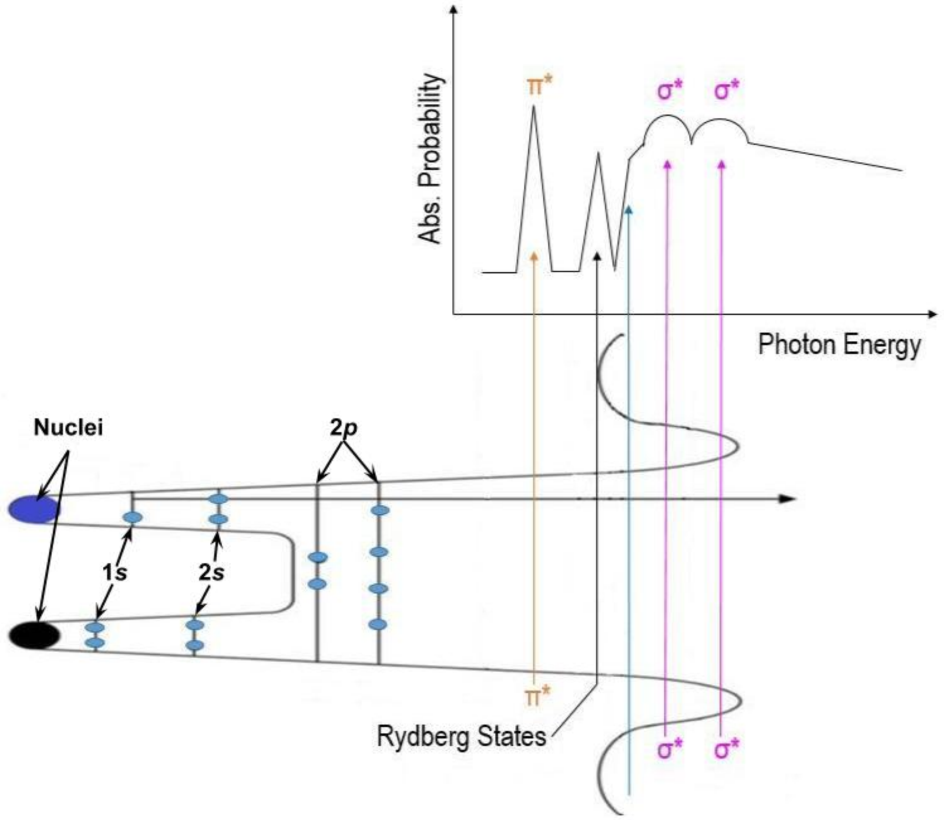

Figure 1.6: Relationships between atomic core level excitations and observed absorption spectrum

1.2.4 X-ray Photoelectron Spectroscopy

X-ray photoelectron spectroscopy (XPS), also referred to in texts as electron spectroscopy for chemical analysis (ESCA) was originally developed in the 1950s by Kai Siegbahn, for which he won the Nobel Prize in 1981 [52]. XPS works on a similar principle to NEXAFS, only in this case the energy of incident X-rays is fixed and the escaping electrons are filtered on kinetic energy. The kinetic energy of these electrons is tied to their binding energies to the atom from which they escaped, and to the energy of the incident X-rays exciting those atoms. The emitted photoelectrons are focused by magnetic collector lenses, and at the same time, their kinetic energy is retarded by the collector lens [44]. The level of retardation allows only electrons with kinetic energy higher than the level of retardation to complete the journey through an electrostatic hemispherical analyser. The analyser sets a potential of ΔV between an inner and outer hemisphere such that the outer is negative and the inner is positive, in relation to the centre line [44]. With the centre line being referred to as the pass energy. If the kinetic energy of the electrons is greater than $\pm 10\%$ of the pass energy after they have been retarded by the lens, the electrons cannot pass through the analyser and collide with one of the hemispheres [44]. At the exit of the analyser is an electron detector, which registers an electron interaction and outputs a count rate for that particular energy [44]. Figure 1.7 shows a

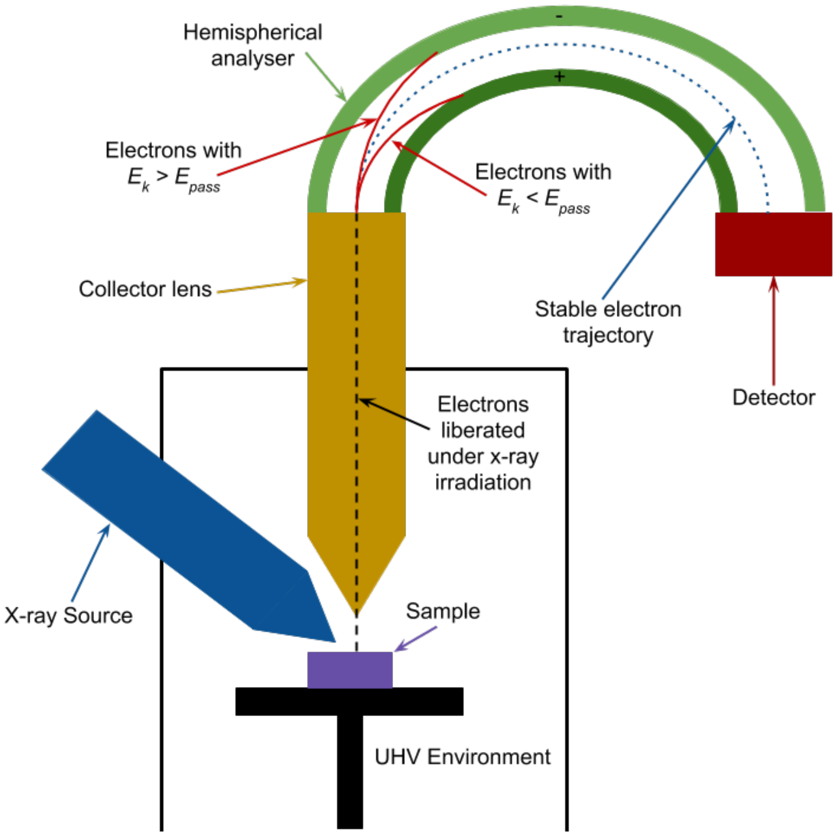

Figure 1.7: Schematic diagram of a typical XPS instrument

cartoon diagram of a typical XPS instrument. Where a sample (purple), is irradiated by an X-ray source (blue). The resultant emitted photoelectrons (dashed lines) are taken in by the collector lens (orange) and their kinetic energy retarded by a defined amount. The photoelectrons are then analysed by the hemispherical analyser (green), where those electrons with kinetic energy $>$ pass energy of the analyser collide with the outer hemisphere (red dashed line). Those with kinetic energy $<$ pass energy collide with the inner hemisphere (green dashed line). Those with kinetic energy $=$ pass energy (blue dashed line), register on the detector (red). Modern instruments may also incorporate monochromators into the X-ray source, and multi-channel detectors that can detect a range of kinetic energies. The kinetic energy of a given photoelectron can be related to the binding energy, or the excitation energy required for the photoelectron to break from its orbital and escape into vacuum. The relationship is simply the difference between the total X-ray energy (λ) and the binding energy (BE), is imparted to the photoelectron as kinetic energy (KE), or;

$$BE = \lambda - KE \tag{1.14}$$

There is another factor that must be considered when evaluating the output from an XPS experiment. Where electrons are leaving the sample, particularly with regard to organic materials, remaining electrons bind more strongly in the sample, this reduces the kinetic energy of the escaping electrons. This effect is referred to as the work function

(ϕ) and is incorporated into Eq 1.14 as [44];

$$BE = \lambda - KE - \phi \tag{1.15}$$

The key benefit of XPS is in the analysis of chemical information at the surface of a material. This is a result of the inelastic scattering of photoelectrons within the sample bulk preventing them from escaping to the collection lens [53]. The depth at which 95% of the electrons emitted can reach the analyser without interacting with another molecule is known as the inelastic mean free path (IMFP) [53]. A consequence of this is that on average, the data acquired by the XPS instrument is on the order of 3-5 nm. The first step in the quantitative analysis of XPS spectra is the subtraction of the inelastically scattered electrons (ISEs), throughout the sample that is detected by the instrument. These ISEs make up the background of the spectra, which must be subtracted from the photoelectron peaks [54]. The most common method of background subtraction is the application of a Shirley background [54]. Once all peaks have had their background subtracted, one must then consider the photoionisation cross-section of the atoms for which peaks have been identified [55]. These photoionisation cross-sections have been extensively studied and are reported in the literature [56]. Many advances have been made in recent years to the application of XPS in systems under near ambient pressure conditions. Though almost all of these studies focus on inorganic systems, particularly in the fields of catalysis and corrosion [57, 58, 59, 60]. Those that have been done with a focus on organic compounds, have been done so on small surface concentrations of organics, polymers, and a limited number of studies on organic crystal powders [61, 62, 63]. Should these techniques be shown to be applicable to insulating organic crystal surfaces, many avenues will be opened in the analysis of these surfaces. A schematic diagram of a NAP-XPS instrument can be seen in figure 1.8

XPS analysis can be performed as a *survey* scan, that is, scanning all kinetic energies possible given the energy of incident X-rays, but with reasonably large steps between kinetic energy increments. These measurements are generally fairly rapid, on the order of minutes. Or as *detailed* scans in which the step increments in kinetic energy are typically very small, but the range over which one measures is also very small on the order of tens of eV. Survey scans give rapid information on the atomic constituents of the sample under analysis, both the nature of the atoms, and the relative levels of them in the sample. Detailed scans give information on the environment of a given atom type. In plain language, survey scans tell the researcher that carbon and oxygen, for example, are present in a sample, and how much of each with respect to the other is present. Detailed scans allow the researcher to determine the relative levels of different carbon environments, for example double bonded carbon to oxygen, from aromatic carbon, for example.

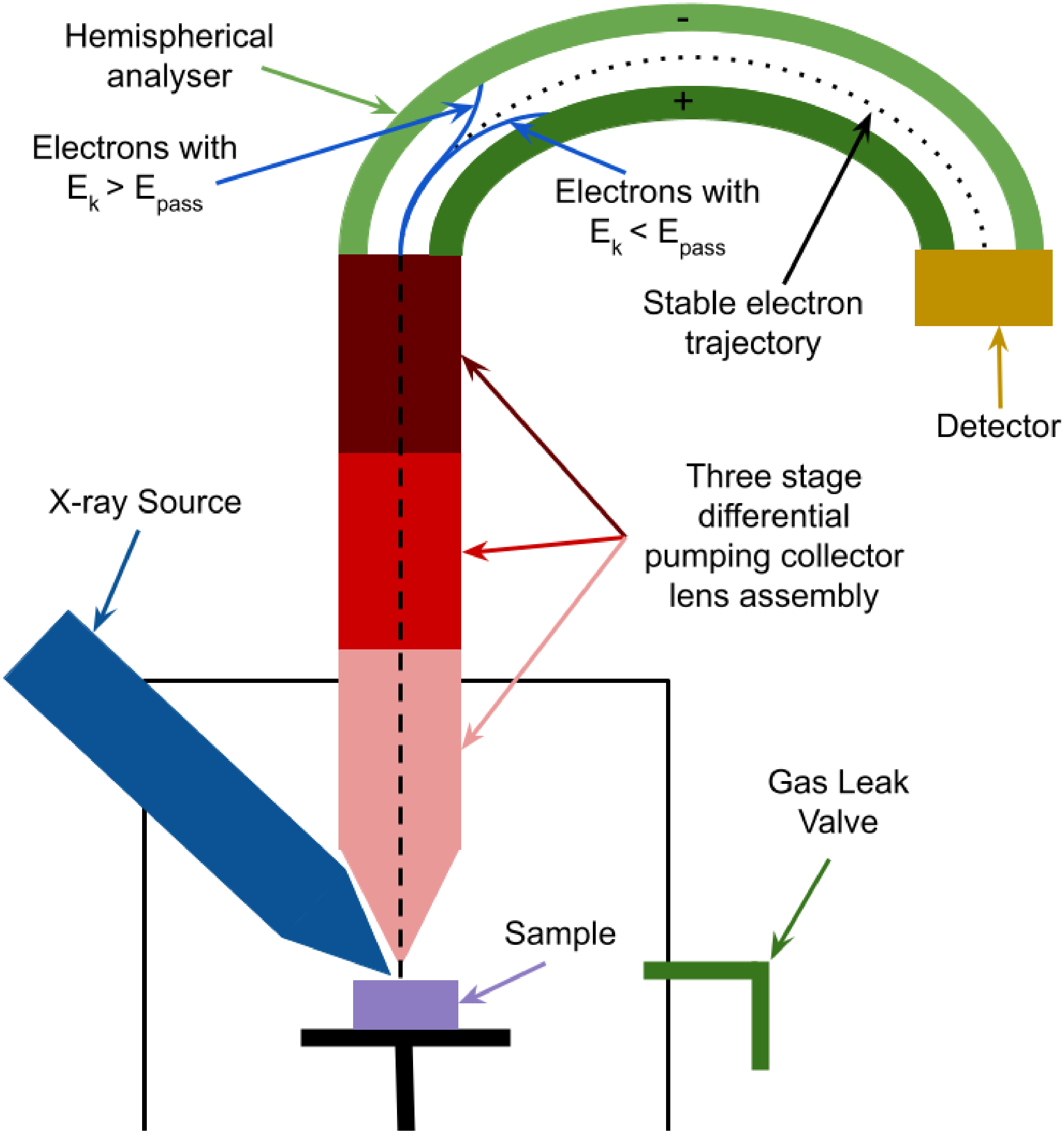

Figure 1.8: Schematic diagram of a typical NAP-XPS instrument

1.3 Preparation of samples for XPS analysis

The first stage of any X-ray photoelectron spectroscopy experiment should always be ensuring that the equipment is well calibrated and fit for purpose. Calibration of an XPS spectrometer is required, at the simplest level, across two axis: the binding energy (BE) of the escaping photoelectrons, and the intensity (number detected) [64]. Given the lack of any internal "standard" that can be incorporated into the sample under analysis and the work function difference between compounds, BE calibration is not always a trivial task. One of the most common methods employed for the calibration of BE in XPS analysis is to calibrate the resultant spectrum to the BE position of an *adventitious carbon* peak. A method first described by Siegbahn et al. in the 1960s, and further incorporated into an ISO standard [65, 66]. Though this has some major drawbacks as a *standard* method. For example, in a well designed vacuum experiment, with an ultra clean sample, there may be no adventitious carbon present. Furthermore the work of Greczynski and Hultman has shown that the adventitious carbon peak is not constant, and can vary between different samples by up to 2.66 eV [67, 68]. An alternative method is to relate the results to calculated binding energies in some way, such as by density functional theory (DFT) [60, 69]. Greczynski and Hultman argue that alignment of the Fermi level in the sample spectrum to the Fermi level of the instrument sample holder is a more robust methodology [67, 68]. While this argument is not incorrect it is not always viable, for example, when the sample is an insulating compound.

The intensity calibration is related to the term *transmission function*, which is specific to a given spectrometer. This is required to ensure that spectra recorded on one instrument, are comparable to those acquired on another spectrometer. Indeed, that even those spectra recorded on a given instrument are comparable to a different point in the life time of that instrument. This is done by measuring the total count of electrons as a function of electron kinetic energy, of a known standard, such as Ar^+ sputter cleaned Au. The total amount detected on a given spectrometer is then adjusted to match a calibration standard produced by a known trusted body, for example, the National Institute of Standards and Technology (USA) [70, 64, 71, 72].

Given the fact that XPS is a surface sensitive technique, the sample under analysis must, at the surface, be as free of contamination as possible. While this does not necessarily mean contamination that is an inherent part of the sample, for example, carbon in carbon steel would not be a contaminant. It means principally surface adsorbed species. Most commonly, it means hydrocarbon contamination, this is typically expressed however, in terms of relative atomic carbon concentration, as XPS is incapable of detecting hydrogen [73]. A number of different methods have been shown to be effective in cleaning samples such that all adventitious carbon is removed. Organic solvents such as trichloroethylene are ideal for removal of contaminants [74], however, trichloroethylene is classified as a class two carcinogen [75]. It has been shown that similar though not as high-quality cleaning can be achieved through the use of hydrofluoroether [75]. UV-ozone cleaning can also be used whereby oxygen is flowed into a chamber and irradiated with ultraviolet light at 184.9 nm and 253.7 nm causing the oxygen to form ozone (O_3) [76]. The ozone reacts with the hydrocarbons and splits the intermolecular bonds releasing oxidised carbonaceous gas of the form CO_x [76]. Another heavily used method for surface cleaning is plasma treatment, typically, but not always using argon or oxygen plasma. Neon, helium, and nitrogen plasmas also see fairly common use [77, 78, 79, 80, 81, 82]. Yamamoto *et al.* provide a good comparison between oxygen plasma cleaning, and argon plasma cleaning [82]. Here they show that while oxygen cleaning may be more efficient for the removal of adventitious carbon, there are some major drawbacks. The largest of which is oxidation of the Au surface, such that Au_2O_3 formation at the surface becomes readily apparent in XPS spectra [83]. Seah and Spencer published a comprehensive study detailing a number of cleaning methods to remove carbonaceous contamination from ultra-thin SiO_2 on an Si substrate [84]. In this study the most effective methods for removing carbonaceous contamination all involved the use of UV/O_3. Where the most effective method was UV/O_3 combined with distilled water and an Ar gas jet. The next most effective method was UV/O_3 alone. UV/O_3 was in fact so effective, that even when a thumbprint was applied to the sample, UV/O_3 resulted in less than a 0.3 nm increase in contaminating carbon layer thickness vs. the most effective method [84]. While the methods described by Seah and Spencer work very well for Si samples, and likely metal crystals, the use of UV/O_3 on an organic sample will be useless, as it will destroy the sample in addition to the carbonaceous contamination.

1.4 Conclusions

1.4.1 Research Question

Taking all of these motivations into account, the principal reason for engaging in this research is to aid in the development of a protocol for determining minimum concentrations of excipient compounds in multicomponent chemical products. Specifically, minimum concentrations of compounds intended to produce surface effects, for example, dispersants. Therefore, the organic crystalline "active" compound *paracetamol*, also commonly known as *acetaminophen*, was selected as a model active ingredient, in combination with *Tergitol NP-9* a nonyl phenyl ethoxylate, non-ionic surfactant with a nine membered ethoxylate chain as a model excipient. The research question being addressed by this work is;

"Can nonyl phenyl ethoxylate surfactant adsorbed to a paracetamol single crystal surface be both detected and quantified by near-ambient pressure X-ray photoelectron spectroscopy?"

1.4.2 Aims and Objectives

In order to address the research question, and provide useful results the following aims and objectives were decided upon;

- **Aim 1** Determine a baseline spectrum for ultra clean paracetamol, by X-ray photoelectron spectroscopy.
  - **Objective 1** The first objective to achieve this aim, is to acquire paracetamol spectra using a laboratory XPS source, and a thin film of paracetamol as the sample.
  - **Objective 2** The second objective is to describe the obtained spectra with the aid of density functional theory. This is in order to ensure that the interpretation of the spectra is grounded in theory and that both theory and experiment are aligned.
- **Aim 2** Determine a method for the removal of adventitious carbon from the surface of paracetamol single crystals.
  - **Objective 1** Screen multiple solvents for their ability to remove adventitious carbon without damaging the surface of the paracetamol.
  - **Objective 2** Determine the degree to which adventitious carbon is removed from the surface of paracetamol, by XPS.
- **Aim 3** Quantify the level of surfactant adsorbed to a paracetamol single crystal surface.
  - **Objective 1** Obtain XPS spectra of the raw *Tergitol NP-9* liquid.
  - **Objective 2** Obtain XPS spectra from the surface of a clean paracetamol single crystal with adsorbed *Tergitol NP-9* surfactant.
  - **Objective 3** Quantify the number of paracetamol molecules, and *Tergitol NP-9* molecules present in the analysis.

Chapter 2

The XPS Spectrum of Pure Paracetamol

2.1 Introduction

2.1.1 Motivation

Paracetamol (acetaminophen), was selected as the model system for the work in this dissertation. It is a well-characterised drug API [85, 86, 28]. It was decided that a reference spectrum for a known, clean paracetamol sample should be obtained. This could then be used to make decisions about the quality of data obtained from future analyses. In order to obtain the clean spectrum, it was decided to deposit from the gas phase, under UHV conditions, as the optimal method for ensuring no surface contamination would be present. It was also decided that interpretation of the resultant spectra should be well grounded in theory, i.e. backed up by density functional theory (DFT) calculations that accurately represented the solid form.

2.1.2 Aims

The aims of this package of work are:

- To obtain XPS spectra of paracetamol under ultra-high vacuum conditions. To include O1s, N1s, C1s, and wide survey scans.
- To determine appropriate input geometries for atom centred density functional theory calculations.
- To determine 1s orbital binding energies through the use of density functional theory.
- To relate the density functional theory outputs to the experimentally obtained XPS spectra of paracetamol.

2.2 Ultra-High Vacuum XPS of Paracetamol

2.2.1 Materials and Methods

Spectra were acquired on an Omicron Nanotechnology XM1000 MKII XPS instrument, equipped with an Al Kα X-ray source and monochromator. It was also equipped with a Sphera EAC 2000 hemispherical analyser equipped with a seven channel, multichannel detector. Spectra were acquired for an Au(111) single crystal substrate after exposure to an ambient atmosphere with a pass energy of 50 eV, dwell time of 0.2 s, and step of 0.5 eV, at a pressure of $\sim$3x10^{-9} mbar, across a binding energy range of 1336.7 – 0 eV. The Au(111) crystal was then moved to a preparation chamber and subject to Ar sputtering at an Ar pressure of $\sim$8x10^{-6} mbar with an electron beam set to an emission voltage of 1 keV at an emission current of 10 μA for 20 min. The Au(111) substrate was then heated to 700 °C and annealed for 20 min. Low energy electron diffraction (LEED) at 79.1 eV was used to confirm a clean Au(111) structure had been obtained [87]. Further XPS spectra were obtained to confirm no contaminants were present on the surface. The initial deposition experiments used a Knudsen cell, pictured in figure 2.1. The paracetamol is held in a small envelope connected to two electrodes. As a current is passed through the electrodes, the envelope heats up and the paracetamol contained within is vaporised under UHV conditions. A thermocouple monitors the temperature of the envelope. This Knudsen cell was then incorporated into UHV apparatus below a chamber designed to suspend the Au(111) substrate above, separated by a gate valve.

The second deposition experiments used a Knudsen cell with extended and insulated electrodes, pictured in figure 2.2, placed in UHV apparatus below a chamber designed to suspend the Au(111) substrate above; a cartoon diagram of this set-up is shown in figure 2.3. The paracetamol containing envelope (green) is heated and the paracetamol vaporised. The concentration of paracetamol is monitored by a mass spectrometer (blue). Vaporised paracetamol can then deposit on to the Au(111) substrate surface (yellow). UHV pumps are implied. A quadrupole mass spectrometer was attached to the dosing chamber to monitor the level of paracetamol present in the chamber. A small envelope was held in the cell and filled 2/3 with paracetamol powder ($\sim$15-20 mg). This was heated at a starting pressure of 8.4x10^{-7} mbar to a temperature of 56.6 °C and held for 30 min to an ending pressure of 7.7x10^{-7} mbar. At this point the mass spectrum indicated that pressure in the chamber was a result of gaseous paracetamol and a trace amount of paracetamol derived contaminants. The Au(111) substrate was held above the paracetamol containing envelope in the opposite orientation to the previous experiment (i.e. with the sample holder between the substrate and the envelope).

Paracetamol survey spectra from the first deposition experiments were obtained by XPS at a pressure of $\sim$2x10^{-9} mbar, at a pass energy of 50 eV, dwell time of 0.2 s,

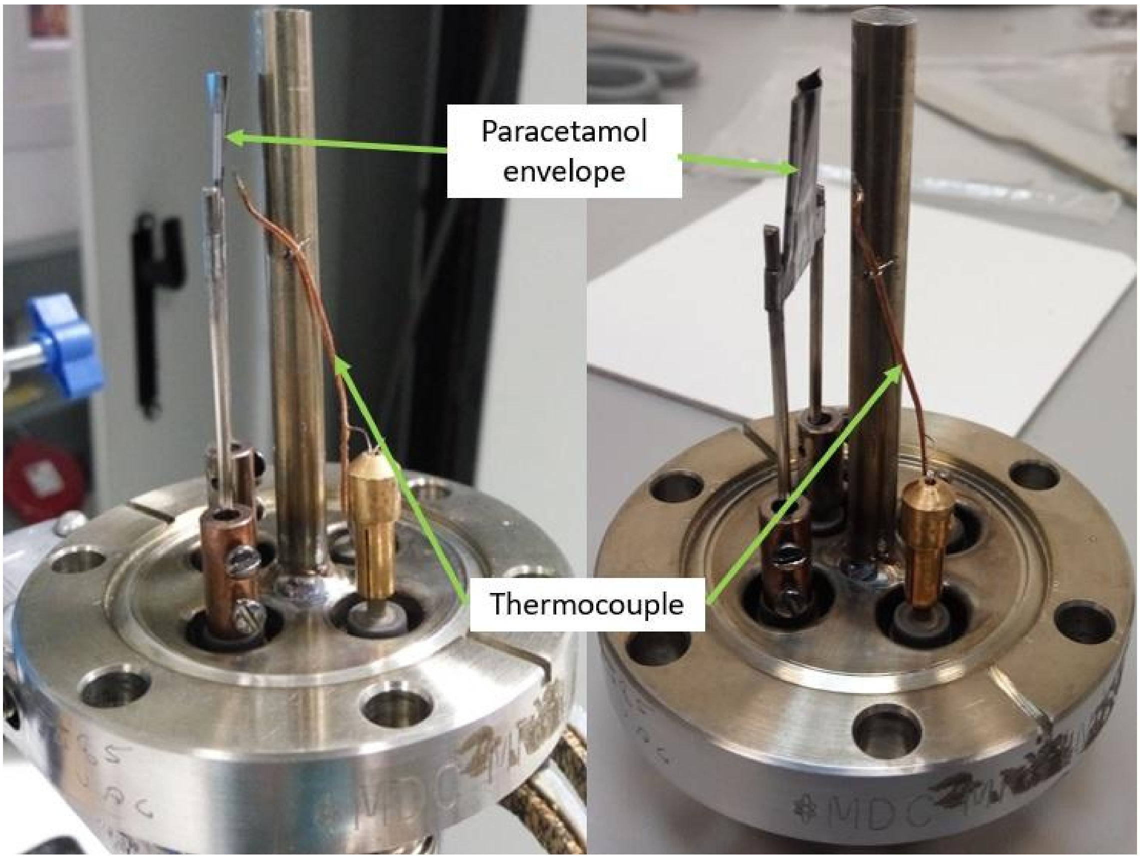

Figure 2.1: Knudsen cell for evaporation of paracetamol

and a step of 0.5 eV, across a binding energy range of 750 eV – 0 eV. Core level scans were performed at a pass energy of 20 eV, a dwell time of 1 s and a step of 0.2 eV across a binding energy of ±3 eV of identified peak centroids in the survey scans. Paracetamol survey spectra from the second deposition experiments were obtained by XPS at a pressure of $\sim$2x10^{-9} mbar, at a pass energy of 50 eV, dwell time of 0.2 s, and a step of 0.5 eV, across a binding energy range of 750 eV – 0 eV. Core level scans were performed at a pass energy of 20 eV, a dwell time of 1s and a step of 0.2 eV across a binding energy of ±3 eV of identified peak centroids in the survey scans.

Peak fitting and background assignment was carried out using the CasaXPS software version 2.3.19. Quantitative analysis was carried out through the use of the Python 3 programming language via Jupyter notebooks [88] using the SciPy [89], NumPy [90], Pandas [91], and Matplotlib [92] libraries. The survey spectra were calibrated by setting the C1s peak to 285 eV binding energy before background subtraction. Shirley backgrounds [54] were applied to the oxygen and carbon peaks, while a linear background was applied to the nitrogen peak. The elements were then corrected for photoionisation cross-section using the values provided in the literature [56]. High-resolution spectra were further fitted with pseudo-voigt functions with a 30% Lorentzian contribution. The full-width at half-maximum (FWHM) of the peaks was constrained while the position and height of the peaks was left to the fitting to determine. Functions were added to

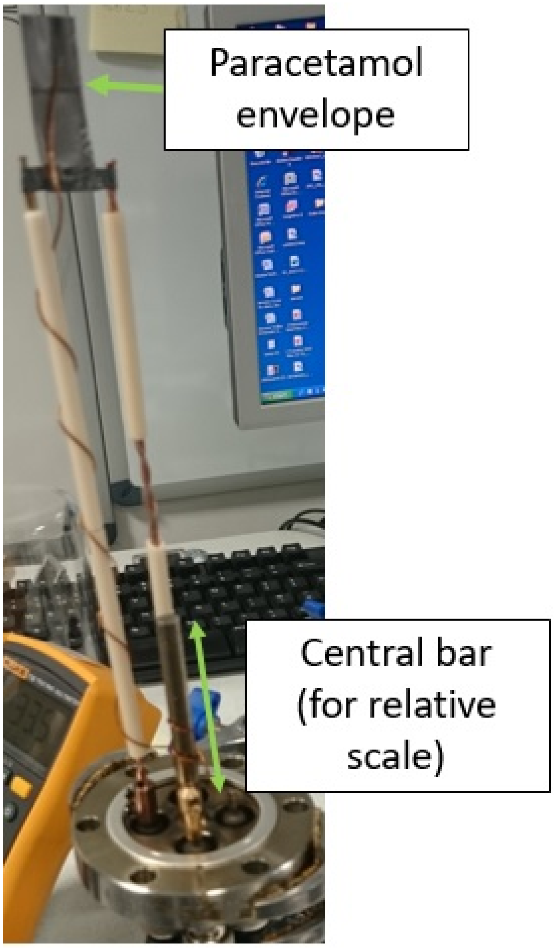

Figure 2.2: Extended Knudsen cell for paracetamol evaporation

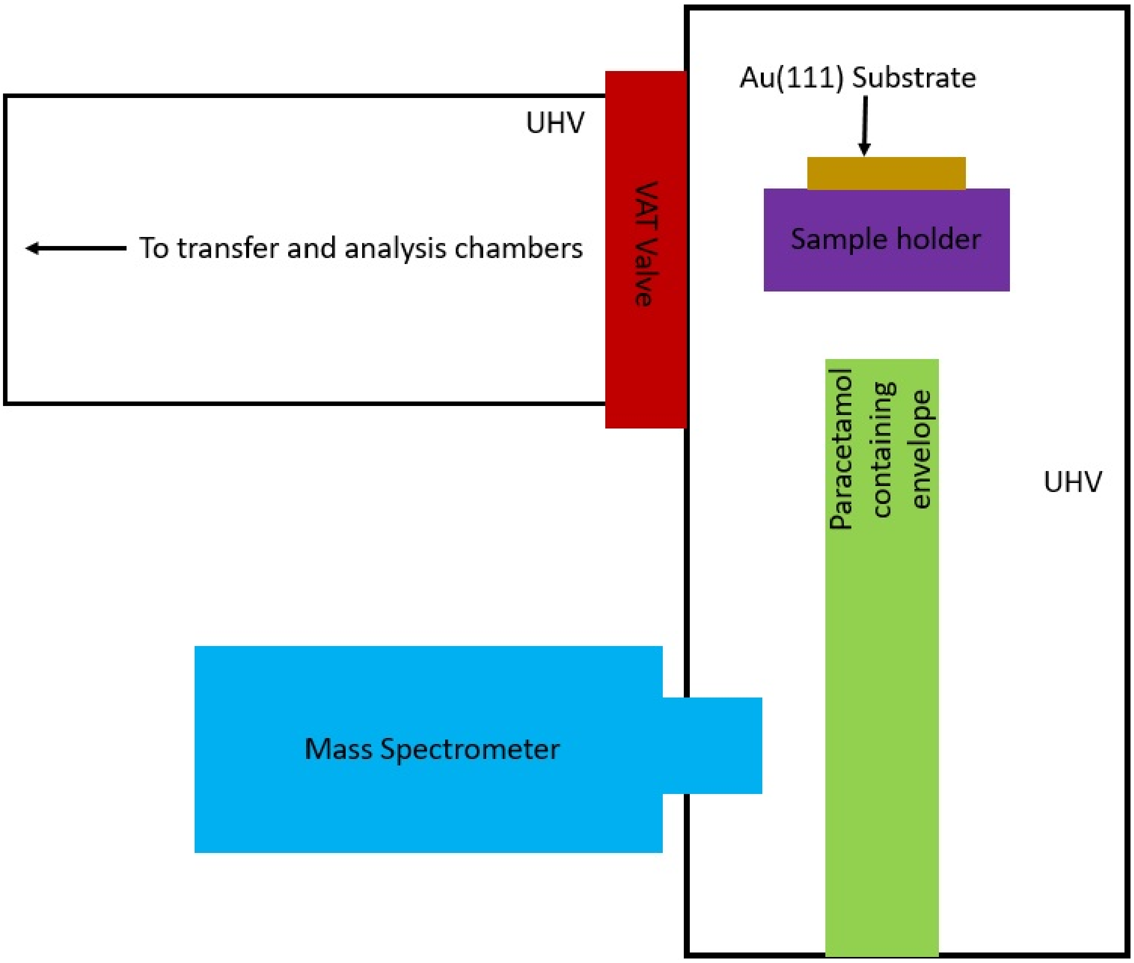

Figure 2.3: Schematic diagram of final paracetamol deposition set-up

the fit sequentially until no better fit could be obtained by adding additional peaks, and no absurd peaks could be added. The goodness of fit was determined by the closeness of an R^2 to 1. An absurd peak in this context is defined as a peak with a FWHM <0.5 eV. The FWHM constraint was initially set low (0.5 eV) for all peaks, and gradually increased until no more than one peak was bound by the constraint. No constraints were applied to the nitrogen peak. After fitting, the high-resolution C1s spectra were then calibrated by setting the carbonyl function at the high binding energy side of the spectra to 287.7 eV. The remaining N1s, and O1s spectra were then calibrated by determining the difference between the measured position of the carbonyl function, and the calibrated position.

2.2.2 Results

Separate survey spectra were obtained from three different positions across the surface of the vacuum deposited paracetamol. A representative survey spectrum is shown in figure 2.4. The only peaks visible in the spectrum were those from carbon, nitrogen, and oxygen. The 1s peaks are labelled in the figure with arrows pointing to the respective peaks. Quantitative analysis was carried out on each survey spectrum, the results of which are tabulated in table 2.1.

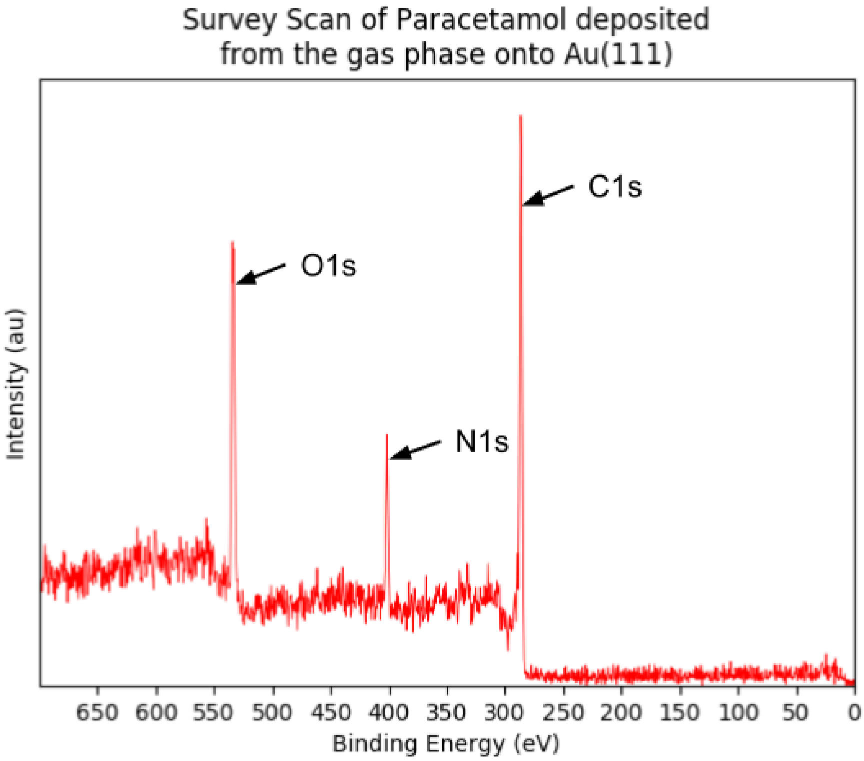

Figure 2.4: Representative survey scan of paracetamol on Au(111) deposited from the gas phase

Table 2.1: Elemental concentrations of paracetamol deposited from the gas phase on Au(111)

Element	**Theoretical %**	**Experiment 1 %**	**Experiment 2 %**	**Experiment 3 %**
C	73	74	73	73
N	9	9	9	9
O	18	17	18	18

The values shown in table 2.1 give a mean C concentration of 73±0.3%, a mean N concentration of 9%, and a mean O concentration of 18±0.4%. The high-resolution scan of the C1s peak was fit with five peaks, four of roughly similar intensity, and one of much greater intensity. The very broad peak at the highest binding energy is generated as a result of the so-called “shake-up” that typically accompanies aromatic ring structures [93].

The C1s high-resolution fits can be seen in figure 2.5. Figure 2.5 shows the C8 methyl carbon (blue) at 283.6 eV, the shake-up at 290.6 eV, the C aromatic peak (orange) at 284.6 eV is the contribution from the four aromatic carbons that only form part of the ring structure and are not bonded to any other atoms outside the ring. The C hydroxyl peak (cyan) is at 285.8 eV, while the C amide peak (magenta) at 285.1 eV originates at the carbon bonded to both the ring and a nitrogen atom. Finally, the C carbonyl peak (green) is at 287.7 eV. Peak centroids are also shown in table 2.2.

Table 2.2: C1s fitted peak positions for paracetamol from UHV experiments

Atom	**Binding Energy (eV)**
C Aromatic	284.6
C Methyl	283.6
C Amide	285.1
C Carbonyl	287.7
C Hydroxyl	285.8

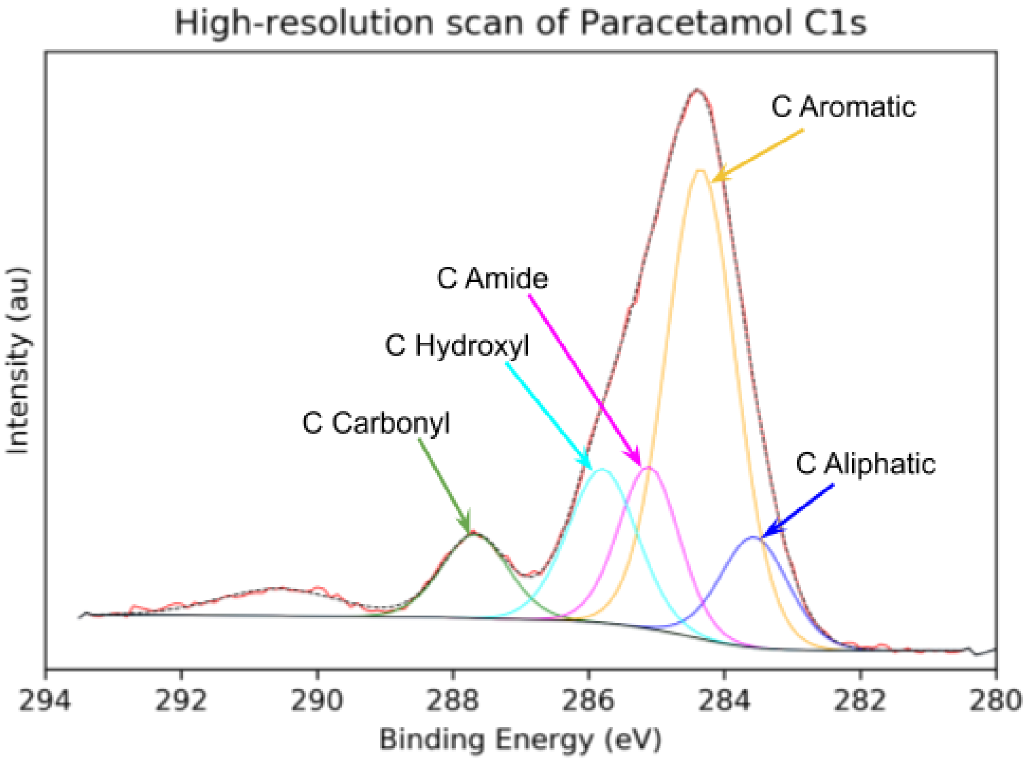

Figure 2.5: High-resolution scan of C1s acquired from paracetamol on Au(111) deposited from the gas phase

The O1s high-resolution spectra was fit with two peaks of roughly similar intensity. The

O hydroxyl peak (blue) at 532.6 eV, and the O carbonyl peak (green) at 531.2 eV. The O1s spectrum can be seen in figure 2.6. Whilst the N1s peak was fit with a single peak at 399.8 eV and can be seen in figure 2.7 (blue).

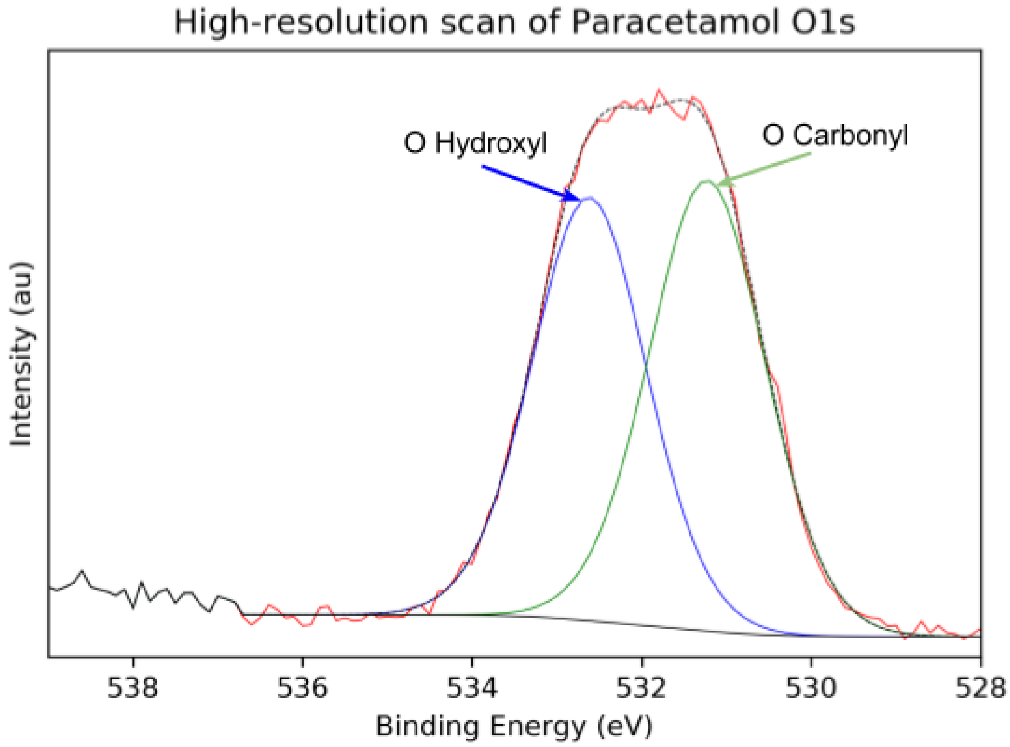

Figure 2.6: High-resolution scan of O1s acquired from paracetamol on Au(111) deposited from the gas phase

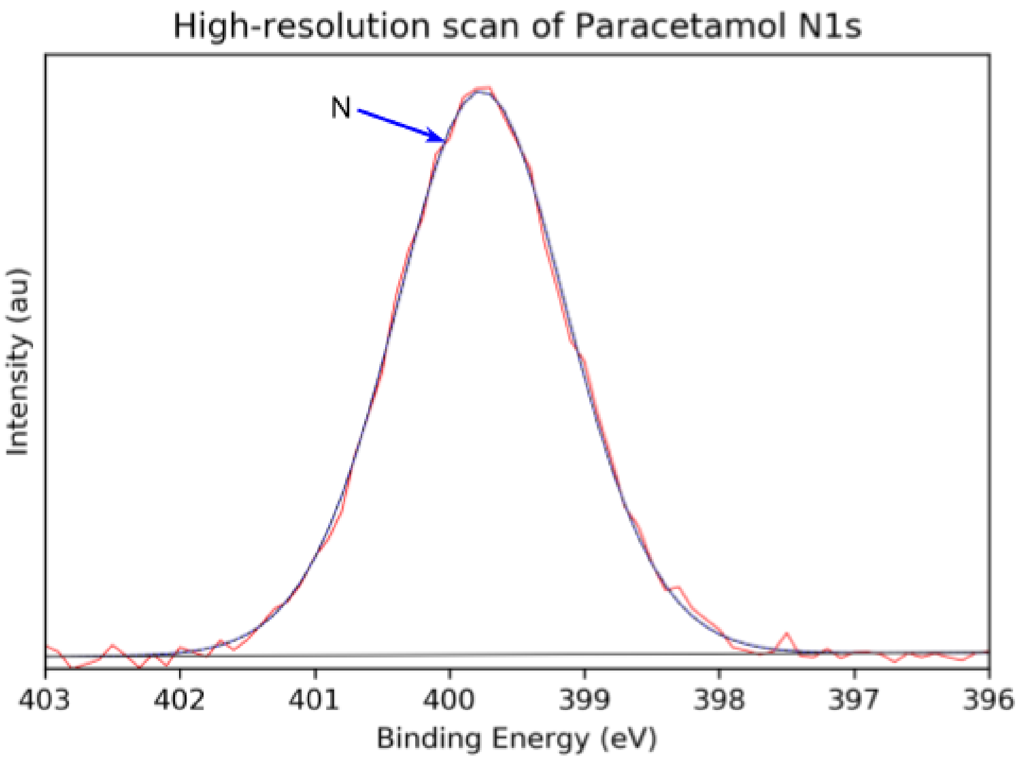

Figure 2.7: High-resolution scan of N1s acquired from paracetamol on Au(111) deposited from the gas phase

2.2.3 Discussion

The survey spectra were the key indicators of ensuring that an ultra pure paracetamol sample had been obtained, and that it had completely covered the Au(111) substrate, to a thickness level that would leave the Au undetectable by XPS. Across all scans the spectra were highly reproducible and showed that the detected atomic concentrations were in line with the expected stoichiometry of paracetamol. In the case of the amide, carbonyl, hydroxyl, and methyl peaks, fitted positions were broadly in line with those reported in one previous study [94]. However, they differed greatly from values published in the literature [95]. The greatest deviation from both, is the fitting of an additional peak at the low binding energy side of the main peak. Given all other carbon environments in the paracetamol molecule can be accounted for, this was assigned to the methyl carbon in the paracetamol molecule. To explain this low-binding energy methyl carbon the density functional theory investigation will be discussed later in this chapter. It must be noted however, that a direct comparison to either of the previously published spectra is not possible, given the sensitivity of XPS to surfaces and the fact that ultra pure samples were not obtained by either [94, 95]. In the case of the N1s spectra, there was little deviation from that seen in previous studies, and was as expected with one peak fitted. The O1s spectra were also largely inline with two peaks fitted to the spectra in positions that were expected. They were also expected to have roughly similar intensity.

In summary, vacuum deposition of the paracetamol on Au(111) is a good method for obtaining ultra pure paracetamol samples suitable for surface science analysis. No contamination was detected in any spectrum. Furthermore, expected stoichiometries of all paracetamol constituent atoms were detected in all survey spectra. There were some unexpected findings in the C1s high-resolution spectra, which require explanation, it is expected however, that this will be resolved with the aid of theoretical calculations.

2.3 Density Functional Theory Analysis of Paracetamol Form I

2.3.1 Methods

A number of density functional theory (DFT) calculations were carried out using the ORCA 4.0 QM software suite [50], *undertaken on ARC3, part of the High Performance Computing facilities at the University of Leeds, UK.*

Solid Form Approximation Geometry

In order to approximate the solid form of paracetamol, a molecular cluster (figure 2.8) was constructed from the paracetamol crystal structure HXACAN28 in the Cambridge Structural Database (CSD) [96, 97]. The cluster was constructed by first creating a crystal slab of the (011) facet of paracetamol, using the Mercury software package [98]. The resultant geometries were then saved in the mol2 format, and opened in the Avogadro molecular viewer software [99]. Here, a molecule reasonably central to the slab was selected to be the *"molecule of interest"*. Starting from the outside edges of the slab, molecules were sequentially removed until the only molecules remaining were the molecule of interest, and other molecules with a direct intermolecular contact with the molecule of interest.

Convergence Testing and Correction/Approximation Testing

The resultant geometry was used as the basis for creating input files for the ORCA software. The first set of input files created were done so according to the following parameters;

- All input files were created to use the B3LYP hybrid exchange-correlation functional [100].
- For each of the following basis sets, def2-SVP, def2-TZVP, def2-TZVPP, def2-QZVP [101] an input file was created.
- Once the basis set convergence had been determined, an input file was created using Grimme's D3 dispersion correction scheme [102].
- Once the basis set convergence had been determined, an input file was created using the RijCosX approximation [103], using the def2/J auxiliary basis set.
- Once the basis set convergence had been determined, an input file was created using, Grimme's D3 dispersion correction scheme [102], an RijCosX approximation [103], and using the def2/J auxiliary basis set.

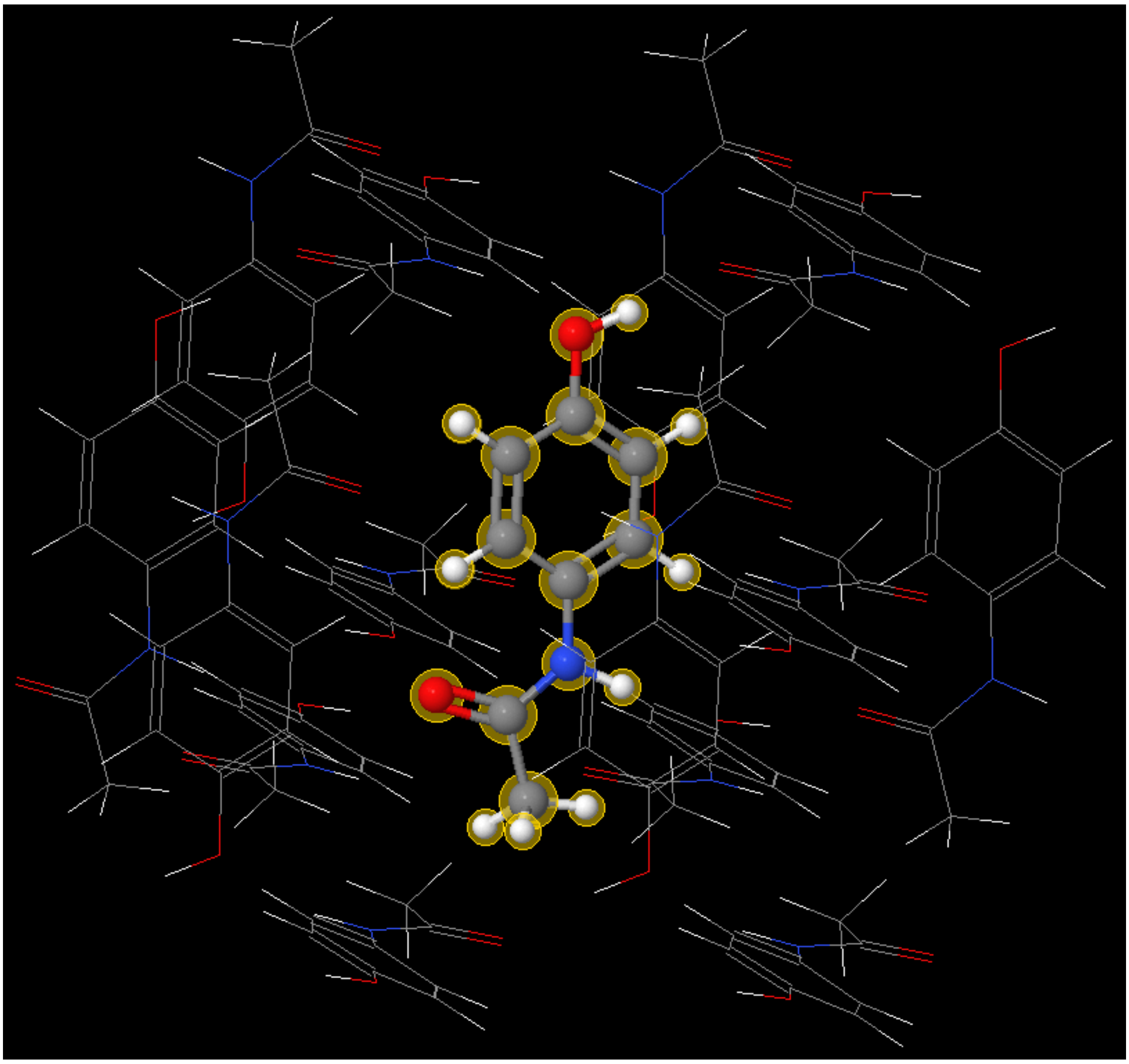

Figure 2.8: Paracetamol cluster as an approximation of the solid form

Calculations with a total of 7 separate input files were performed on the ARC3 high-performance computer (HPC) at the University of Leeds, Leeds, UK., using 24 CPU cores and 128 GB of system memory (A single compute node on the ARC3 system). The convergence criteria for these calculations was set at a change of less than a 0.1 eV in the 1s orbital energies.

DFT Calculations on Paracetamol

Further input geometries were derived from the solid form approximation described earlier.

- All molecules with the exception of the molecule of interest were removed. (Single molecule calculation.)
- All molecules not involved in a hydrogen bond with the molecule of interest were removed. (Leaving the four hydrogen bonded molecules, and the molecule of interest.)
- All molecules involved in a hydrogen bond with the molecule of interest were removed.
- Molecular pairs in which both molecules were considered the "molecule of interest". (For example, if a hydrogen bond consists of an amide donor and a hydroxyl acceptor, then the "molecule of interest" with respect to a satisfied amide hydrogen bond, is the amide donor molecule.)
- Finally, each hydrogen bonding molecule to the molecule of interest was sequentially removed. Resulting in four separate input geometries.

Each of these geometries was used to create input files specifying calculations using the B3LYP exchange-correlation functional, the def2-TZVP basis set, and the RijCosX approximation using the def2/J auxiliary basis set. Each of these calculations was then run on the ARC3 high-performance computer (HPC) at the University of Leeds, Leeds, UK using 24 CPU cores, and 128 GB of system memory (A single compute node on the ARC3 system).

2.3.2 Results

Convergence Testing and Correction/Approximation Testing

The first set of calculations were done to determine basis set convergence. 1s orbital energies for each of the paracetamol atoms were calculated using the input geometry seen in figure 2.8. These were then calibrated by setting the C carbonyl to 287.7 eV, and tabulated. Table 2.3 shows the 1s orbital energies, as calculated at each of the basis sets used.

Table 2.3: 1s orbital binding energies (eV) for atoms in paracetamol calculated using different basis sets with B3LYP

The table shows that at the def2-TZVP basis level, there are no further changes in any of the calculated binding energies.

Atom	def2-SVP	def2-TZVP	def2-TZVPP	def2-QZVP
C Hydroxyl	286.0	286.0	286.0	286.0
C Aromatic	284.4	284.4	284.4	284.4
C Amide	285.4	285.4	285.4	285.4
C Carbonyl	287.7	287.7	287.7	287.7
C Methyl	284.5	284.4	284.4	284.4
N	398.1	398.2	398.2	398.2
O Hydroxyl	528.8	528.9	528.9	528.9
O Carbonyl	527.8	527.8	527.8	527.8

* The calculated energies are calibrated with respect to that of the C carbonyl, which was set to 287.7 eV.

The effect of the D3 dispersion correction and the RijCosX approximation, individually and in combination, using the def2-TZVP basis set on the calculated orbital binding energies was then evaluated. Results from all three of these calculations are shown in table 2.4 the table shows that to one decimal place, there is no effect on the calculated 1s binding energies of any atoms in paracetamol whether using D3 dispersion correction, RijCosX approximation, or both.

DFT Calculations on Paracetamol

The output of calculations performed on various dimer input geometries was initially calibrated by setting the C aromatic 1s orbital energy to 284.4 eV. The reason for this calibration, rather than setting the C carbonyl to 287.7 eV, is for comparison to the solid form approximation so as to make determination of orbital energies around H-bond contacts simpler. After calibration, the outputs for each calculation were tabulated and are shown in table 2.5.

Table 2.4: The effect of D3 dispersion correction and the RijCosX approximation on the 1s bind energies (eV) calculated for the atoms in paracetamol

Atom	**No Corrections or Approximations**	**D3 Dispersion Correction**	**RijCosX Approximation**	**D3 & RijCosX**
C Hydroxyl	286.0	286.0	286.0	286.0
C Aromatic	284.4	284.4	284.4	284.4
C Amide	285.4	285.4	285.4	285.4
C Carbonyl	287.7	287.7	287.7	287.7
C Methyl	284.4	284.4	284.4	284.4
N	398.2	398.2	398.2	398.2
O Hydroxyl	528.9	528.9	528.9	528.9
O Carbonyl	527.8	527.8	527.8	527.8

* The calculated energies are calibrated with respect to that of the C carbonyl, which was set to 287.7 eV.

Table 2.5: C1s orbital energies (eV) in paracetamol dimers as calculated by DFT using the B3LYP functional and def2-TZVP basis set

Where No H-Bonds 1 refers to the input geometry shown in figure 2.10 and No H-Bonds 2 refers to the input geometry shown in figure 2.11

Atom	**No H-Bonds 1**	**No H-Bonds 2**	**Amide Donor**	**O-H Acceptor**	**O-H Donor**	**C=O Acceptor**
C Hydroxyl	286.0	286.0	286.0	286.1	285.5	286.0
C Aromatic	284.4	284.4	284.4	284.4	284.4	284.4
C Amide	285.5	285.5	285.5	285.5	285.5	285.5
C Carbonyl	287.2	287.0	286.8	286.8	287.5	287.6
C Methyl	284.4	284.2	284.0	283.9	284.7	284.5

**(Calibrated to 284.4 eV as the aromatic C)*

In the case of the two No H-bonds columns in table 2.5, the first column represents a dimer where the molecules are relatively close together. The second represents a dimer where the molecules are further apart. Both were taken from the HXACAN28 unit cell, by removing the other two molecules from the geometry [97]. Figure 2.9 depicts the paracetamol form I unit cell, as taken from the HXACAN28 structure in the CSD [97], Figures 2.10 and 2.11 show the two dimers from the HXACAN28 structure, that do not have either molecule engaged in a hydrogen bond [97]. The two geometries shown in Figures 2.10 and 2.11 are referred to from now on as No H-bonds 1, and No H-bonds 2, respectively.

In the case clusters where only hydrogen bonded molecules were present, and the cluster where only the van der Waals (vdW) interacting molecules were present, only the central molecule was regarded as the "molecule of interest". In the case of both, calibration was performed in the same manner as with the dimers, in order to observe changes in

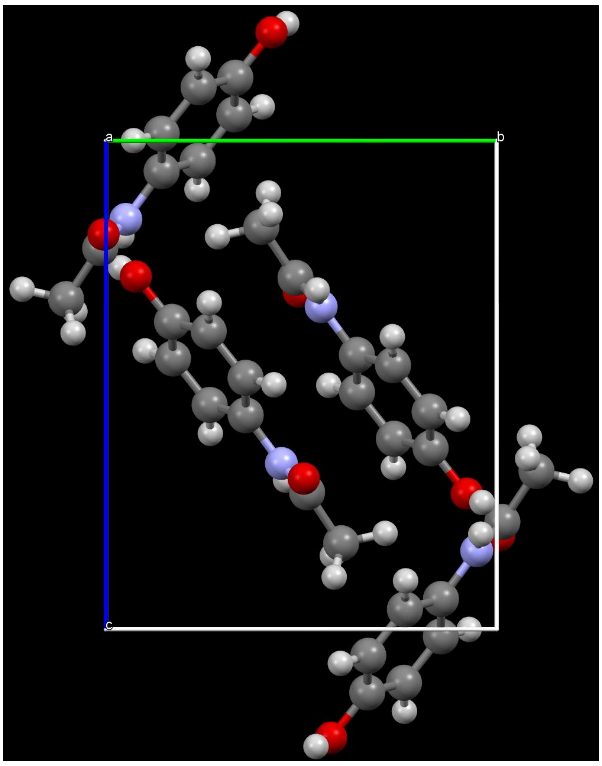

Figure 2.9: Unit cell of paracetamol form I

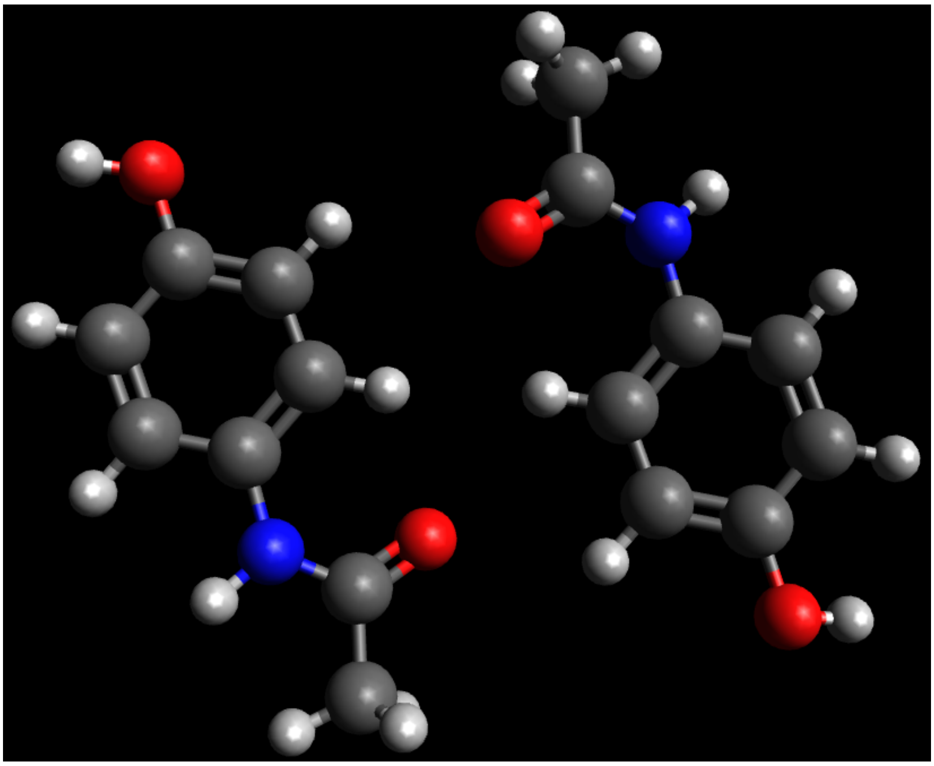

Figure 2.10: "No H-bonds 1" from the HXACAN28 structure

the hydrogen bonding atoms, with respect to the solid form approximation. Additionally calculations were done where single molecules were removed from the solid form approximation cluster. Table 2.6 shows the C1s binding energies calculated on all of these geometries. Figure 2.12 shows a molecule of interest (Highlighted blue), and all

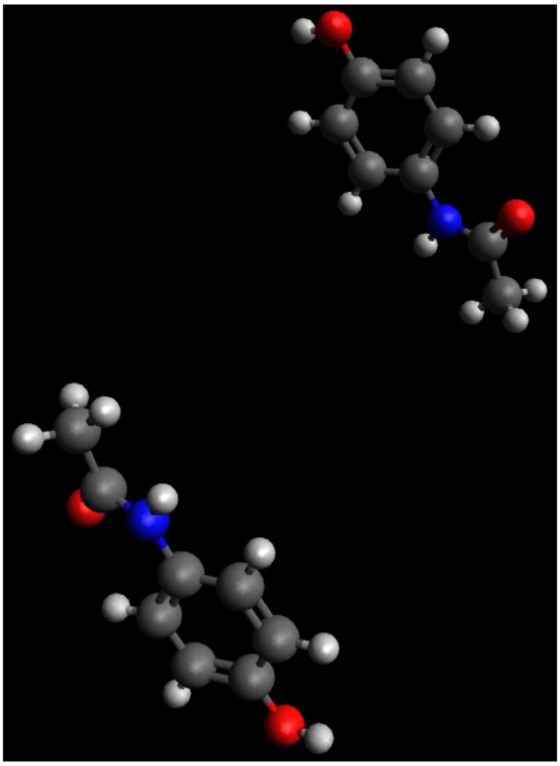

Figure 2.11: "No H-bonds 2" from the HXACAN28 structure

paracetamol molecules in the solid form approximation that make hydrogen bond contacts with the molecule of interest. Hydrogen bond contacts are shown as dashed yellow lines. Figure 2.13 shows a molecule of interest (Highlighted blue), and all paracetamol molecules in the solid form approximation that do not make hydrogen bond contacts with the molecule of interest. These are the geometries on which the H-bond only and vdW only calculations were performed.

Table 2.6: C1s orbital energies (eV) in paracetamol clusters as calculated by DFT using the B3LYP functional and the def2-TZVP basis set

Where specific molecules have been removed from a solid form approximation. For example, O-H donor indicates that this hydrogen bond interaction is not satisfied in the molecule of interest.

Atom	**O-H Donor**	**O-H Acceptor**	**Amide Donor**	**C=O Acceptor**	**H-Bonds Only**	**VdW Only**	**Solid Form**
C Hydroxyl	286.1	285.9	286.0	286.0	286.0	286.0	286.0
C Aromatic	284.4	284.4	284.4	284.4	284.4	284.4	284.4
C Amide	285.4	285.5	285.6	285.4	285.5	285.5	285.4
C Carbonyl	287.6	287.9	287.9	287.3	287.6	287.5	287.7
C Methyl	284.2	284.7	284.7	284.2	284.6	284.4	284.4

**(Calibrated to 284.4 eV as the aromatic C)*

The final set of results were obtained from an input geometry using only the molecule of interest. Results from the calculation are shown in table 2.7 along side the results from

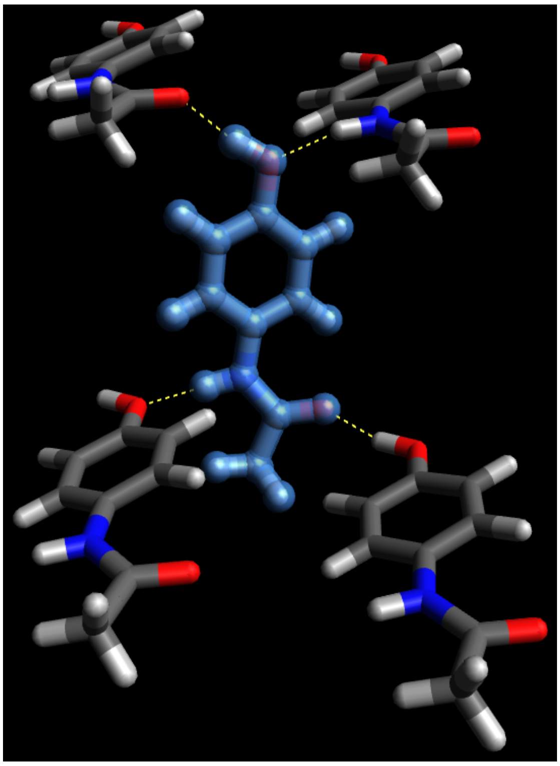

Figure 2.12: Hydrogen bonds only in the solid form approximation of paracetamol form I

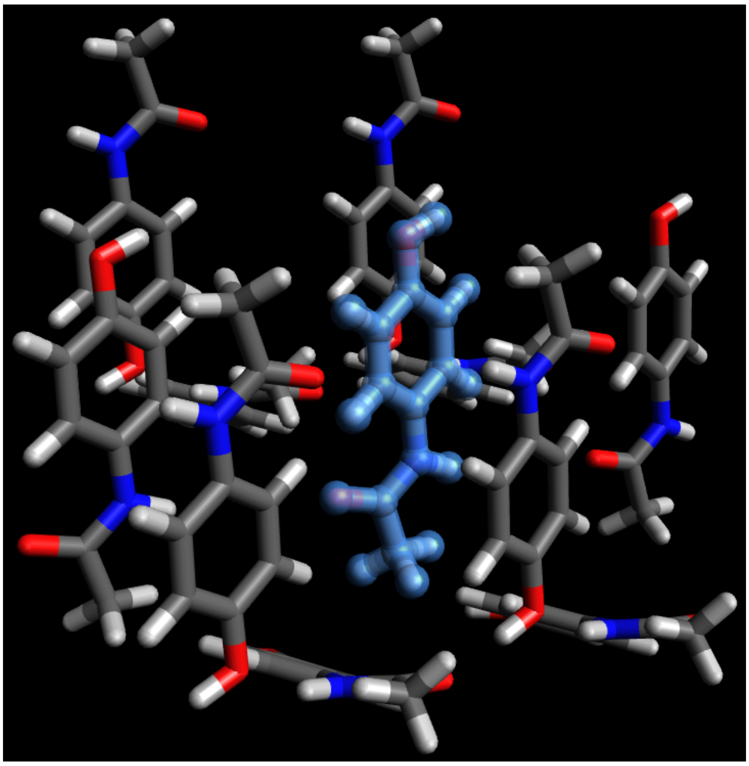

Figure 2.13: van der Waals contacts only in the solid form approximation of paracetamol form I

the solid form approximation.

Table 2.7: C1s orbital energies in a single paracetamol molecule as calculated by DFT *(Calibrated to 284.4 eV as the aromatic C)*

Atom	**Single Molecule**	**Solid Form Approximation**
C Hydroxyl	286.0	286.0
C Aromatic	284.4	284.4
C Amide	285.5	285.4
C Carbonyl	287.0	287.7
C Methyl	284.2	284.4

2.3.3 Discussion

Single Molecule vs. Solid Form Approximation Cluster

The rationale for choosing atom centred DFT for performing these calculations, as opposed to using plane-wave DFT methods, was principally due to the trade off between speed and accuracy. While plane-wave DFT codes are generally periodic in nature, and take crystallographic parameters, such as the unit cell vectors/angles, most codes are not "all electron codes" [104, 105, 51]. As a result, these methods use so called "pseudopotentials" [106] to approximate core electrons to allow valence electrons to be modelled in a time efficient manner. While it has been shown that these methods are appropriate for some calculations that involve core electrons, such as the calculation of K-edge absorption spectra [107, 108, 109], in this instance it was decided that these methods would be inappropriate. The methodology used was specifically designed to calculate the 1s orbital binding energies, and hence, an approximation was not the desired outcome. All electron plane-wave DFT codes do indeed exist, but take considerably longer to complete the calculations or have prohibitive licence costs [110]. At the same time, linear combination of atomic orbital (LCAO) codes with the ability to perform periodic calculations also exist, but again, often have prohibitive licence costs associated with them [111].

Given that the O1s and N1s environments were as expected, the DFT analyses were done in order to explain the deviation from the expected result in the clean C1s spectra of paracetamol, by XPS. The results of the DFT analyses in the solid form approximation and the single molecule when compared, showed little difference in the hydroxyl and aromatic carbon 1s binding energies. The other carbon 1s environments, showed significant differences between the single molecule and solid form approximation carbonyl carbon 1s binding energies. The C1s binding energy of the carbonyl in the single molecule was redshifted by 0.7 eV. This shows a significant increase in the electron density surrounding the atom, in the single molecule calculation. The methyl carbon in the single molecule having a binding energy 0.2 eV lower than the aromatic carbons was surprising. It would not be expected that a methyl carbon would possess greater electron density than an aromatic carbon. When the molecular orbitals are visualised however, it becomes clear that the conjugated π system in the molecule extends to encompass the methyl carbon. This trend continues until the HOMO orbital, in which the methyl carbon has zero electron density. Figures 2.14 and 2.15 show the first ten low energy states above the 1s orbitals, and the HOMO state, respectively.

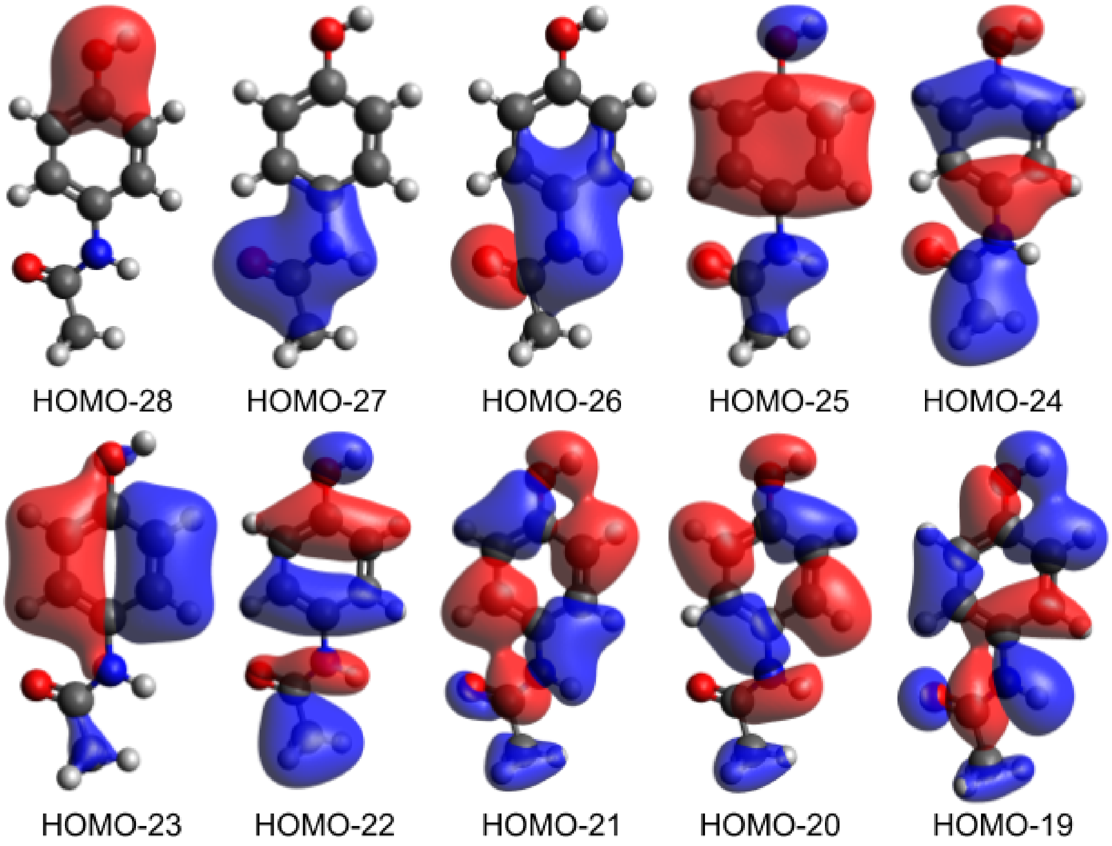

Figure 2.14: First ten low energy states in a single paracetamol molecule

In the solid form approximation cluster, when molecular orbitals are visualised, it is apparent from a small subset close to the 1s orbitals in energy, that hydrogen bonding in the solid form plays a major role and has a large effect on the electron distribution within the conjugated π system. In the first four HOMO states following the 1s orbitals, similar orbitals to the HOMO-28 and HOMO-27 in the single molecule are seen. However in the solid form approximation, below these two, but above the 1s orbitals, hydrogen bonded orbitals were calculated.

In the case of the hydroxyl moiety, it is acting as a hydrogen bond donor, and hence drawing some of the electron density from the accepting carbonyl in a neighbouring molecule toward the ring.

The carbonyl moiety is acting as a hydrogen bond acceptor, with a neighbouring molecule's

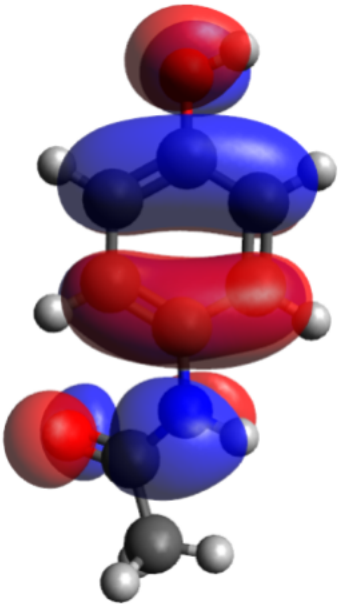

Figure 2.15: HOMO state in a single paracetamol molecule

hydroxyl drawing some of the electron density away from the methyl carbon. Figure 2.16 shows the four lowest energy HOMOs that have electron density around the central molecule in the solid form approximation. C and D are reminiscent of the HOMO-28 and HOMO-27 in the single molecule calculation. A and B occur at lower energies, and show hydrogen bond orbital overlap with neighbouring molecules. Here A and B have some covalent character which perturbs the electronic structure of the molecule. All images were generated from the solid form approximation calculation, various molecules were removed from the figures to aid clarity.

With reference to table 2.7, it is therefore likely that the distribution of electrons throughout the molecule's conjugated π system is stabilised by the presence of surrounding molecules in the solid form. Though whether or not this is caused by the presence of the hydrogen bond network, the van der Waals dispersion forces, or both will presently be explored.

Hydrogen Bonds and van der Waals Dispersion Forces

With reference to table 2.6, the initial results of note are a comparison between the columns **Solid Form**, **vdW Only**, and **H-bonds Only**. Using the solid form approximation as reference point, one can see the effect on the C1s binding energies of removing either all of the hydrogen bonding molecules, or all of the van der Waals interaction forces. The hydroxyl, aromatic, and methyl carbon binding energies do not change as a result of removing all hydrogen bond interactions from the molecule of interest in the solid form approximation. The amide carbon is blueshifted by 0.1 eV and the carbonyl carbon is redshifted by 0.2 eV. With only the hydrogen bonds present, the hydroxyl and aromatic carbons remain the same as in the solid form approximation. The amide and methyl

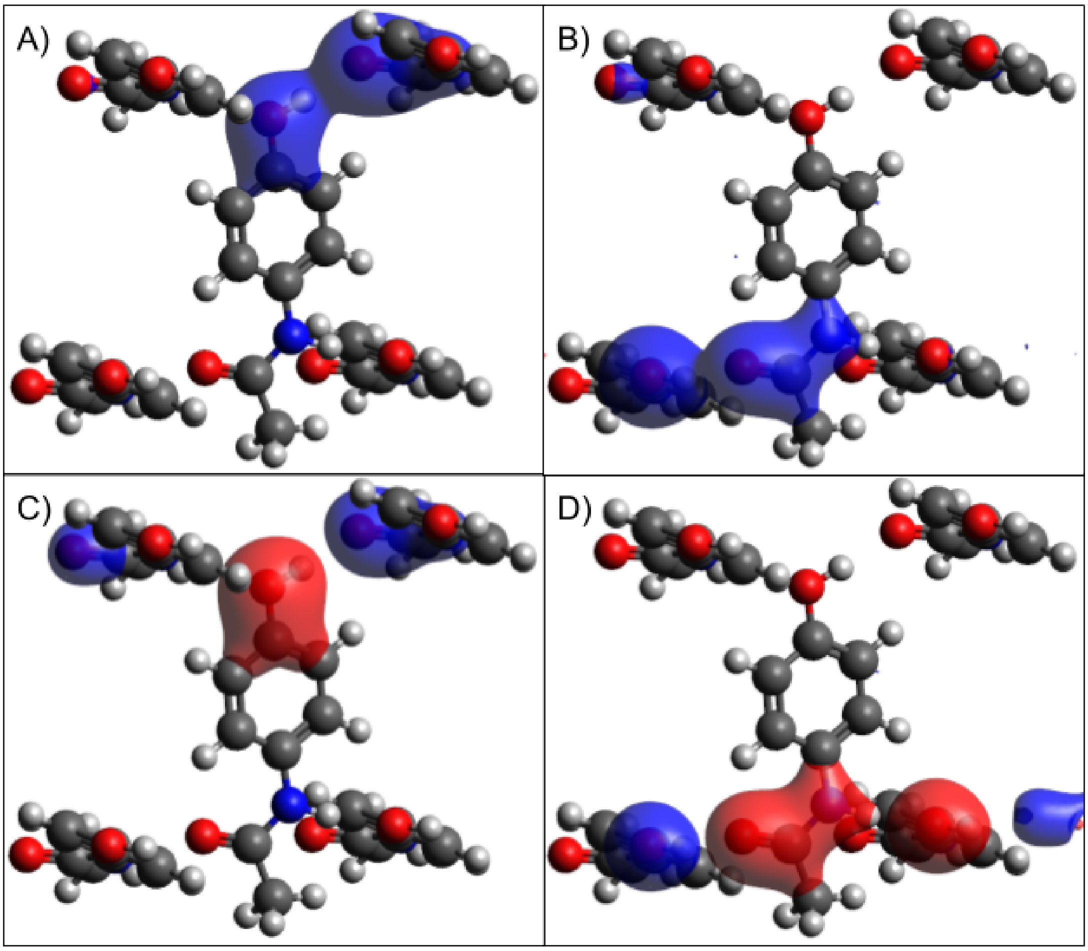

Figure 2.16: Low HOMOs in a solid form approximation of paracetamol

Where A is the lowest energy HOMO orbital in the solid form approximation that includes the central molecule. D is the fourth lowest energy HOMO orbital in the solid form approximation. B and C are between the two.

carbons 1s binding energies are blueshifted by 0.1 eV and 0.2 eV, respectively. The carbonyl is redshifted by 0.1 eV. The implication of these differences, is that when all hydrogen bond contacts are made with the molecule of interest, the electron density throughout the *para*-position of the molecule is somewhat decreased, relative to the rest of the molecule. This is further reinforced by the fact that the single molecule calculation determined the electron density in the *para*-position of the molecule to be significantly greater. Once the van der Waals interactions are also in place, these appear to stabilise the electron density throughout the molecule of interest, in a more uniform manner. This is again further reinforced with reference to the "No H-bonds" dimer calculations. In these calculations, "No H-bonds 2" (fig 2.11) the carbon 1s binding energies from both molecules were identical to the single molecule calculation. Whereas in "No H-bonds 1" (fig 2.10), the molecules were significantly closer together. Their calculated carbon 1s binding energies showed the effect of the van der Waals dispersion in bringing the methyl carbon 1s binding energy more inline with that of the aromatic carbons. Figure 2.17 shows the information in table 2.5 to visually represent the effects of hydrogen bonding interactions on paracetamol molecules.

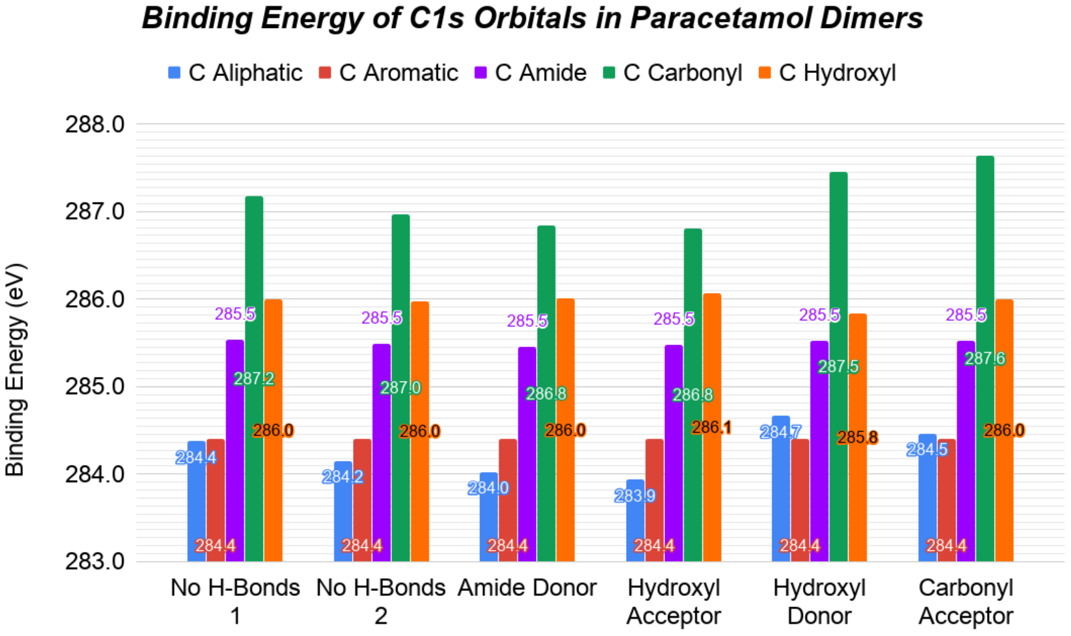

Figure 2.17: Binding energy of C1s orbitals in paracetamol dimers

2.3.4 Conclusions

Linear Combination of Atomic Orbital (LCAO, or *atom centred*) based density functional theory codes utilising solid form approximation inputs provide a good compromise between expensive (in terms of compute resource and economic cost), all-electron plane wave codes, and expensive (in terms of economic cost) periodic LCAO codes. It must however be noted, that this is unlikely to remain the case when systems of interest place a high-weight on Coulombic interactions, for example, charged systems, or transition metal complexes. In these cases, the number of atoms needed to generate a meaningful solid form approximation would make the calculations far too costly for all but the most powerful HPC systems. Though given recent advances in both CPU and GPU manufacture, it may be possible to extend this approach to larger systems, by making use of a shared memory architecture and heavy use of GPU based parallelism. This may be explored in future works.

The use of an RijCosX approximation to speed up the calculations came with little drawback, and the addition of dispersion correction to the calculations served little benefit. However, this may simply have been a quirk of the system under investigation. These additions to DFT calculations should always be tested and confirmed to be appropriate for the system being studied.

While not in perfect agreement with the experimentally determined binding energies of the carbon 1s environments, all environments but the methyl carbon were within ±0.3 eV, if calibrated to the carbonyl at 287.7 eV. The methyl carbon was substantially different though this will be discussed later in this chapter. The calculations also showed that changes in the hydrogen bonding environment of paracetamol, has a large effect on the carbon 1s binding energies particularly the carbonyl and methyl carbons.

2.4 General Discussion

In order to directly compare the DFT outputs to the experimental results from the UHV-XPS, all calculated carbon 1s binding energies were calibrated to the carbonyl carbon at 287.7 eV. As this was the calibration point applied to the carbonyl carbon shoulder in the XPS spectra. Tables 2.8, and 2.9, are the same as tables 2.5, and 2.7. Here they are shown with the results calibrated to the carbonyl carbon at 287.7 eV.

Table 2.8: C1s orbital energies in paracetamol dimers as calculated by DFT and measured experimentally

(Calibrated to 287.7 eV as the carbonyl C)

Atom	**No H-Bonds 1**	**No H-Bonds 2**	**Amide Donor**	**O-H Acceptor**	**O-H Donor**	**C=O Acceptor**
C Hydroxyl	286.5	286.7	285.9	286.0	285.8	286.1
C Aromatic	284.9	285.1	284.3	284.3	284.7	284.5
C Amide	286.0	286.2	285.4	285.4	285.8	285.6
C Carbonyl	287.7	287.7	287.7	287.7	287.7	287.7
C Methyl	284.9	284.9	283.9	283.8	285.0	284.6

Table 2.9: C1s orbital energies in a single paracetamol molecule as calculated by DFT

(Calibrated to 287.7 eV as the carbonyl C)

Atom	**Single Molecule**	**Solid Form Approximation**	**UHV-XPS Experimental**
C Hydroxyl	286.7	286.0	285.8
C Aromatic	285.1	284.4	284.6
C Amide	286.2	285.4	285.1
C Carbonyl	287.7	287.7	287.7
C Methyl	284.9	284.4	283.6

These results show that the use of DFT in calculating solid form 1s binding energies is appropriate, and gives results within an acceptable level of error when compared to the experimental result (±0.3 eV). While the methyl carbon calculation for the solid form approximation was incorrect, with a calculation over 1 eV off from the experimental results. However, with regard to table 2.8, when all hydrogen bonds are unsatisfied the binding energy, particularly that of the methyl carbon can shift by over 1 eV. Furthermore, one can consider the total electron density of the molecule. In the case of the solid form approximation, calculation of an electron density plot is prohibitively expensive in terms of computational cost. Therefore, the Mulliken charges calculated as part of the DFT calculations was used as a proxy for electron density. In this case the lower the Mulliken charge of the atom, the greater the electron density. Figure 2.18 shows a bar graph plotting the Mulliken charges of the paracetamol molecule. It can be seen that in all cases, but the fully interaction satisfied solid form approximation, the electron density surrounding the methyl carbon is considerably higher than around any of the other atoms in the paracetamol molecule. It is therefore likely that the initially surprising XPS results, in which an methyl peak was observed at a lower binding energy than the aromatic peaks, is not as surprising as first thought. Rather, it may be a surface effect, in which molecules at the interface between the solid paracetamol, and the surrounding vacuum do not have completely satisfied hydrogen bond environments. This in turn causes the electron density around the methyl carbon to be perturbed, relative to the bulk paracetamol in the solid form.

Previous work [112] has shown some slightly different results with respect to the low binding energy methyl peak discovered in this analysis. Bouhmaida et al. calculated that the charge on the aromatic carbon atoms is either slightly lower than that of the methyl carbon, or that it is substantially lower. This is indeed backed up by the results presented in this chapter, if one is solely concerned with the bulk properties of paracetamol in the solid form, where table 2.9 shows that the expected binding energies for the solid form paracetamol is in agreement with those described by Bouhmaida et al. However, it must be pointed out that in their analysis, no consideration was made as to the nature of the terminating groups of the paracetamol surface. This is not to say they are incorrect, merely that this investigation is probing different phenomena.

Suggestion has been made within the S.L.M.S research group that the low binding energy peak may be related to early stage adventitious carbon deposition. The findings from this investigation dispute this however. Figure 2.4 and table 2.1 clearly show that there is no excess carbon present in the system beyond that sourced from the paracetamol molecule. Furthermore, figures 2.19 and 2.20 show no evidence of carbon contamination at all, either before (figure 2.19) or after (figure 2.20) the paracetamol film measurements were taken.

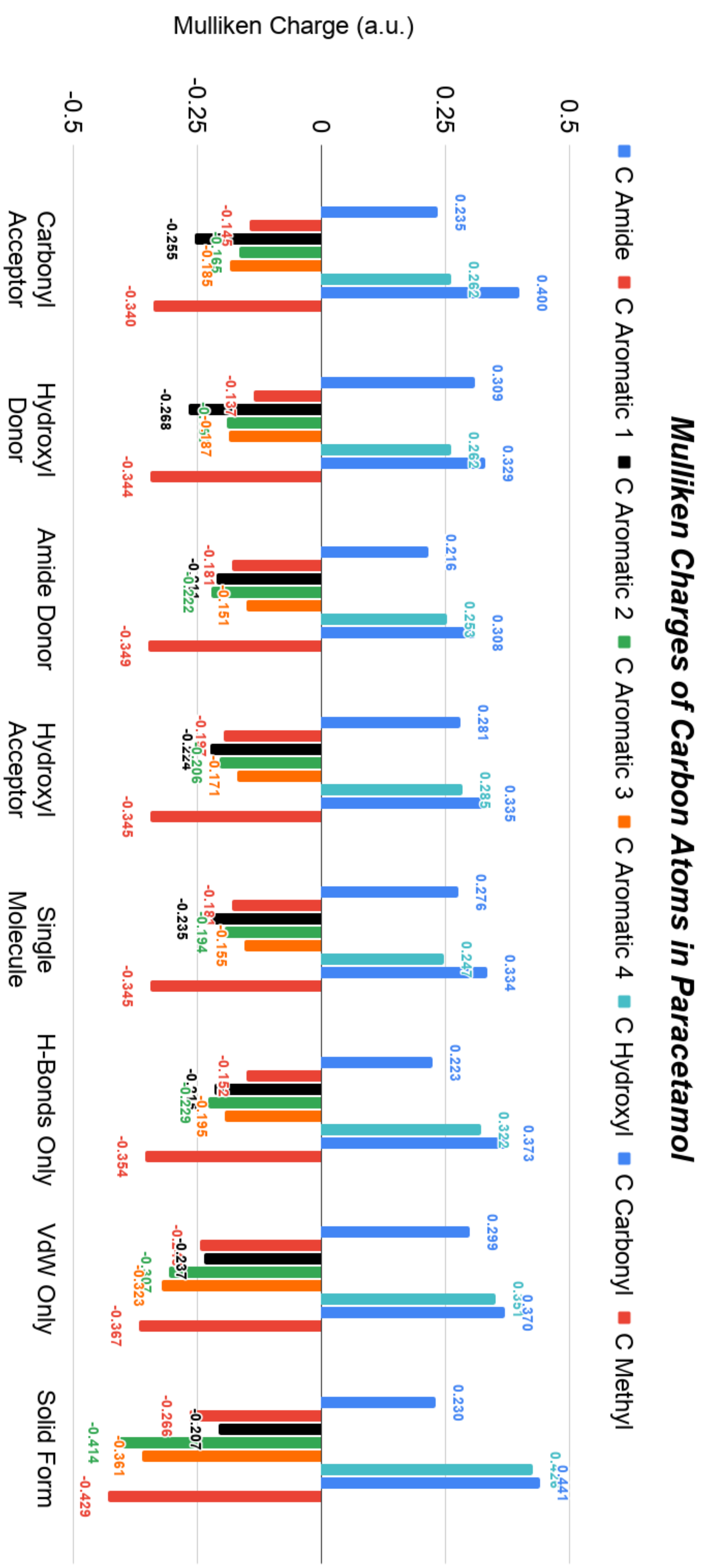

Figure 2.18: Graph showing the Mulliken charges of carbon atoms in paracetamol

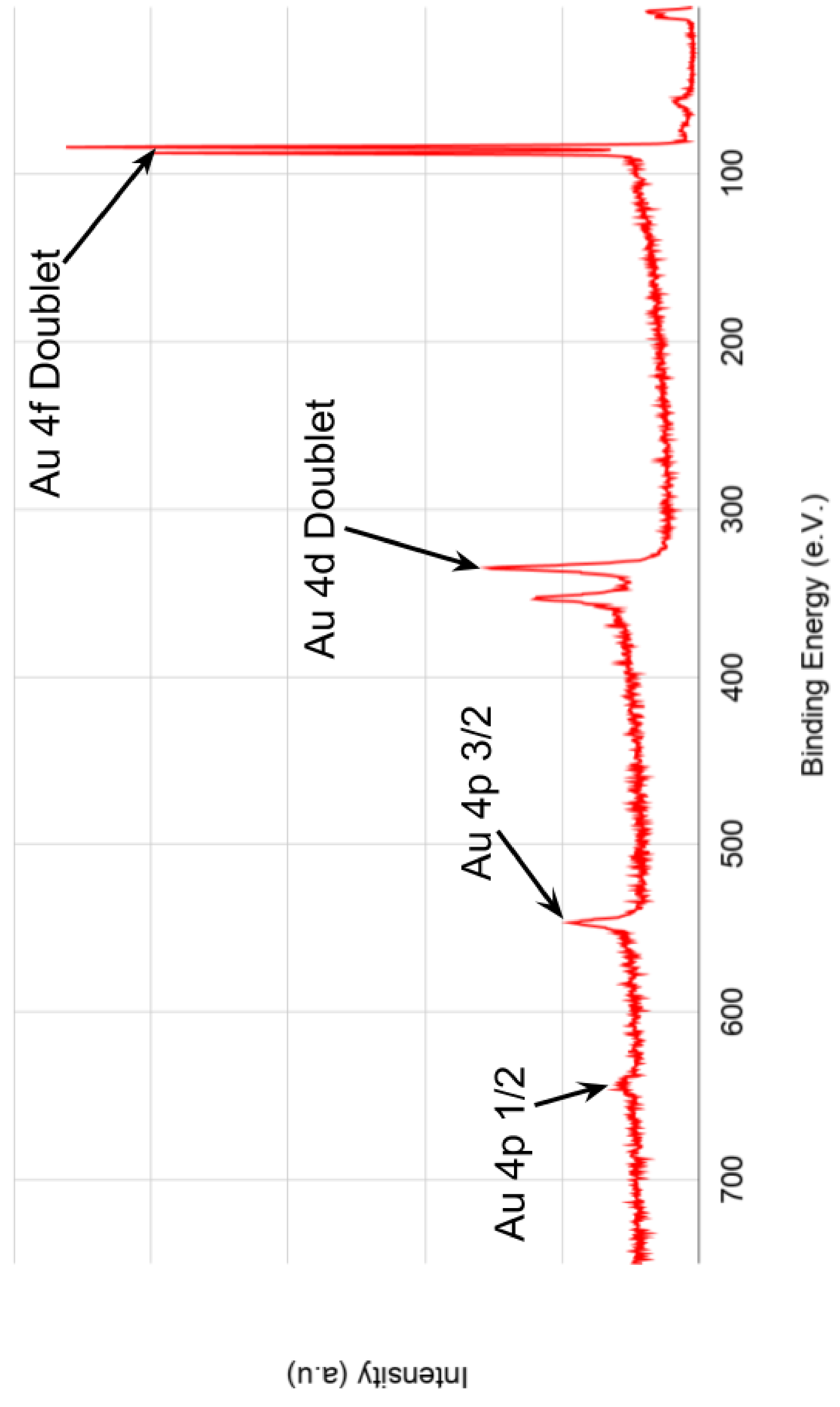

Figure 2.19: Survey scan of Au(111) post Ar sputtering, before paracetamol deposition

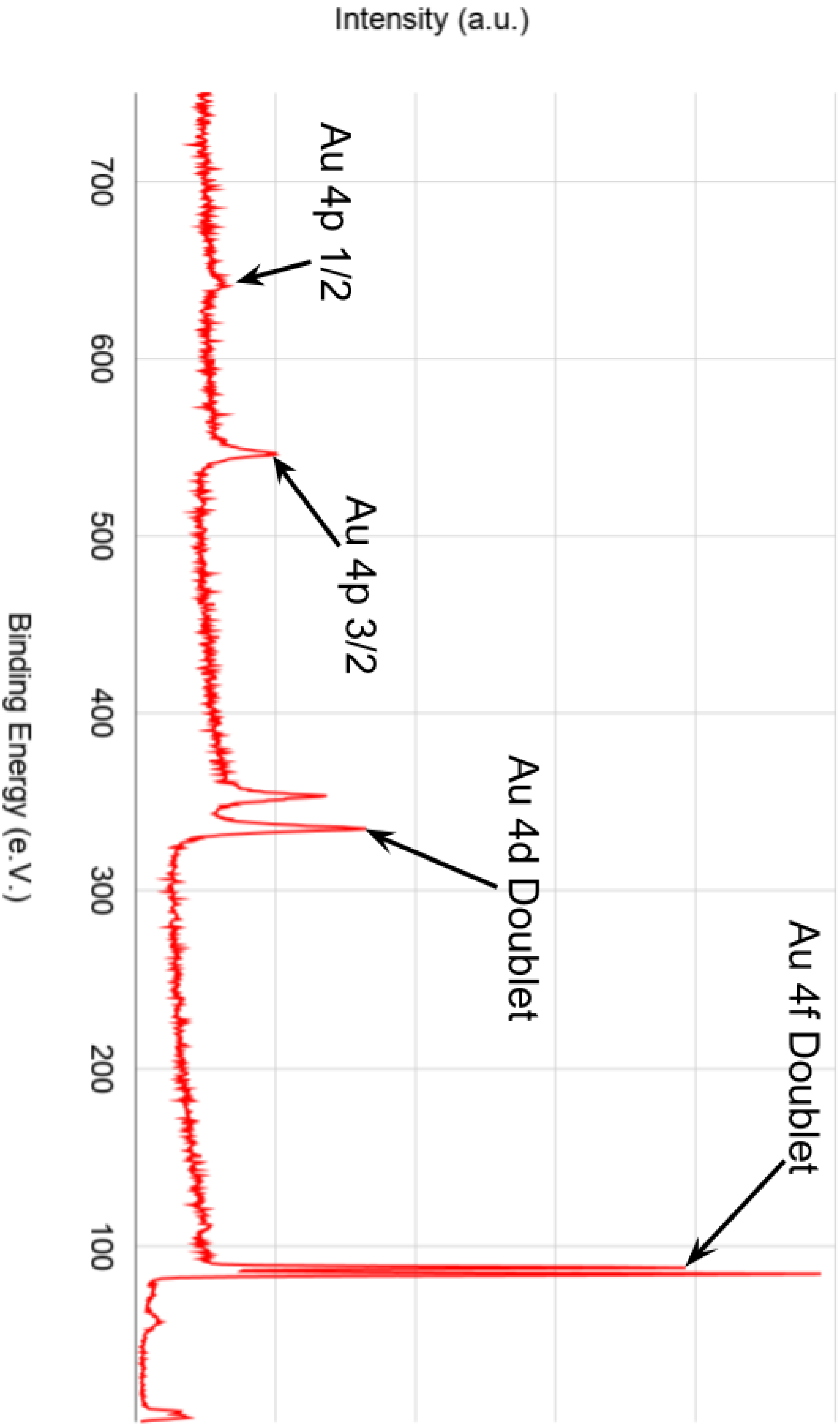

Figure 2.20: Survey scan of Au(111) post Ar sputtering, after paracetamol deposition

2.5 Conclusions

Vacuum deposition of paracetamol from the gas phase is a good method for preparing ultra clean paracetamol surfaces, assuming of course, that it is done under UHV conditions. For analysis by surface sensitive techniques, such as XPS or ToF-SIMS, it could be argued that it is the *only* method for preparing these surfaces, given the incompatibility of most organic crystal systems with high-energy ion beams, or temperatures sufficient to remove contamination from their surfaces. With appropriate input geometries, taken from a good crystal structure, calculation of binding energies is well suited to density functional theory calculations. For researchers of means, this could possibly be extended into the use of periodic LCAO codes, though more research would be needed before drawing conclusions. Some initial attempts were made at these calculations utilising geometry optimisation, and other electronic structure calculation methods. Unfortunately, all were poor choices for this application, predominantly due to the calculated binding energies having little in common with experimental results. In the case of coupled-cluster single-double with perturbative triples (CCSD(T)), the issue was more a case of the computer resources required to calculate such large systems. While DFT and UHV-XPS with vacuum deposited paracetamol worked well together in establishing baseline properties of paracetamol, unfortunately this cannot be extended to real world organic systems of interest. Few organic crystalline products are made for mass market consumption by vacuum deposition. Therefore not only are methods for establishing rigorous analysis of organic crystalline systems needed, but also, methods for preparing "real world" samples are required.

Chapter 3

Surfactant Deposition on to Paracetamol Powders

3.1 Introduction

3.1.1 Motivation

With a baseline established for analysing paracetamol by X-ray photoelectron spectroscopy in the previous chapter, the next stage of this investigation was to determine whether or not adsorbed surfactant could be detected by XPS. In order to achieve this, a new instrument, the *EnviroESCA* (SPECS GmbH, Berlin, Germany) was utilised. Having information that confirms that surfactant molecules will adsorb to paracetamol crystal surfaces is critical to undertaking experiments to quantify the level of adsorbed surfactant. These experiments were also utilised as a method to test the *EnviroESCA* instrument. A relatively recent addition to the market, the EnviroESCA is a completely self-contained NAP-XPS instrument. Sample loading in the EnviroESCA is achieved via a computer controlled module, which contains it's own in-build plasma cleaning and vacuum sealing/pump down equipment. There is then large valve separating sample loading from analysis chambers. Having never been used in an academic research setting, there was a desire to test the capabilities of the instrument, and ensure it was capable of producing results that were in line with those expected from existing laboratory XPS systems. A technologically important surfactant is the non-ionic molecule nonylphenyl ethoxylate 9, which is marketed under the trade name *Tergitol NP-9*. Its molecular structure consists of three principal components, a nonane chain connected to the 4 position of a benzene ring, and a nine-membered ethoxylate chain terminated by a hydroxyl group. In this structure the surfactant tail group is represented by the nonane chain and the ring structure. The head group is represented by the ethoxylate chain. Figure 3.1 shows a representation of Tergitol NP-9 as a ball and stick representation of the molecule. The nonane chain is shown in the 4 position of the aromatic ring, and the nine membered ethoxylate chain, terminated by a hydroxyl group is in the 1 position of the ring. Historically, Tergitol NP-9 has been used to stabilise aqueous suspensions of organic crystals at high concentrations. For Tergitol NP-9 at high concentrations, the main product engineering challenges are the aggregation and caking of the crystal component of their formulations. It should be stressed that paracetamol and Tergitol NP-9 represent a model system, to establish the principle for use with proprietary molecules, and to aid in design of new formulations.

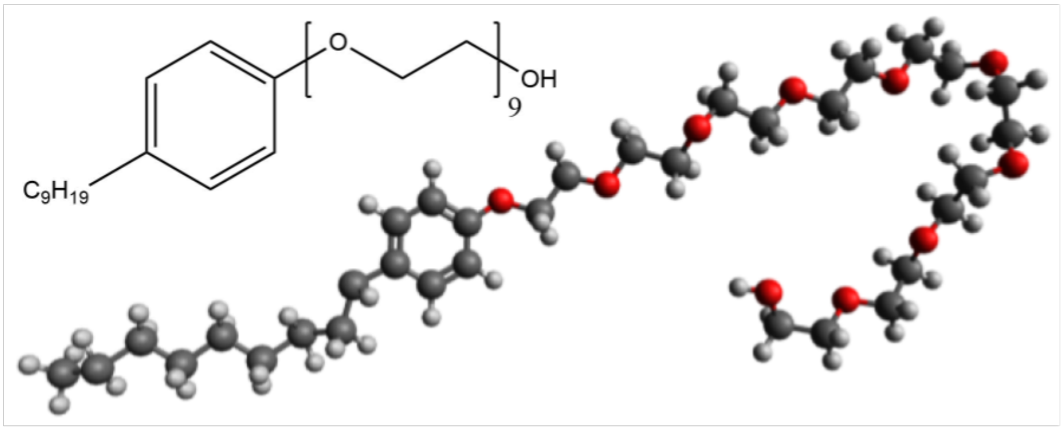

Figure 3.1: Ball and stick diagram of Tergitol NP-9

3.1.2 Aims

- To obtain XPS spectra of paracetamol under NAP-XPS conditions. To include O1s, N1s, C1s, and wide survey scans.
- To determine appropriate levels of surfactant for optimal adsorption to paracetamol.
- To determine an appropriate method for adsorbing surfactant to paracetamol surfaces.

3.2 Materials and Methods

Eight samples were made up for analysis. The first being neat Tergitol NP-9 liquid (>99.9%, Sigma-Aldrich, UK). The rest were composed of varying mixtures of paracetamol powder (>99.9%, BioXtra, Sigma-Aldrich, UK), and Tergitol NP-9. These are shown in table 3.1.

Table 3.1: Paracetamol samples for Tergitol deposition

Sample Number	**Sample Description**
1	Paracetamol powder as received (Unwashed)
2	Paracetamol powder washed in ultra-pure water
3	Paracetamol powder washed in ultra-pure water and exposed to 0.1% w/w Tergitol NP-9
4	Paracetamol powder washed in ultra-pure water and exposed to 0.2% w/w Tergitol NP-9
5	Paracetamol powder washed in ultra-pure water and exposed to 0.4% w/w Tergitol NP-9
6	Paracetamol powder washed in ultra-pure water and exposed to 0.8% w/w Tergitol NP-9
7	Paracetamol powder washed in ultra-pure water and exposed to 1.6% w/w Tergitol NP-9

The neat Tergitol NP-9 sample was prepared by filling a standard differential scanning calorimetry pan with Tergitol NP-9, taken directly from the bottle with a 1 ml sterile plastic syringe. The unwashed paracetamol powder was pressed onto an SEM stub, covered with double-sided carbon tape. The remaining samples were each prepared by first dissolving an excess of paracetamol in 100 ml de-ionised H_2O. A clean magnetic stirrer was added to the mixture before being covered with parafilm and agitated at 500 rpm. This was left overnight to ensure complete dissolution of the paracetamol, to saturation. The resultant solution was then filtered through a glass fibre filter and the supernatant collected. The supernatant being de-ionised H_2O saturated with dissolved paracetamol. An abundance of paracetamol powder ($\sim$25 g) for use in these solutions was initially measured out into a glass fibre filter and washed with de-ionised H_2O chilled to 4°C. This chilled water wash was repeated twice. The washing was achieved by means of büchner filtration using a small vacuum pump. For each of the samples, solutions of paracetamol and Tergitol were weighed out according to table 3.2.

An additional sample was made up using 100 g of water and 0 g Tergitol NP-9. Each of

Table 3.2: Preparation of paracetamol powder samples

Sample	**Mass of supersaturated Paracetamol Solution (g)**	**Mass of Tergitol (g)**
3	99.9	0.1
4	99.8	0.2
5	99.6	0.4
6	99.2	0.8
7	98.4	1.6

these solutions had ∼1 g of washed paracetamol added to it, before being covered in parafilm and stirred at 500 rpm for one hour. Samples were then filtered through a glass fibre filter, the powder collected from the filter and applied to an analysis stub coated with a double sided carbon tape before being dried by vacuum dessication. XPS spectra from each of the samples was then collected using the *EnviroESCA* NAP-XPS instrument, which was set to a pressure of ∼8 mbar Ar gas. Three survey scans were acquired of each sample over a binding energy range from 600 eV - -4 eV, with a step size of 1 eV and a dwell time per step of 0.1 s. Detailed spectra for each sample were then acquired at the N1s, C1s, and O1s peaks, with the binding energy ranges for each peak determined from the survey spectra. Table 3.3 shows the settings used for acquisition of the detailed spectra. Data Analysis was undertaken utilising the same method as described in Chapter 2.2.1, and concentrates on the C1s spectra from each sample.

Table 3.3: Detailed scan acquisition settings

Element	**Number of Scans Summed**	**Start Binding Energy (eV)**	**End Binding Energy (eV)**	**Pass Energy (eV)**	**Binding Energy Increment (eV)**	**Increment Dwell Time (s)**
C1s	6	291	280	20	0.2	1
O1s	6	543	529	20	0.2	1
N1s	6	408	397	20	0.2	1

3.3 Results

Neat Tergitol NP-9 Surfactant

Results from the neat Tergitol NP-9 C1s spectrum showed two distinct peaks, separated by 1.6 eV, as shown in Figure 3.2. One is assigned to a convolution of methyl and aromatic carbon at 285.0 eV, and the other is assigned to ethoxylate carbon at 286.6 eV. This is in very good agreement with work previously carried out in the SLMS research group, with the C-C-O group identified at binding energies of 286.4-286.5 eV and that of the C-C at 285.0 eV [94]. The ethoxylate peak was observed to have 30% greater intensity than that of the C-C peak. This is outside of the expected levels for pure Tergitol NP-9 (35%) but within the same level of error as seen in previous works [94]. It is unlikely that the sample supplied is 100% pure. Figure 3.2 shows two peaks, representing two carbon functional groups. The orange labelled peak represents the ethoxylate carbons (C-C-O), and the blue labelled peak represents the both the aromatic and aliphatic carbon (C-C).

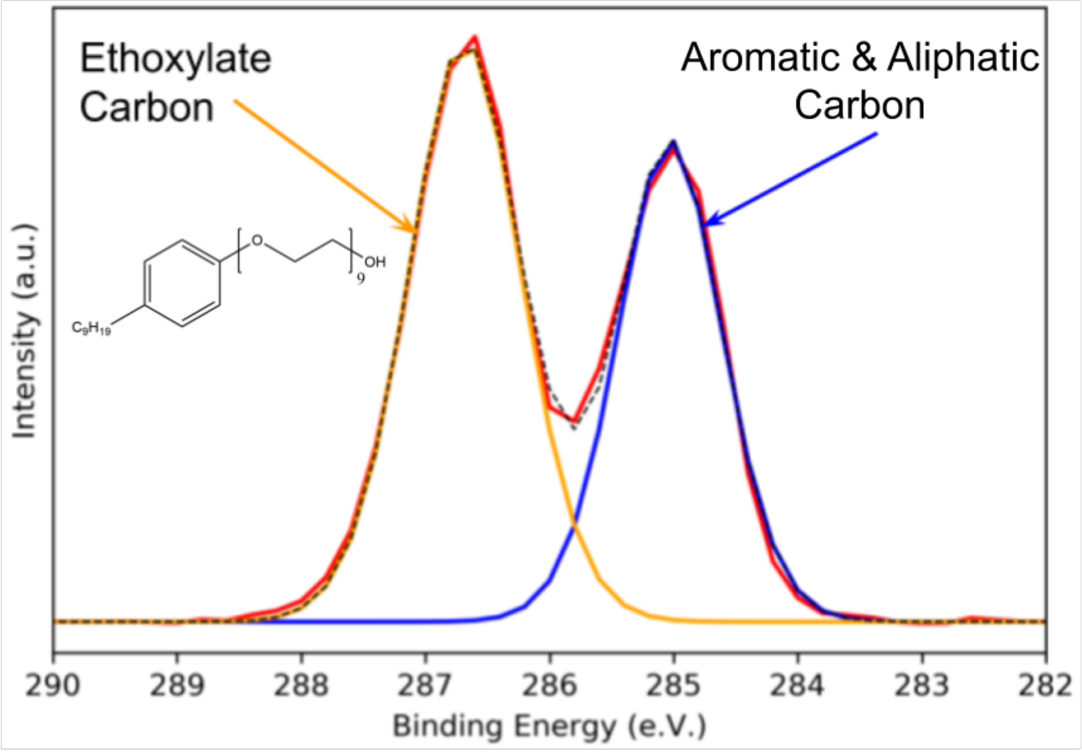

Figure 3.2: C1s region of XPS spectrum of Tergitol NP-9

The O1s spectrum showed two peaks, one far in excess of the other. The peak of greater intensity was assigned to the ethoxylate oxygen (C-C-O), and the lesser to the terminating hydroxyl group (O-H). Figure 3.3 is a detailed XPS spectrum of the Tergitol NP-9 O1s peak. The spectrum contains two peaks, representing two oxygen environments. The orange labelled peak represents the ethoxylate oxygen (C-C-O), and the blue labelled peak represents the hydroxyl oxygen (O-H).

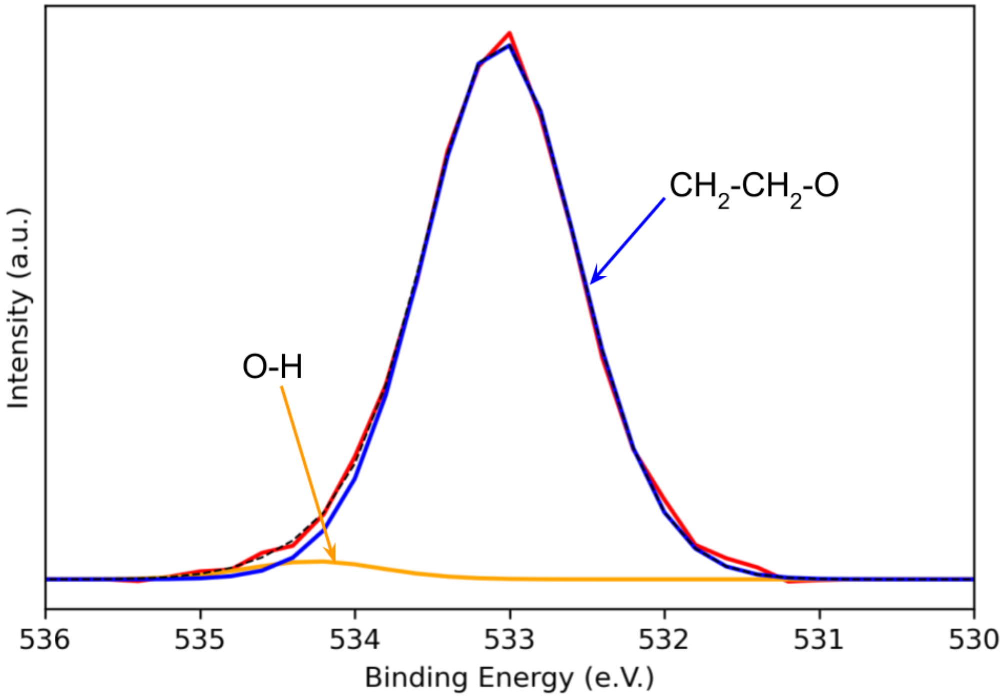

Figure 3.3: O1s region of XPS spectrum of Tergitol NP-9
Where the orange peak represents hydroxyl oxygen and the blue peak represents ethoxylate oxygen.

As Received Powder & Washed Powder

The C1s spectrum contained ∼29% more carbon than that of the spectrum of as received paracetamol powder. The main peak in the C1s spectrum of the as received paracetamol was also considerably broader than that of the washed powder. Figure 3.4 is a detailed XPS spectrum of paracetamol 'as received' (shown in blue), and paracetamol powder after washing with de-ionised H_20 (shown in red).

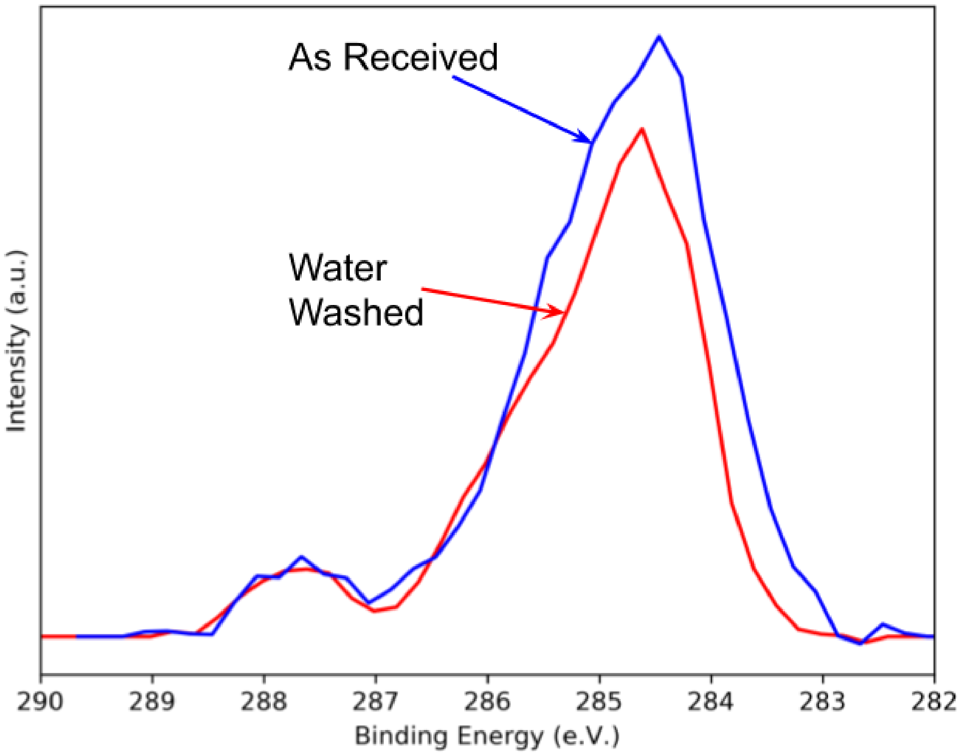

Figure 3.4: C1s XPS spectra of 'as received' paracetamol powder & paracetamol powder post water wash

Attempts to fit the raw powder spectrum were unsuccessful, as no sensible fit could be obtained. This was expected given both the unknown levels and nature of possible contaminants in the powder. In the case of the washed powder, the hydroxyl, carbonyl, and amide carbons were identified, as was the aromatic carbon peak at four times the intensity of the others. The methyl peak at the low binding energy side of the main peak could not be fitted. There was an additional peak at ∼285 eV, assigned to adventitious carbon contamination. Figure 3.5 shows the C1s spectrum of de-ionised H_2O washed paracetamol powder, with Gaussian-Lorentzian (L=30%) functions fitted. The identified features were the carbonyl (C=O) carbon (orange), the hydroxyl (C-OH) carbon (cyan), the amide (C-N) carbon (magenta), and the aromatic carbons (Green). There was also an aliphatic adventitious (C-C) carbon identified (blue).

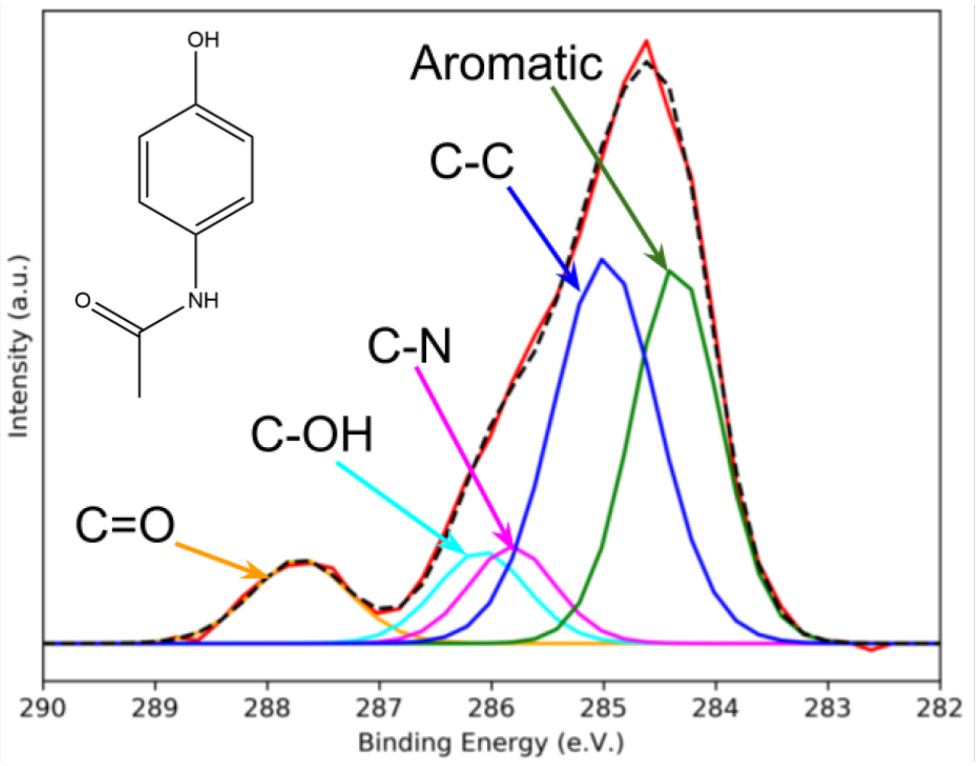

Figure 3.5: C1s XPS spectra of water washed paracetamol powder

Washed Paracetamol Powder Exposed to Varying Concentrations of Tergitol NP-9

Shown first is the comparison of all concentrations used, including both the 'as received' sample, and the water washed sample. There was little in the way of an observable trend in the spectra, with respect to the level of surfactant. This was in some way expected, given the combination of the method of exposure, and the lack of knowledge about how the surfactant behaves in an aqueous environment, especially as a function of increasing concentration.

What was observable was at 0.2% w/w surfactant, the maximum intensity of the main peak was similar to that of the 'as received' sample, though was significantly less broad. At 1.6% w/w, the maximum intensity of the main peak was ~25% lower than that observed for the 'as received' sample, and ~10% lower than that of the water washed sample. Figure 3.6 shows the C1s spectra of paracetamol powders exposed to varying levels of surfactant. The spectrum shown in brown, is that of the water washed sample, as seen in figure 3.4. The remaining spectra are powders that have been exposed to surfactant at the following concentrations; 0.1% w/w (blue), 0.2% w/w (orange), 0.4% w/w (green), 0.8% w/w (red), 1.6% w/w (lilac).

The sample of paracetamol exposed to 1.6% w/w Tergitol NP-9 showed the greatest reduction in surface contamination, relative to the other samples, and the lowest signal from Tergitol NP-9 carbon atoms. When the spectrum was fitted, paracetamol signals were fitted in the expected concentrations, with the carbonyl, hydroxyl, and amide carbons

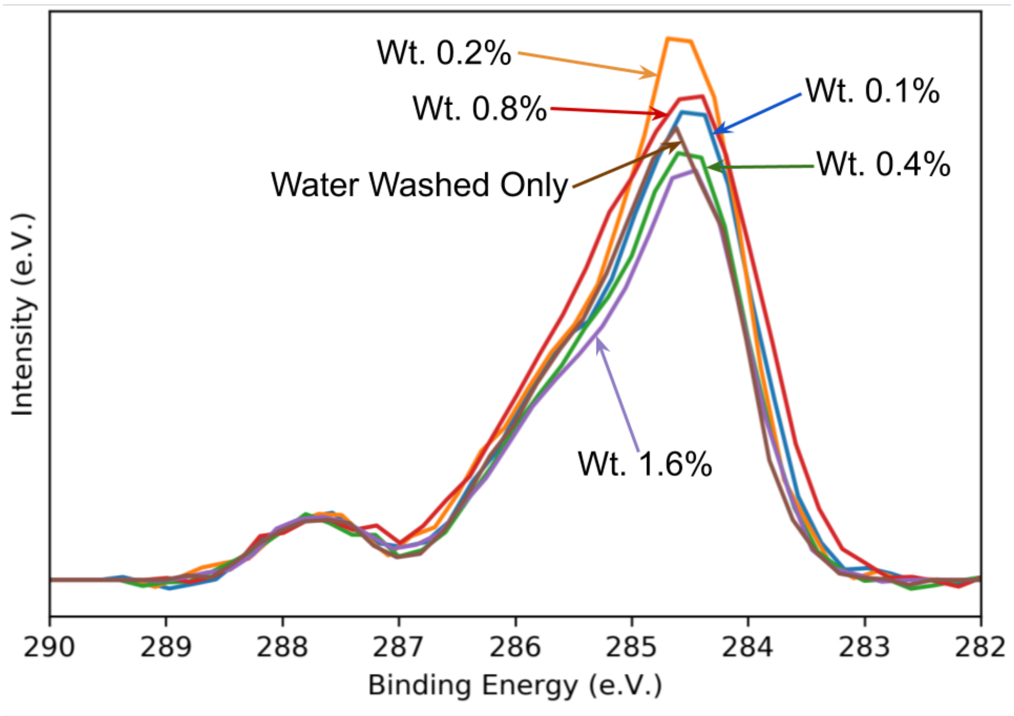

Figure 3.6: XPS C1s spectra comparison of paracetamol powders exposed to varying levels of Tergitol NP-9

being of equal intensity, and the aromatic signal being four times greater.

In this spectrum, like the water washed sample, no low binding energy methyl carbon signal could be fitted. There were however, two additional signals fitted. One was assigned to the ethoxylate carbon signal in the Tergitol NP-9, and the other to methyl carbon, which in this instance is related to methyl carbon in the paracetamol, Tergitol, and adventitious carbon. Given the fact that this was fitted at a 4:3 ratio for aromatic:methyl carbon, it is unlikely that there is more than trace adventitious carbon signal being detected. Figure 3.7 shows the C1s spectrum of paracetamol powder exposed to 1.6% (w/w) Tergitol NP-9 surfactant. The paracetamol signals can be seen in the carbonyl (C=O, orange), hydroxyl (C-OH, cyan), amide (C-N, pink), and aromatic (green) peaks. The ethoxylate (C-C-O) carbon is shown in yellow. The methyl (C-C) carbon signal is shown in blue, and represents methyl carbon from paracetamol, Tergitol, and adventitious carbon.

The spectrum of paracetamol powder that had been exposed to 0.8% w/w Tergitol showed a considerably greater concentration of ethoxylate carbon, whereas the spectra of paracetamol exposed to 0.1% w/w, 0.2% w/w, and 0.4% w/w Tergitol all showed much greater concentrations of methyl carbon. A comparison of the spectra obtained for all four of these concentrations is shown in figure 3.8. The top left plot shows the C1s spectrum of paracetamol powder exposed to 0.1% w/w Tergitol NP-9 surfactant. The top right shows the same with 0.2% w/w Tergitol NP-9. The bottom left and right show

Table 3.4: Intensities of peaks fitted to the spectra of paracetamol powder exposed to different concentrations of Tergitol
BE positions (eV) are indicated in parentheses

Tergitol Concentration (% w/w)	**C=O**	**C-OH**	**C-N**	**C Aromatic**	**C-C**	**C-C-O**
0	1 (287.7)	1 (286.1)	1 (285.8)	4 (284.4)	5 (285.0)	- (-)
0.1	1 (287.7)	1 (286.3)	1 (285.6)	4 (284.3)	5 (284.8)	1 (285.6)
0.2	1 (287.7)	1 (286.3)	1 (285.7)	4 (284.3)	5 (284.7)	2 (285.5)
0.4	1 (287.7)	1 (286.1)	1 (285.8)	4 (284.3)	4 (284.7)	2 (285.4)
0.8	1 (287.7)	1 (286.3)	1 (285.9)	4 (284.2)	5 (284.6)	3 (285.3)
1.6	1 (287.7)	1 (286.2)	1 (285.5)	4 (284.3)	3 (284.7)	1 (285.6)

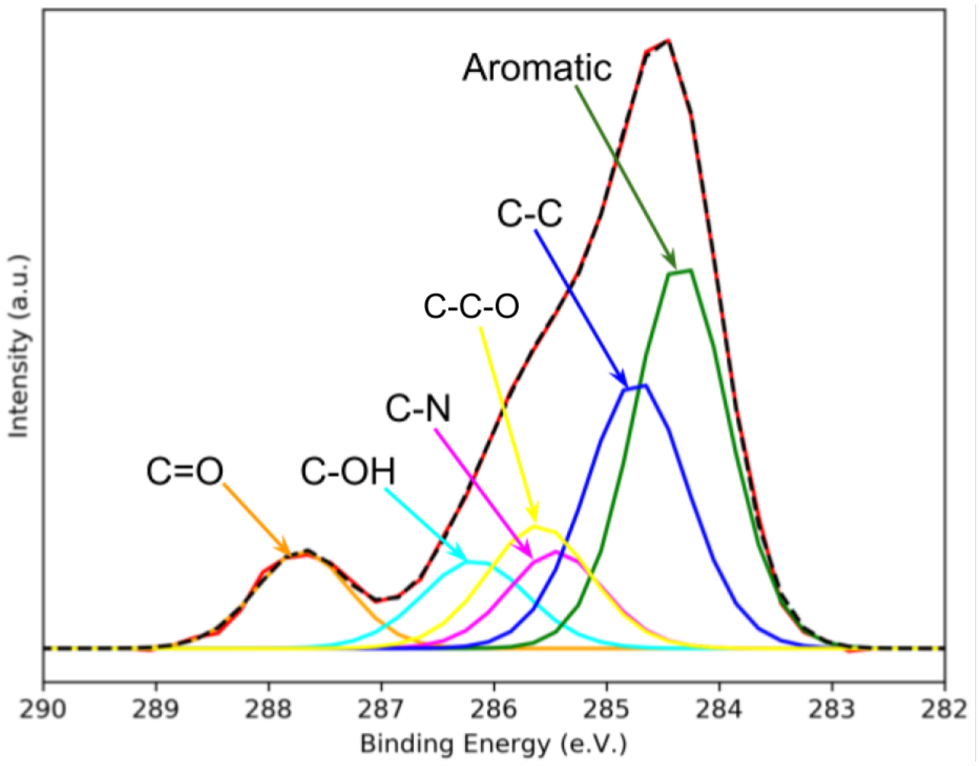

Figure 3.7: Fitted XPS C1s spectra of paracetamol powder exposed to wt.1.6% Tergitol NP-9

spectra obtained for paracetamol samples exposed to Tergitol concentrations of 0.4% w/w, and 0.8% w/w, respectively. The paracetamol signals can be seen in the carbonyl (C=O, orange), hydroxyl (C-OH, cyan), amide (C-N, pink), and aromatic (green) peaks. The ethoxylate (C-C-O) carbon is shown in yellow. The methyl (C-C) carbon signal is shown in blue, and represents methyl carbon from paracetamol, Tergitol, and adventitious carbon.

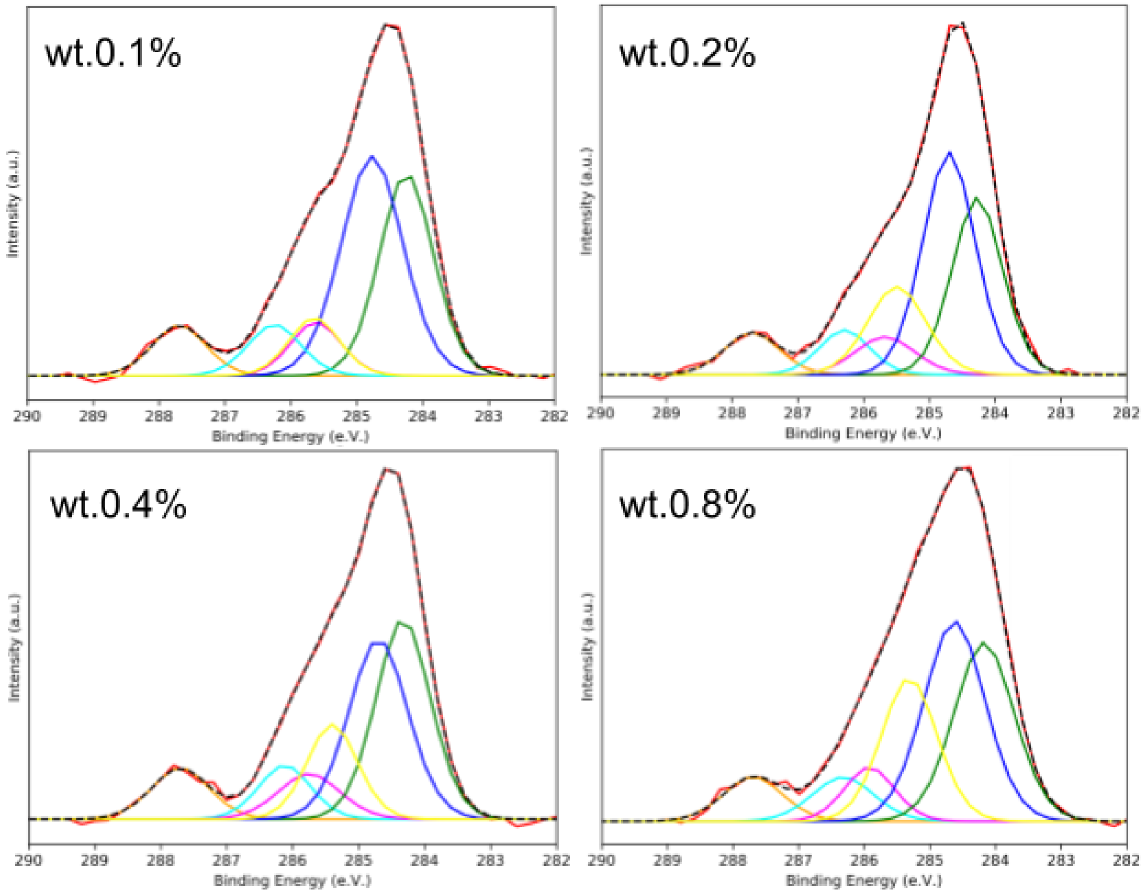

Figure 3.8: Fitted XPS C1s spectra of paracetamol powder exposed to 0.1%, 0.2%, 0.4%, and 0.8% w/w of Tergitol NP-9

Where the green peak represents the aromatic signal, the blue peak represents C-C signal, the yellow peak represents the ethoxylate carbon signal, the magenta peak represents the amide carbon signal, the cyan peak represents the hydroxyl carbon signal, and the orange peak represents the carbonyl carbon signal.

3.4 Discussion

The immediate first noticeable difference between all of the analysed spectra is the disappearance of the low binding energy methyl peak seen previously in figure 2.5 in the previous chapter. This peak was expected at the low binding energy side of the curve at 283.6 eV (table 2.2). It was not possible to fit such a peak sensibly in any of the spectra. The hypothesis for this is that the water wash is not removing an adequate amount of adventitious carbon from the sample surfaces. There is also the noticeable lack of a trend resulting from exposure to increasing levels of surfactant. Figure 3.9 shows the maximum values of the main peak in the C1s spectra vs. the level of surfactant used in each experiment. The graph shows clearly that no trend is present. While it would have been more desirable to utilise a Langmuir trough to deposit surfactant onto a solid surface, this would have been non-trivial to achieve with powder samples. Furthermore, access to such equipment was not obtainable. This would have allowed for more controlled surfactant deposition on the surface of the crystal. The rationale for this is likely a result of the surfactant's behaviour in an aqueous medium. One explanation for these results is that with a critical micelle concentration (CMC) of 0.006 % w/w [113] it is highly likely that higher order colloidal structures are forming in the medium, given the lowest concentration of Tergitol NP-9 was 0.1 % w/w, and the highest was 1.6 % w/w. Concentrations this far above the CMC will have a major an effect on the surface interactions with the paracetamol powder. An alternative explanation for these results is that at lower concentrations, the surfactant is adsorbing to the surface of the crystal and then at higher concentrations the contamination is being solubilised. The exact nature of these interactions, or indeed the nature of the surfactant's colloidal structure in aqueous medium, is beyond the scope of this investigation.

Table 3.4 show the intensities of all fitted functions to the C1s peaks obtained for paracetamol samples exposed to different concentrations of Tergitol. These intensities are all normalised to the intensity of the C=O shoulder at 287.7 eV. The binding energies of all hydroxyl peaks ranged from 286.1 eV to 286.3 eV putting them all within ±0.3 eV of the solid form binding energy calculated previously by DFT (table 2.9). The C aromatic showed similar results with a fitted range of 284.2 eV to 284.4 eV, again within ±0.3 eV of the DFT calculated solid form binding energy. The amide carbon was more erratic with a range from 285.5 eV to 285.9 eV, where the DFT calculation placed the binding energy at 285.4 eV. This could be a function of changing surface hydrogen bond environments with differing levels of Tergitol NP-9 exposure (see table 2.8). The lack of a separate methyl peak from the paracetamol, and inability to sensibly fit a 5:1 ratio peak at the position of the aromatic carbon, rules out both the solid form calculation, and UHV-XPS results being able to shed any light on the peak position. It is therefore likely, that there is still some contamination present on the surface of the crystal, and that this is affecting the observed methyl carbon peak. For reference, all fitted binding energies are shown in Figure 3.10. One can also consider the ratios of the methyl and ethoxylate peaks fitted

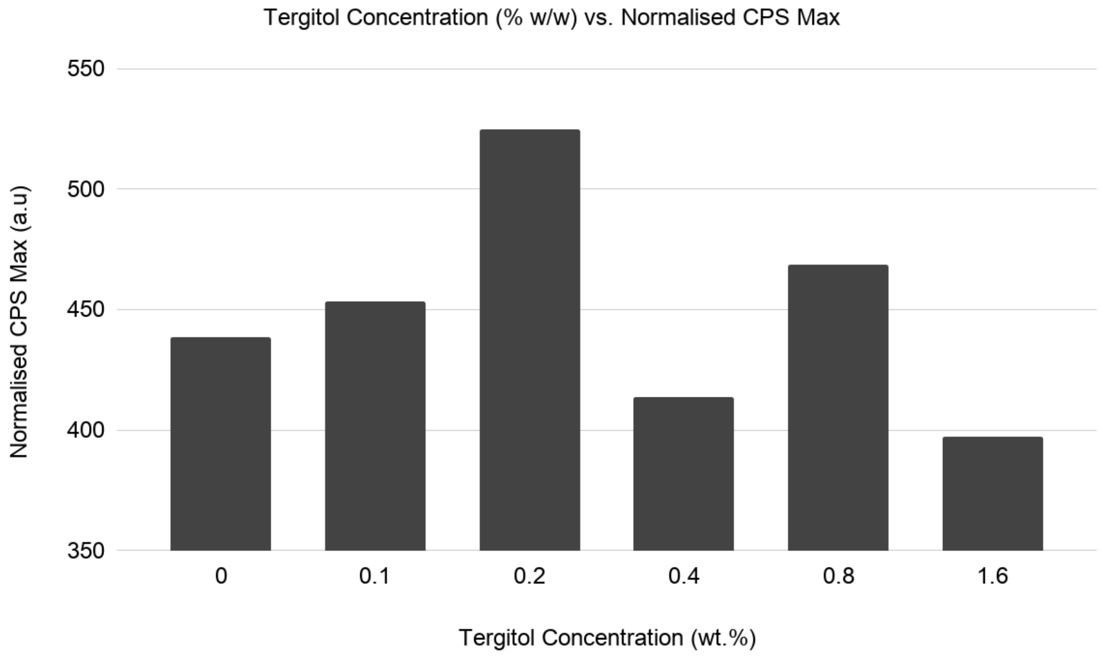

Figure 3.9: Graph showing the normalised counts per second (CPS) of C1s spectra acquired by XPS vs. Tergitol NP-9 concentration

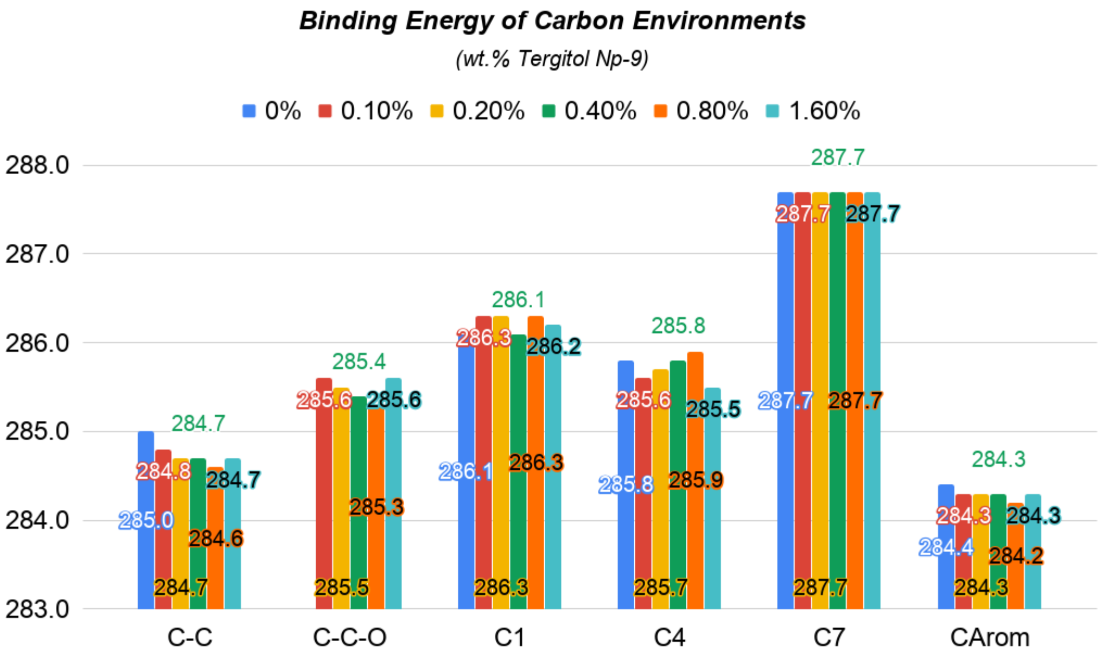

Figure 3.10: Graph showing the C1s binding energies in paracetamol powders exposed to Tergitol NP-9

in the spectra. Figure 3.11 shows the normalised ratios of methyl carbon (C-C) and ethoxylate carbon (C-C-O) to the carbonyl carbon (C=O) in paracetamol. No ethoxylate carbon was detected in the 0% Tergitol spectrum, this was of course, the expected result. This implies that the 5:1 ratio of methyl carbon in the 0% Tergitol NP-9 spectrum is a combination of methyl carbon from paracetamol and adventitious contamination. At 0.1% w/w Tergitol NP-9, there is a peak from the ethoxylate carbon present, but again, there is an abundance of methyl carbon. The spectrum of the 0.2% w/w sample again shows an abundance of methyl carbon, but this time more ethoxylate carbon. Given the lack of change in methyl carbon across the three samples of paracetamol exposed to 0%, 0.1%, and 0.2% w/w Tergitol NP-9, it is likely that the exposure of the powder to the surfactant in aqueous medium is having some effect on the levels of adventitious carbon. The effect being to remove it from the surface of powder.

At higher concentrations, it appears that more contaminating adventitious carbon is being removed, but more surfactant is being deposited on the powder surfaces. For example, at 0.4% w/w Tergitol NP-9, the ratio of methyl carbon drops to 4 while the ratio of ethoxylate carbon is 2. At 0.8% w/w this increases to a ratio of 5 in the methyl carbon, and 3 in the ethoxylate carbon. It is likely at this stage that multiple layers of surfactant are depositing on the surface of the paracetamol powders. At 1.6% w/w both ratios drop to 3 and 1, in the methyl and ethoxylate carbons, respectively. Determining the exact reason for this, is as stated earlier, beyond the scope of this investigation. However, it is likely that at a concentration of Tergitol this high, that higher order colloidal structures are having an effect on the mode of surfactant deposition. At these ratios it would appear that the minimum amount of surfactant deposition has occurred, compared to the other concentrations. Whilst it would be good to ensure that no adventitious contamination could occur between the surfactant deposition and transfer of the sample to the XPS instrument, it is likely to be extremely difficult to achieve this in the real world.

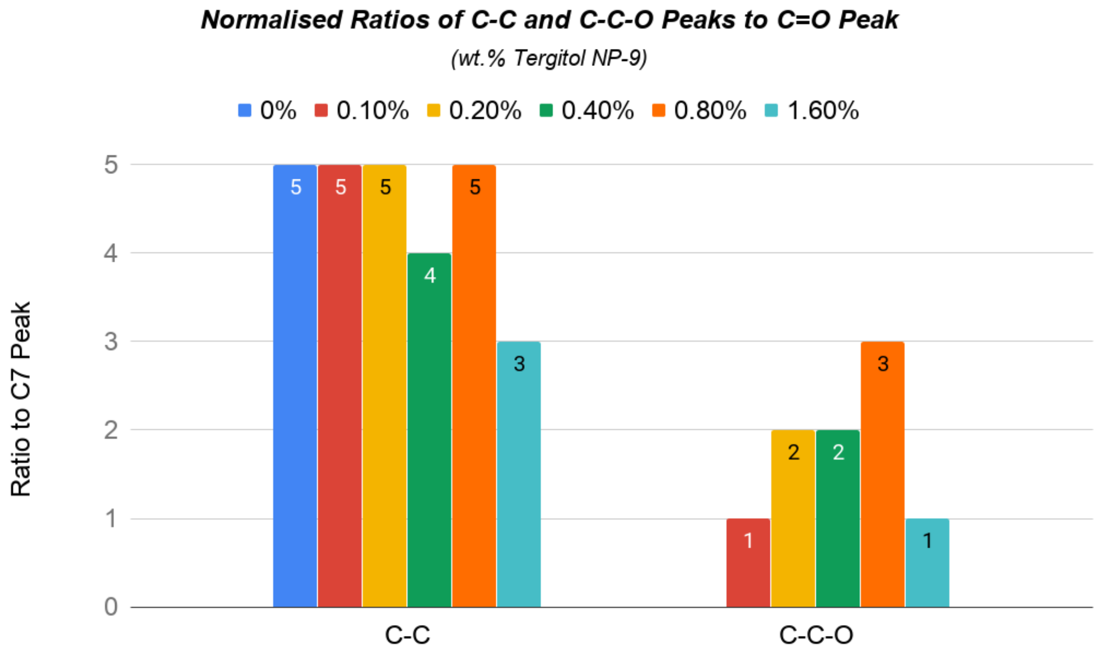

Figure 3.11: Graph showing the normalised ratios of methyl and ethoxylate carbon to the carbonyl in paracetamol

3.5 Conclusions

The laboratory instrument *EnviroESCA* produces high quality data. One must be careful to achieve the right pressure balance in order to both neutralise charging of the sample, but still retain sufficient counts to make data analysis sensible. Samples of paracetamol exposed to 1.6% w/w Tergitol NP-9 was shown to consist of both a minimum amount of adventitious carbon, and Tergitol NP-9. At lower concentrations of Tergitol NP-9 in aqueous medium, it appears that either insufficient adventitious carbon is removed from the surface of the samples, or too much surfactant is depositing on the surface. Finally, the low binding energy methyl peak fitted in the ultra-clean paracetamol sample was not present in any of the powder samples. The implication here being that the surface of the sample was not quite as pristine as the experiments demand. Therefore, further work was needed to determine a method for ensuring the cleanliness of the samples.

Chapter 4

Preparation of Organic Surfaces for Surface Analysis

4.1 Introduction

4.1.1 Motivation

Having prepared and analysed a paracetamol film prepared under UHV conditions, a base line for the analysis of *real world* paracetamol samples was established. Various studies have shown however, that surface contamination can be found on samples, of practically all materials, often in sufficient quantities to frustrate a meaningful quantitative analysis [73, 114, 115, 116]. Traditional methods utilised by researchers to remove contamination from samples in UHV are unfortunately inappropriate for use on most organic crystalline materials. For example, heating a metal single crystal to ~500°C will not generally destroy the sample, but will remove all adsorbed water. In contrast paracetamol, with a melting point ~170°C in the form I, will have melted long before this temperature. In fact, few organic compounds can be heated to temperatures in the >400°C range. Most will have thermally decomposed long before such temperatures are reached. Similarly, high energy ion beams, such as argon ions are also incompatible with organic crystalline materials, as they will rapidly damage the sample being analysed. Therefore, new methods are needed to aid in the surface analysis of organic crystals. In this chapter the principal method explored is the application of the organic solvent dichloromethane (DCM). Paracetamol is insoluble in DCM, while many types of carbon contamination are soluble in DCM. The hypothesis is that DCM will remove the majority of the contamination, leaving the paracetamol largely undisturbed. Part of this work was done collaboratively with Alexandru A. Moldovan, EPSRC Centre for Doctoral Training in Complex Particulate Products and Processes, University of Leeds.

4.1.2 Aims

- To determine an appropriate solvent with which to treat organic crystal surfaces to remove adventitious carbon contamination.
- To determine the level of contaminant removal achieved by solvent treatment.
- To ensure that any cleaning regime does not negatively impact the surface topography of single paracetamol crystals.

4.2 Materials and Methods

4.2.1 Laboratory XPS

Laboratory experiments were carried out on a SPECS EnviroESCA NAP-XPS instrument. The pressure in the analysis chamber was produced by introduction of Ar gas at ∼8 mbar. Each survey spectrum was conducted twice and the results summed. Each high-resolution scan was performed six times and summed. Survey spectra were acquired across a binding energy range of 1470 eV to -3eV, with a pass energy of 100 eV and step increments of 1 eV. Each step was analysed for 0.1 seconds. High-resolution spectra were acquired at a pass energy of 30 eV and step increments of 0.1 eV. Each step was analysed for 1 second.

4.2.2 Paracetamol Samples

Four samples were analysed, ∼1 g each of the following powders;

- Paracetamol powder washed in ultra pure water. (see Chapter 3)
- Unwashed paracetamol powder (as received). (see Chapter 3)
- Paracetamol powder washed in ultra pure water, then washed in >99.9% pure dichloromethane.
- Paracetamol single crystal.

The method by which the washed powder samples were prepared was as follows; A solution of saturated paracetamol in ultra pure water was prepared by dissolving 12 g of paracetamol in 600 ml of ultra pure water. This was covered with parafilm and left under agitation at 600 rpm overnight to ensure complete dissolution. The solution was then filtered through a glass fibre filter and the supernatant collected. The supernatant was then transferred to six 100 ml beakers. ∼1 g of paracetamol was then added to each of these beakers and left for 10 minutes prior to filtration through a glass fibre filter. For this filtration step, first the surfactant containing solution was filtered off, the filter was then filled (250 ml) with ultra pure water that had been chilled to ∼3°C and rapidly drawn through the filter. This process was repeated two more times. The crystalline solid was then collected and transferred to double-sided carbon tape mounted to a sample holder.

4.2.3 Synchrotron NAP-XPS

Synchrotron work was done on the undulator beamline 23-ID-2 NSLS-II Brookhaven National Laboratory, New York, USA, using a NAP-XPS endstation. The endstation was equipped with a SPECS Phoibos 150 NAP electron analyser and a SPECS 1D-delay line detector. All experiments were performed under a pressure of ∼4 mbar (3 Torr) ultrapure water. Paracetamol single crystals used during the experiments were affixed to a sample holder by double sided carbon tape before being cleaned. The cleaning was achieved by soaking a single sheet of precision lens tissue with dichloromethane (DCM). This was then drawn across the surface of the crystal in a single steady motion, three times. The crystal was then blasted with inert gas (N_2) for ∼3 seconds to remove any residual solvent (Figure 4.1).

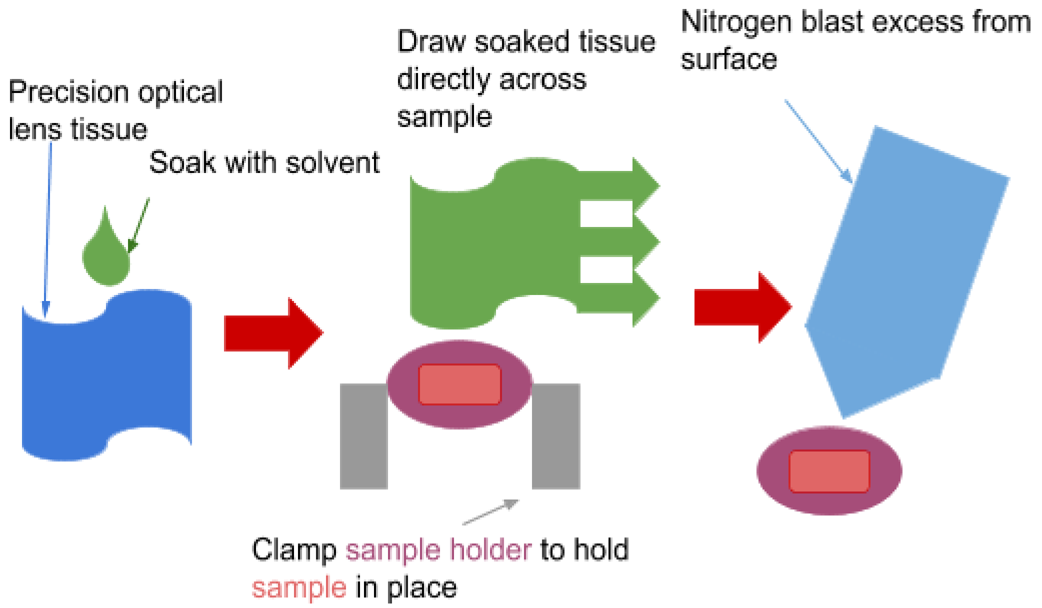

Figure 4.1: Solvent cleaning of organic crystal surfaces

The paracetamol single crystal used in these experiments was crystallised from ethanol solution by using the slow evaporation method. This involved dissolving an excess of paracetamol (BioXtra, Sigma-Aldrich) in ethanol (>99.9% Ethanol Absolute, Fischer Scientific) and leaving covered with parafilm overnight, subject to agitation. This was to ensure complete saturation of the ethanol with paracetamol. The resultant suspension was then passed through a glass fibre filter via Büchner filtration and the supernatant collected. The supernatant was then decanted into a number of clean glass petri dishes. These were covered with parafilm and small holes pierced in the film to allow for ethanol evaporation. Supporting atomic force microscopy (AFM) data resulted from experiments planned by AM, and conducted by AM and BT-B. AFM data were analysed by AM. Informative figures included in this text are included only where necessary to inform further XPS work. A full description of the AFM work can be found in AM's PhD thesis [117].

Survey spectra were acquired over a binding energy range of 750 eV to -10 eV with step size of 1 eV. Acquisition times were 76 s with a pass energy of 20 eV, and a beam exit slit size of 45 μm. High resolution spectra were obtained at various binding energy ranges, with a step size of 0.1 eV, and a dwell time of 0.2 s per step. These were acquired with a pass energy of 20 eV, and a beam exit slit size of 45 μm. Spectra were acquired from twelve different incident X-ray energies to take core-level spectra of three atoms, as well as survey spectra at four constant kinetic energies as shown in table 4.1. The surface analysed was determined to be the (011) facet, by comparison to a molecular mechanics based morphology prediction. The prediction was generated in the software Mercury using a force field developed by Momany et al [98, 118]. Initially with no cleaning treatment applied. The same facet was then scanned again after cleaning the crystal. Data were then compared.

Table 4.1: Incident X-ray Energy Required for Constant Kinetic Energies

	Required	**Photon**	**Energy**
Kinetic Energy (eV)	**C1s**	**N1s**	**O1s**
150	435	550	682
300	585	700	832
450	735	850	982
600	885	1000	1132
Binding Energy (eV)	**285**	**400**	**532**

4.2.4 Data Analysis

Peak fitting and spectra calibration were performed using the CasaXPS software package. Peaks in the spectra were fitted with Gaussian-Lorentzian line shapes in which there was a 30% Lorentzian contribution. In the case of the synchrotron data, peaks in the carbon high-resolution spectra were fitted by the following iterative protocol; The shoulder on the high-binding energy side of the peak was fitted first, by eye. The remaining expected paracetamol peaks were then fitted by constraining the FWHM and area under the peaks to be identical to the high-binding energy shoulder. The area under the peak representing the aromatic carbons was then increased to be four times that of the high-binding energy shoulder. An additional peak was added to represent adventitious carbon, in which the FWHM was constrained to be identical to the preceding peaks. Oxygen peaks were fitted in a similar manner whereby three Gaussian-Lorentzian peaks in which a 30% Lorentzian contribution was used, were fitted to the O1s high-resolution spectra. These peaks were constrained to have the same FWHM. Further peaks were added to the high binding energy side of the peak to represent the gas phase water. These peaks were then summed to represent the asymmetry in the gas phase. This asymmetry is a result of the differing local hydrogen bond arrangements having slightly different binding energies [119]. The spectra were then fitted using a Levenberg-Marquardt least squares algorithm. The laboratory data were treated the same way, with the exception of the oxygen 1s peaks, given there was no water present in these analyses. Data was then exported in the tab delimited text format and further processed by application of the Python 3 programming language. This process was carried out as follows;

1. Import fitted spectra from CasaXPS.

2. Background subtract all spectra and normalise all spectra to the intensity of the high-binding energy carbon shoulder.
3. Comparisons made across different spectra.
4. Plots were created using the Matplotlib [92] third-party library for the python 3 programming language.

Furthermore, data analysis utilised the Pandas data analysis library [91] and Scipy scientific python library [88].

4.3 Results

4.3.1 Laboratory Methods

The C1s spectrum of the dichloromethane cleaned powder was compared to that of the water washed powder in the previous chapter. The total C1s integral with the normalised DCM washed spectrum was 15% lower than that of the water washed sample. Also observed in the comparison between the two spectra was the additional intensity on the low binding energy side of the DCM spectrum. Figure 4.2 shows the comparison of the two spectra. The red spectrum was obtained from a powder sample cleaned with dichloromethane (DCM). The blue spectrum was obtained from a powder sample cleaned with ultra pure water.

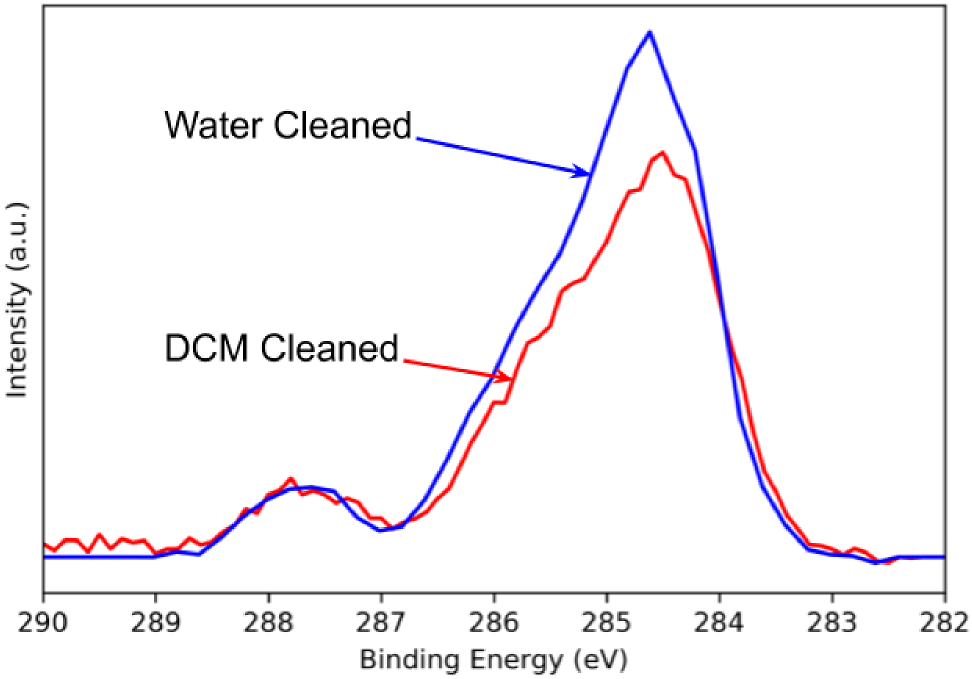

Figure 4.2: Comparison of the C1s XPS spectra of paracetamol powders cleaned with ultra pure water or DCM

The fitted C1s spectrum for the DCM cleaned sample of paracetamol contained an additional peak at a lower binding energy to the aromatic carbon peak. There was considerably less intensity contributed by the adventitious carbon peak than for the water cleaned sample. Figure 4.3 B shows the fit of the spectrum obtained for the DCM cleaned paracetamol powder. The fit shows four peaks of similar intensity, the paracetamol C-C peak (black), the amide (C-N, magenta), the hydroxyl (C-OH, cyan), and the carbonyl (C=O, orange). It also shows the aromatic carbon peak (green) and the adventitious carbon (blue). The aromatic peak is ~4 times the intensity of the other paracetamol peaks. The adventitious carbon was fitted at ~2 times the intensity of the other paracetamol peaks. To aid in the interpretation of the data, figure 3.5 is reproduced here as figure 4.3 A.

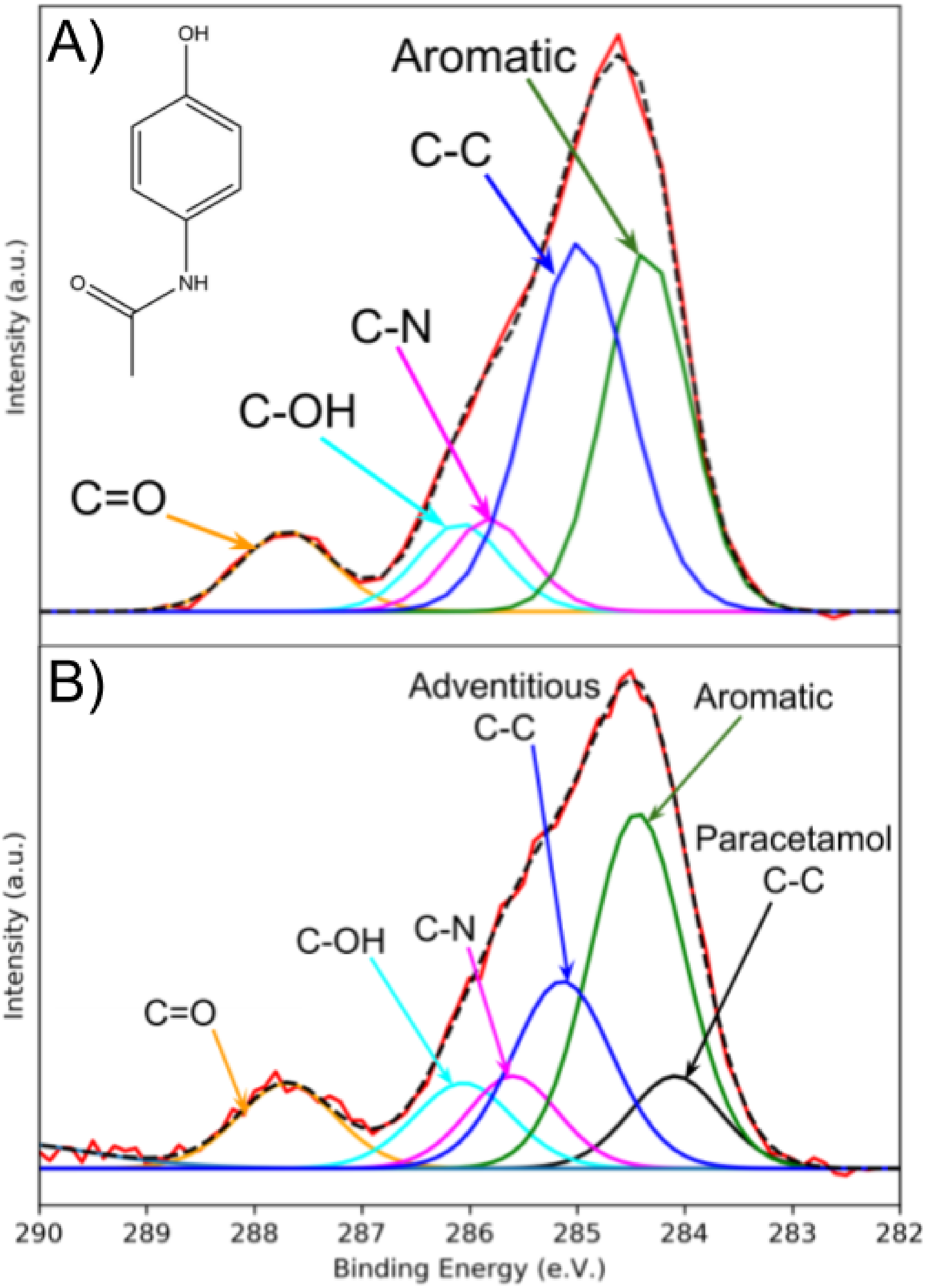

Figure 4.3: Fitted C1s XPS spectra of paracetamol powder cleaned with DCM

Where A is a spectrum obtained prior to DCM treatment, and B is a spectrum obtained from the same sample after DCM treatment.

4.3.2 Synchrotron Methods

Initial survey scans of the DCM cleaned single crystal at both 1000 eV and 550 eV photon energies yielded spectra that contained only peaks related to carbon, nitrogen, and oxygen. No Cl was observed in any of the spectra. Figures 4.4 and 4.5 show both sets of survey spectra, where Cl would be expected at ∼200 eV binding energy. Though initially, the intention was to take a number of scans according to table 4.1 in order to maintain photon kinetic energies across elements, limitations of the end station made this impossible. In the survey spectrum of a paracetamol single crystal, at 1000 eV photon energy, Figure 4.4 the only major peaks identified were those related to carbon, oxygen, and nitrogen. At ∼200 eV binding energy, there was no chlorine detected. In the survey spectrum of a paracetamol single crystal, at 550 eV photon energy, Figure 4.5 the only major peak identified was that related to carbon. Neither an oxygen peak nor nitrogen peak were observed at this photon energy due to limitations with the end station at the beam line. At ∼200 eV binding energy, there was no chlorine detected.

Table 4.2: Elemental analysis of paracetamol surface before and after DCM exposure

Photon Energy (eV)	**C1s**	**%**	**N1s**	**%**	**O1s**	**%**
	Before	*After*	*Before*	*After*	*Before*	*After*
682	91	88	2	3	7	9
832	81	65	3	1	16	34
982	71	47	3	0	26	53
1132	73	73	3	5	24	22

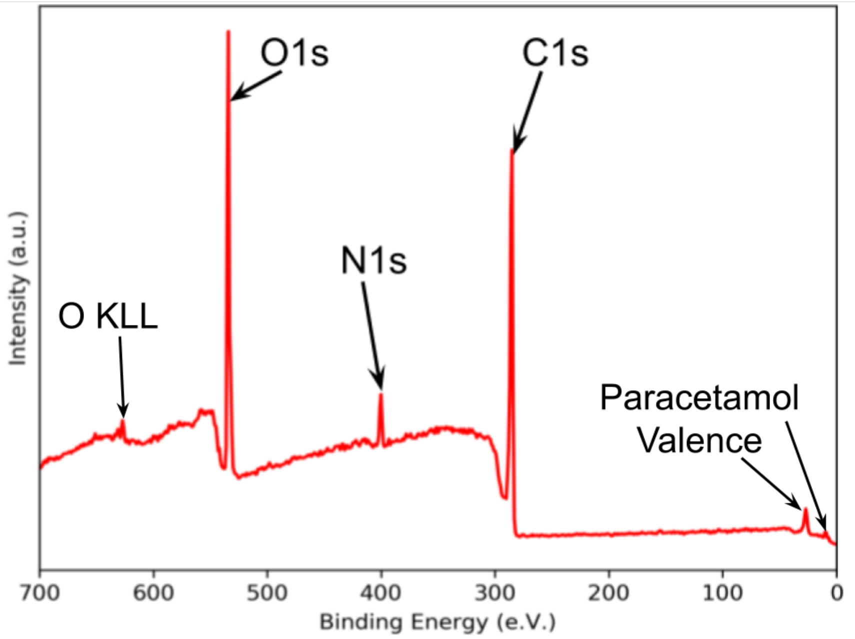

Figure 4.4: Survey spectrum of a paracetamol single crystal at 1000 eV photon energy

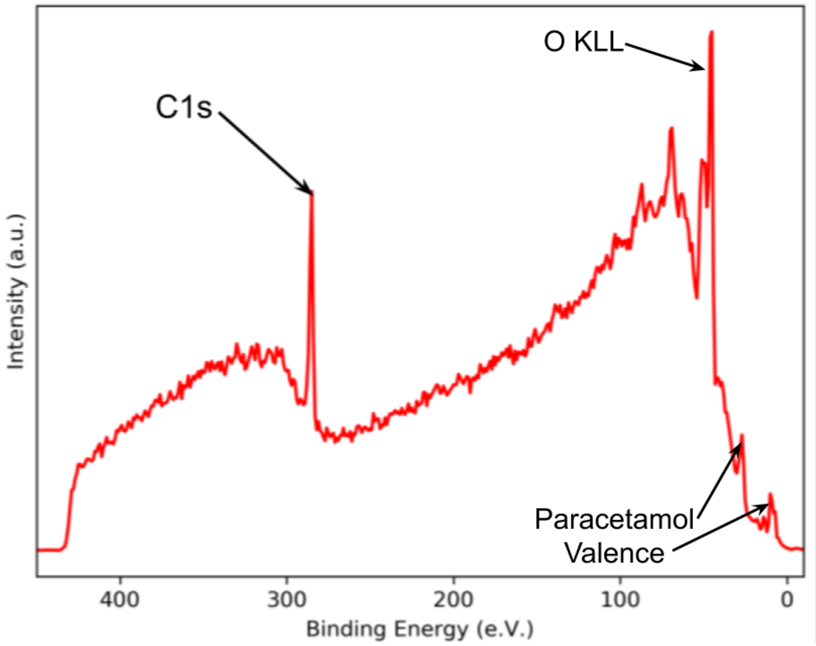

Figure 4.5: Survey spectrum of a paracetamol single crystal at 550 eV photon energy

C1s

The most surface sensitive measurement obtained for the C1s peak was at 550 eV photon energy. In the spectrum obtained from the crystal before DCM treatment, the adventitious carbon had ∼25% more intensity than that fitted in the spectrum obtained after the DCM treatment. Furthermore, the low binding energy paracetamol C-C peak was observed in the spectrum after DCM treatment, but not in the spectrum prior to DCM treatment. Figures 4.6 and 4.7, show the pre-DCM treatment and post-DCM treatment spectra, respectively. The pre-treatment spectrum showed no low binding energy C-C peak in the spectrum. The adventitious carbon (dashed blue), was fitted at only marginally less intensity of that of the aromatic peak (orange). The amide carbon (C-N, magenta), hydroxyl (C-OH, cyan), and carbonyl (C=O, green), were all fitted at similar intensity. The aromatic peak is four times the intensity of these three peaks. The post-DCM treatment spectrum showed the low binding energy C-C peak (solid blue) at similar intensity to the amide, carbonyl, and hydroxyl peaks. The adventitious carbon (dashed blue), was fitted at 75% of the intensity of that of the aromatic peak (orange). The amide carbon (C-N, magenta), hydroxyl (C-OH, cyan), and carbonyl (C=O, green), were all fitted at similar intensity. The aromatic peak is four times the intensity of these three peaks.

At the most bulk sensitive measurement obtained for the C1s, in this case 1000 eV photon energy, the paracetamol C-C peak at the low binding energy side of the main peak is still present, albeit at a slightly higher binding energy than in the more surface sensitive measurement. The same disappearance is evident in the more bulk sensitive comparison between the pre and post-DCM treatment spectra. In the more bulk sensitive spectrum of the crystal prior to DCM treatment, there was more adventitious carbon

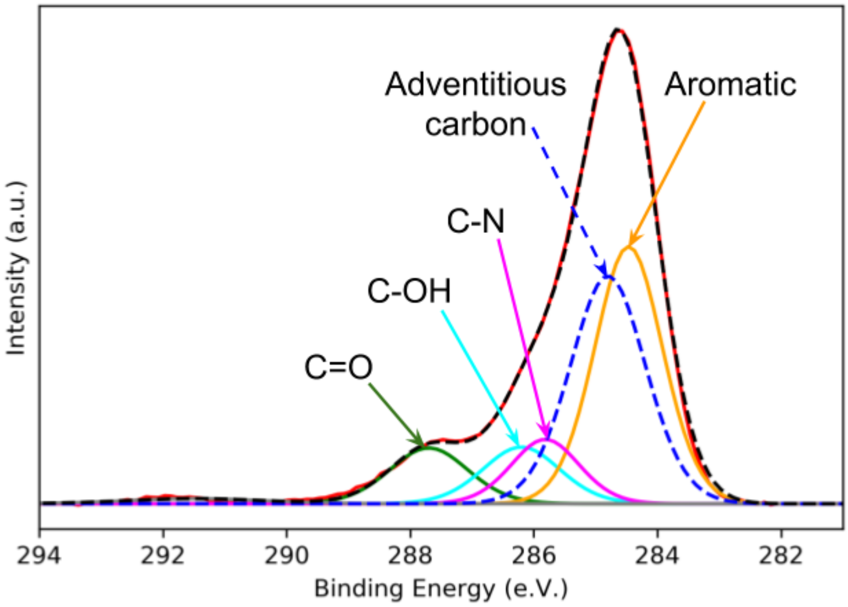

Figure 4.6: Detailed spectrum of a paracetamol single crystal surface C1s peak prior to DCM cleaning at 550 eV photon energy

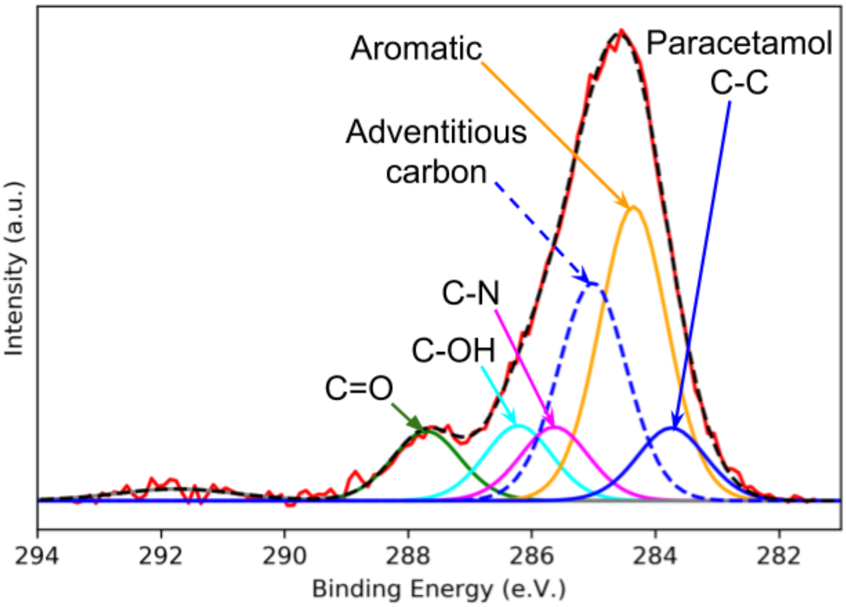

Figure 4.7: Detailed spectrum of a paracetamol single crystal surface C1s peak after DCM cleaning at 550 eV photon energy

detected than in its respective more surface sensitive spectrum. This implies that the distribution of adventitious carbon contamination is not homogenous across the surface. Figures 4.8 and 4.9 show spectra of the crystal surface before and after cleaning with DCM, respectively. In the spectrum of the crystal prior to DCM treatment, no low binding energy C-C peak was observed. The adventitious carbon (dashed blue), was fitted at slightly greater intensity than that of the aromatic peak (orange). The amide carbon (C-N, magenta), hydroxyl (C-OH, cyan), and carbonyl (C=O, green), were all fitted at similar intensity. The aromatic peak is four times the intensity of these three peaks, whereas in the spectrum of the post-DCM treated sample, the low binding energy C-C peak was observed (solid blue) at a similar intensity to the amide, carbonyl, and hydroxyl peaks. The adventitious carbon (dashed blue), was fitted at around 75% of the intensity of that of the aromatic peak (orange). The amide carbon (C-N, magenta), hydroxyl (C-OH, cyan), and carbonyl (C=O, green), were all fitted at similar intensity. The aromatic peak is four times the intensity of these three peaks.

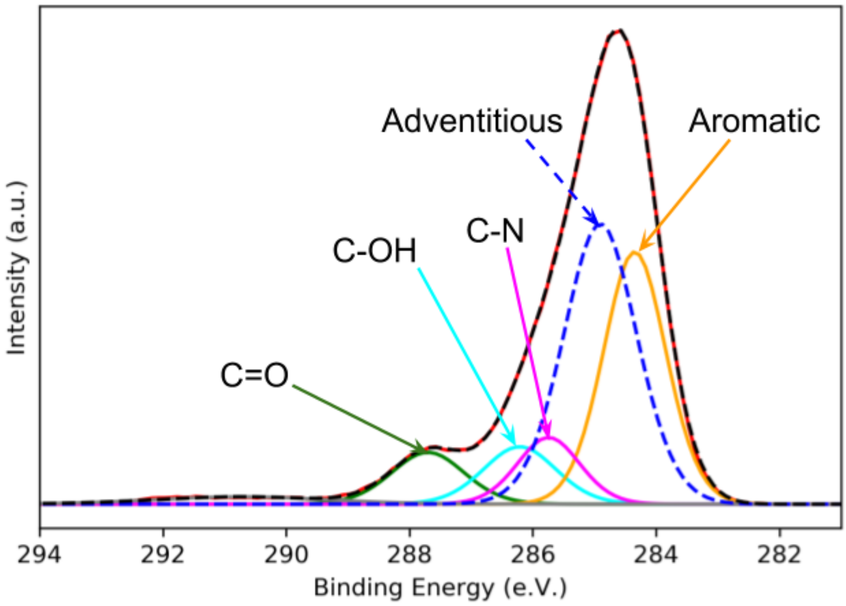

Figure 4.8: Detailed spectrum of a paracetamol single crystal surface C1s peak prior to DCM cleaning at 1000 eV photon energy

O1s

The more surface sensitive measurements in the case of the O1s peaks were done at 682 eV photon energy. In these scans the majority of the observable signal was as a result of the gas phase water in the system, though this was expected. At the lower binding energy portion of the spectra the paracetamol and liquid water features were fit. In the case of the spectrum obtained of the crystal surface prior to cleaning with DCM, the paracetamol contributions were of a 2:1 ratio, favouring the hydroxyl oxygen. The liquid water contribution had a 1:1 ratio with the carbonyl oxygen. The spectrum of the crystal surface after treatment with DCM was similar in make up, but with a ∼33% reduction

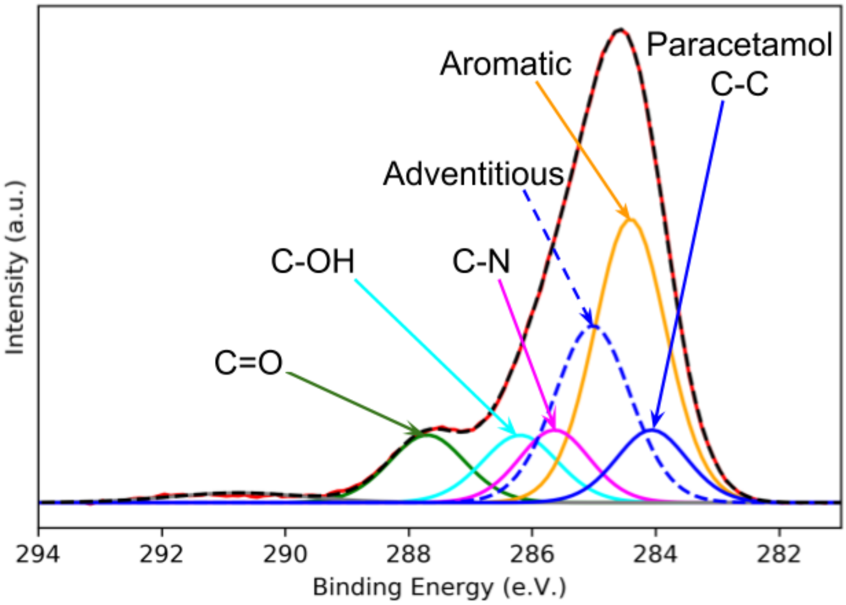

Figure 4.9: Detailed spectrum of a paracetamol single crystal surface C1s peak after DCM cleaning at 1000 eV photon energy

in the hydroxyl oxygen feature intensity. Figure 4.10 shows the oxygen features identified were the carbonyl oxygen (O=C, green), hydroxyl (O-H, blue), oxygen in liquid water (magenta), and gas phase oxygen (orange). In the more surface sensitive scans, the majority of the signal obtained came from the gas phase oxygen, leaving it difficult to make out the rest of the features. The inset therefore shows the full spectrum, whilst the main image is zoomed in on the additional features. Figure 4.11 shows the oxygen features identified were the carbonyl oxygen (O=C, green), hydroxyl (O-H, blue), oxygen in liquid water (magenta), and gas phase oxygen (orange). There is a marked reduction in hydroxyl oxygen relative to the spectrum obtained of the crystal surface before DCM treatment (fig. 4.10). In the more surface sensitive scans, the majority of the signal obtained came from the gas phase oxygen, leaving it difficult to make out the rest of the features. The inset therefore shows the full spectrum, whilst the main image is zoomed in on the additional features. In the case of the more bulk sensitive measurements, taken at 1132 eV photon energy, the gas phase water feature was still prominent; in this case more intense than in the surface sensitive measurements. The ratio of hydroxyl to carbonyl oxygen in this instance decreases from 2:1 to 1:1 after DCM treatment of the crystal surface. The ratio of carbonyl oxygen to liquid water was 2:1. This was expected, given the increase in photoelectron escape depth with the increase in photon energy. The more bulk sensitive spectra are shown in figures 4.12 and 4.13 where the oxygen features identified were the carbonyl oxygen (O=C, green), hydroxyl (O-H, blue), oxygen in liquid water (magenta), and gas phase oxygen (orange). There is a marked increase in hydroxyl oxygen relative to the spectrum obtained before DCM treatment (fig. 4.12).

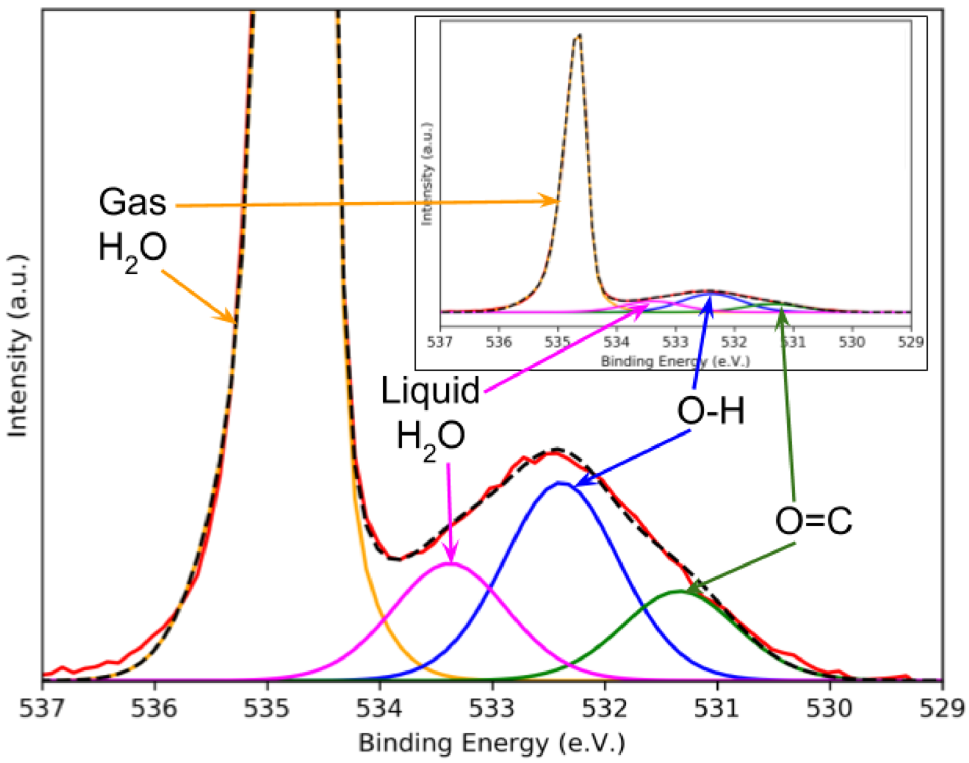

Figure 4.10: Detailed spectrum of a paracetamol single crystal surface O1s peak before DCM cleaning at 682 eV photon energy

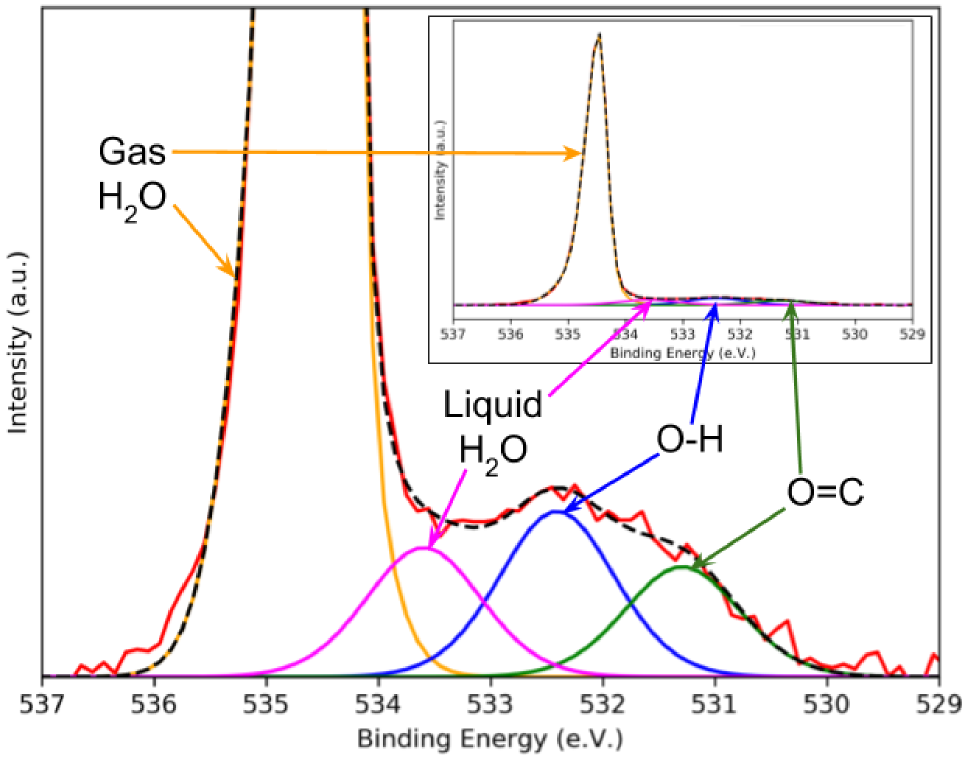

Figure 4.11: Detailed spectrum of a paracetamol single crystal surface O1s peak after DCM cleaning at 682 eV photon energy

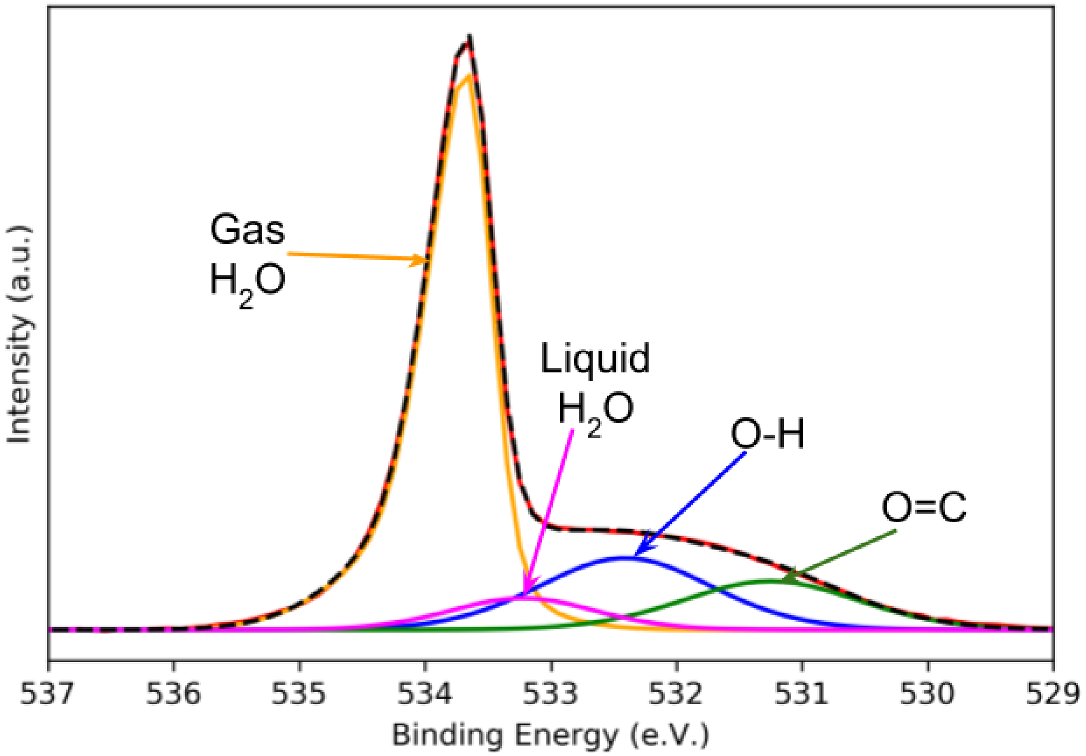

Figure 4.12: Detailed spectrum of a paracetamol single crystal surface O1s peak before DCM cleaning at 1132 eV photon energy

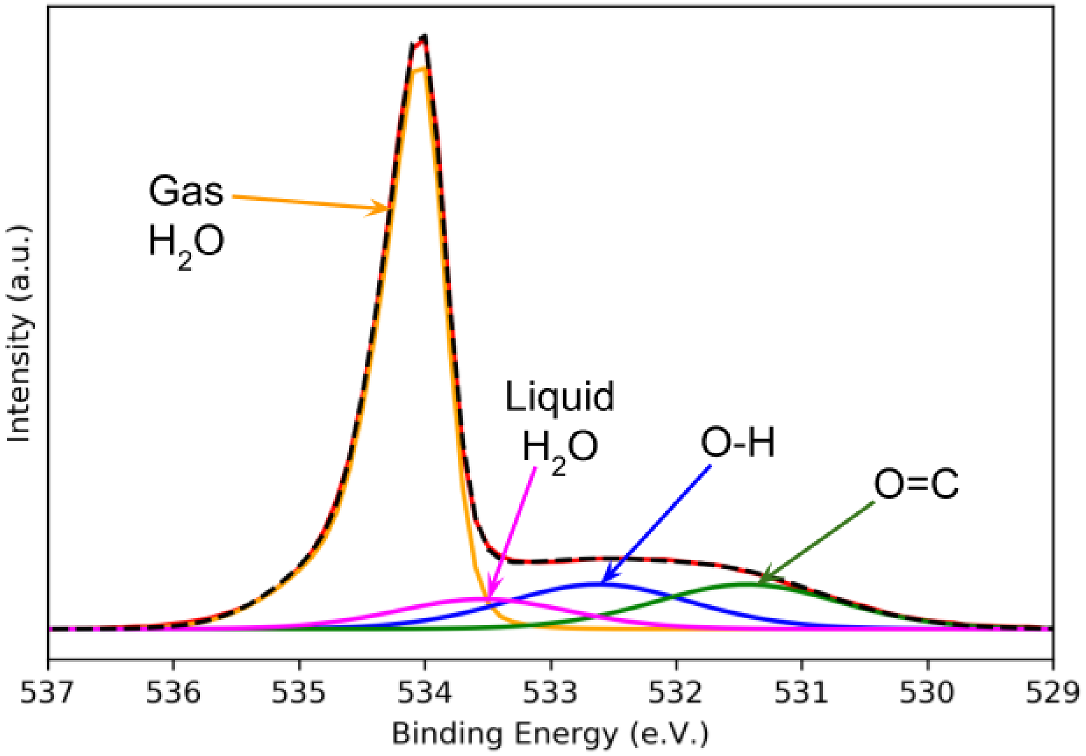

Figure 4.13: Detailed spectrum of a paracetamol single crystal surface O1s peak after DCM cleaning at 1132 eV photon energy

4.4 Discussion

Dichloromethane was selected as the solvent with which to clean the crystal surfaces after a set of experiments done in collaboration with A.M. (see chapter introduction). In these experiments, a number of different solvents (ultra pure water, ethanol, methanol, propan-2-ol, and dichloromethane) were compared for their ability to achieve as uniform a distribution in adhesion force, and as minimal a change in the surface micro structure as possible. These experiments were performed using atomic force microscopy and a full account of these experiments is presented in A.M.'s PhD thesis '*Interfacial Interactions of Faceted Organic Crystals – An in-silico study with Atomic Force Microscopy*' [117].

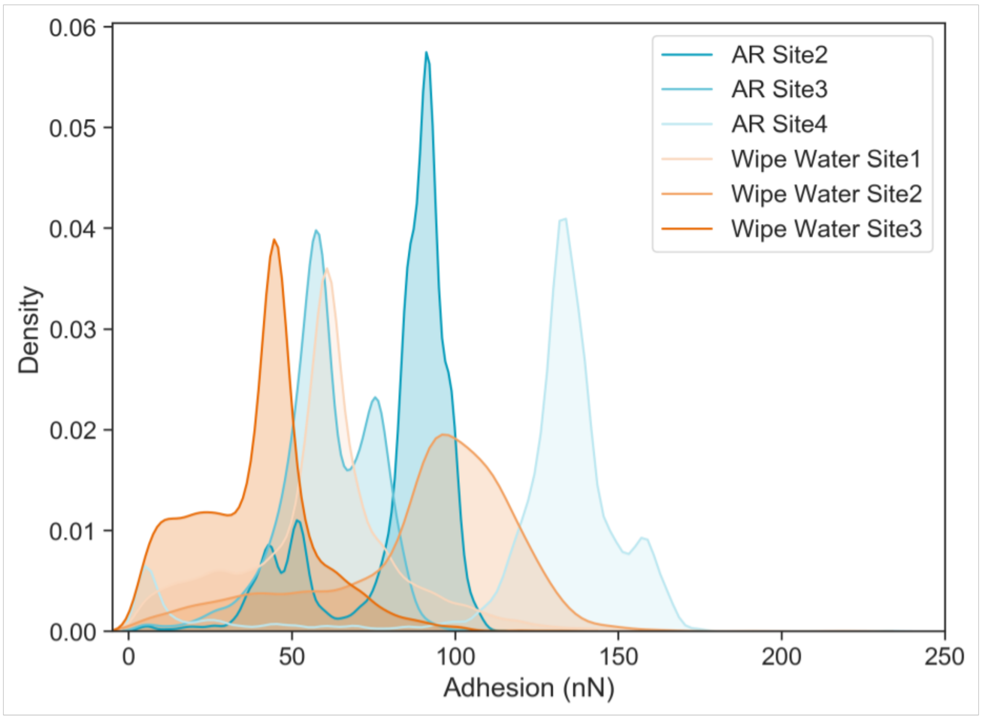

Figure 4.14: Adhesion force distribution plot of paracetamol crystal surface before & after cleaning with water

Where AR represents "as received" measurements and Wipe Water represents sites measured after water treatment. AR and Wipe Water sites are taken from the same sample, but are unrelated. (For example, AR site2 represents the second site measured before water treatment, and Wipe Water Site2 represents the second site measured after water treatment, but they are not the same site.)

Figure 4.14 shows an adhesion force distribution across the surface of a water cleaned crystal. Figure 4.15 shows microscopy images of the same surface before and after cleaning with water. Figure 4.16 shows the same for a surface cleaned with DCM. Figure 4.17 shows microscopy images of the DCM cleaned surface before and after cleaning. All other solvents tested, resulted in similar results to that of water, likely because of the solubility of paracetamol in these solvents, which dissolve paracetamol fairly readily.

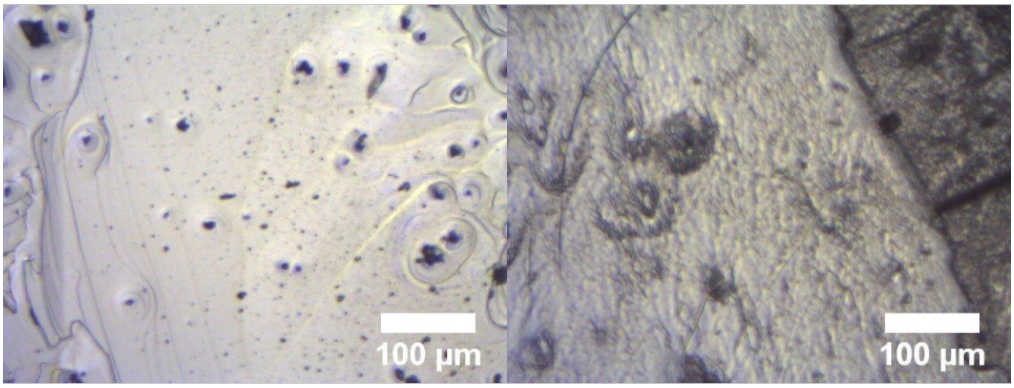

Figure 4.15: Light microscopy images of paracetamol crystal surface before & after cleaning with water

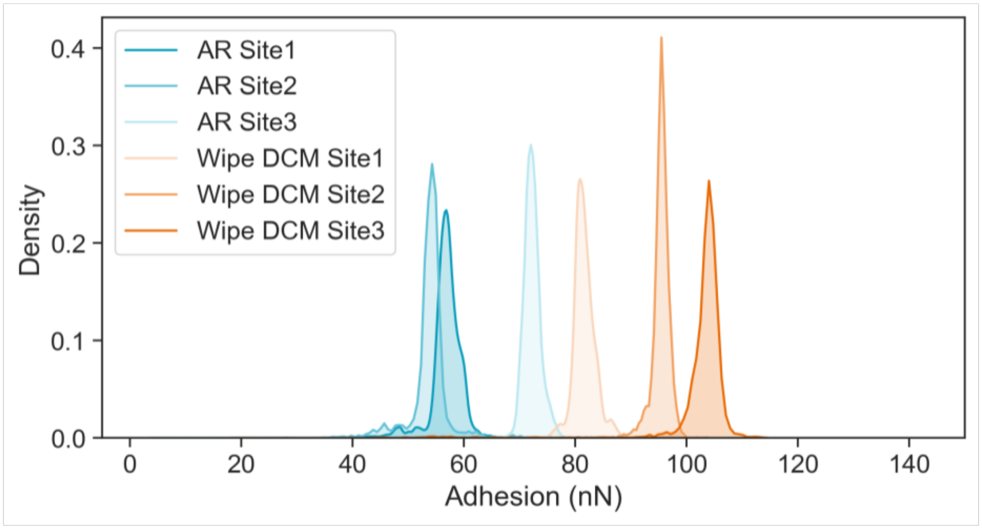

Figure 4.16: Adhesion force distribution plot of paracetamol crystal surface before & after cleaning with DCM

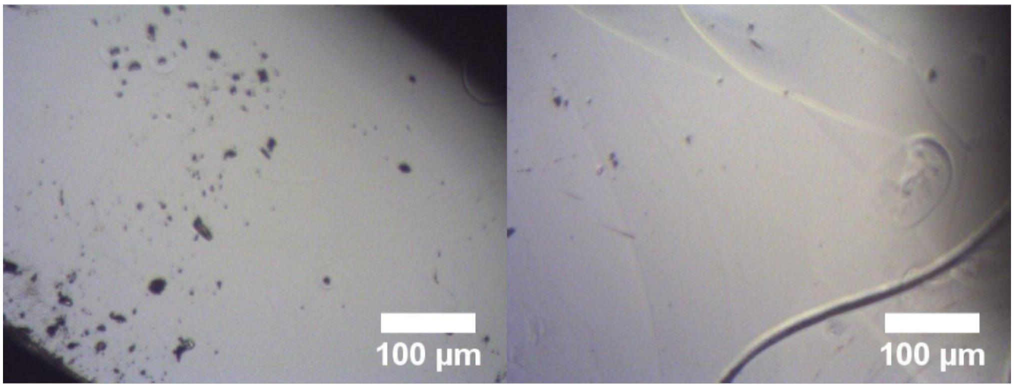

Figure 4.17: Light microscopy images of paracetamol crystal surface before & after cleaning with DCM

However, the impact on the surface of the crystal was negligible when exposed to DCM, and the adhesion force distribution across the analysis area was far more uniform than in the case of any of the other solvents. Figure 4.2 shows a marked reduction in carbon signal after DCM cleaning, compared to after cleaning with ultra pure water. In total, DCM treatment yielded a decrease in the total carbon content of 44% vs the 'as received' sample. A quick comparison of figures 3.5 and 4.3 shows visually how much contamination is being removed from the surface of the paracetamol. In the spectrum of the 'as received' sample of paracetamol (figure 3.5) the ratio of methyl to aromatic carbon is on the order of 1:1 where as post-DCM treatment, the ratio of adventitious carbon to all other components is much reduced over the 'as received' sample. The more bulk sensitive (1000 eV photon energy) C1s spectra obtained of crystal surfaces before and after treatment with DCM were compared by first normalising both to the carbonyl shoulder at the high binding energy side of the peak. After comparing the integrals of the normalised spectra, the resultant decrease in carbon signal after DCM treatment was 19%. While not as high as that observed with the powder samples, the cleaning regime was significantly different, in order to ensure as little disturbance to the surface of the crystal as possible. In the case of the more surface sensitive (550 eV) C1s experiments similar results were obtained. Though in this case the reduction in carbon signal on cleaning the crystal surface with DCM was 7%. Figures 4.18 and 4.19 show a comparison of paracetamol C1s spectra of a single crystal surface both before (blue) and after (red) treatment with DCM. Unfortunately, the method of cleaning the single crystals was not as effective as that used to clean the paracetamol powders, at least in terms of removing adventitious carbon from the surface of the crystal. However, a balance needed to be drawn between the removal of adventitious carbon, and the deposition of recrystallised paracetamol on the surface of the crystal. The aim of the experiments was to remain facet specific. Hence, had the crystal been simply dipped into or rinsed with DCM, some dissolution of the crystal would have occurred with large volumes of DCM. Given the rapid evaporation rate of DCM, this would result in the dissolved paracetamol recrystallising on the crystal surface.

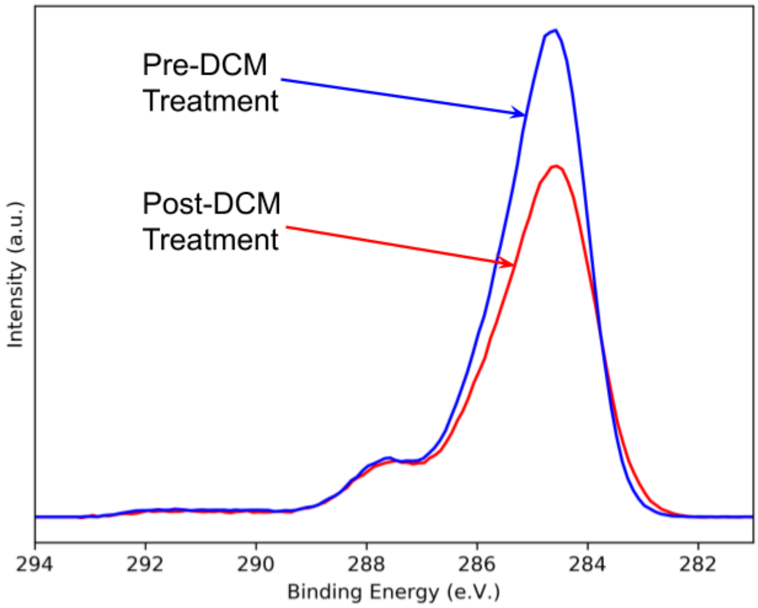

Figure 4.18: Comparison of paracetamol C1s spectra before and after DCM treatment at 1000 eV photon energy

Table 4.3: Peak parameters of paracetamol C1s fits before and after DCM exposure at 1000 eV photon energy

Photon Energy (eV)	Area (%)	After FWHM (eV)	Exposure Position (eV)	Area (%)	Before FWHM (eV)	Exposure Position (eV)
C-C	9	1.4	284.0	-	-	-
C-OH	9	1.5	286.2	8	1.5	286.2
C-N	9	1.4	285.6	8	1.2	285.7
C=O	9	1.5	287.7	8	1.4	287.7
Aromatic	37	1.4	284.4	32	1.2	284.4
Adventitious	24	1.5	285.0	41	1.4	284.9

The oxygen spectra when normalised to the integrals of the carbonyl oxygen peaks both contained an observable reduction in contamination. The expectation for a pure paracetamol sample was a 1:1 ratio of hydroxyl to carbonyl oxygen. A great deal more hydroxyl oxygen was determined to have been removed than carbon contamination. With respect to the more surface sensitive measurements (682 eV photon energy), the oxygen

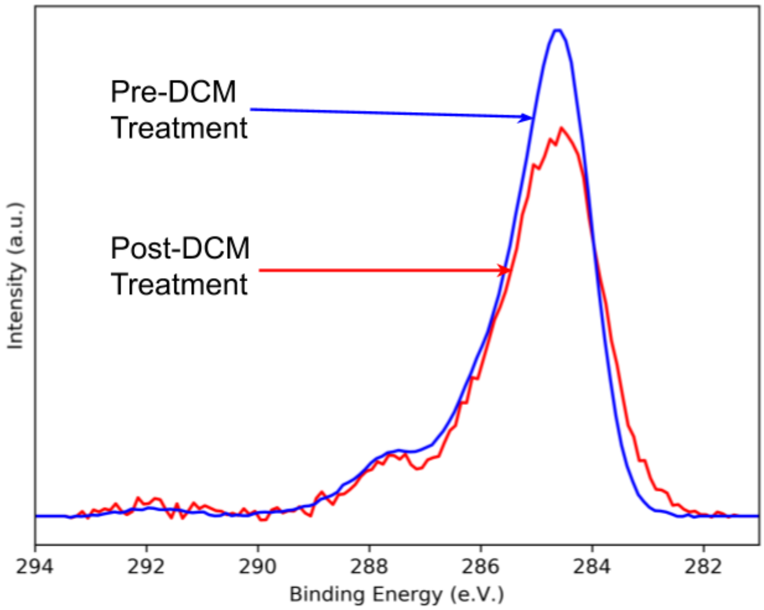

Figure 4.19: Comparison of C1s spectra of paracetamol before and after DCM treatment at 550 eV photon energy

Table 4.4: Peak parameters of paracetamol C1s fits before and after DCM exposure at 550 eV photon energy

Photon Energy (eV)	After Exposure			Before Exposure		
	Area (%)	FWHM (eV)	Position (eV)	Area (%)	FWHM (eV)	Position (eV)
C-C	9	1.3	283.7	-	-	-
C-OH	9	1.3	286.2	9	1.5	286.2
C-N	9	1.3	285.6	9	1.3	285.8
C=O	8	1.3	287.7	9	1.5	287.7
Aromatic	35	1.3	284.4	36	1.3	284.5
Adventitious	27	1.3	285.0	35	1.4	284.8

removed accounted for 33% of the hydroxyl carbon signal. Figures 4.20 and 4.21 show the paracetamol of a single crystal surface both before (blue) and after (red) treatment with DCM for the more bulk and surface sensitive measurements, respectively. The more bulk sensitive measurement of the O1s peak (1132 eV) yielded a 20% increase in intensity of the hydroxyl oxygen. This was an inversion of what was seen in the case of the surface spectrum (682 eV photon energy). In the carbon spectra, there was a greater reduction of contamination observed in the more bulk sensitive measurements, than in the more surface sensitive measurements, indicating that there is little oxygen

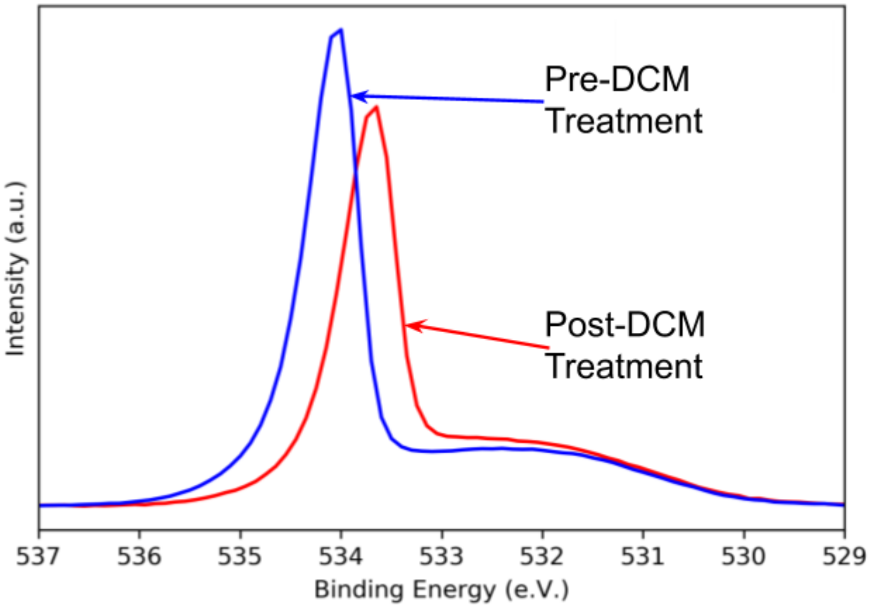

Figure 4.20: Comparison of O1s spectra of paracetamol before and after DCM treatment at 1132 eV photon energy

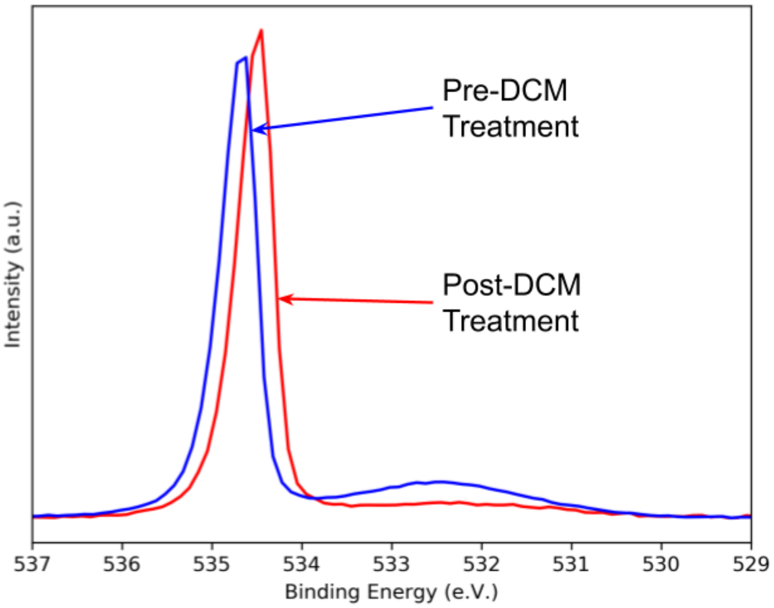

Figure 4.21: Comparison of O1s spectra of paracetamol before and after DCM treatment at 682 eV photon energy

contamination present at the surface of the sample. The sharp gas phase peak at the high binding energy side of the O1s peak also indirectly shows how much the sample is charging and the fact that surface contamination is working in some way to mitigate the level of charging in the sample. Although figures 4.20 and 4.21 show an apparent shift in the position of the gas phase water peak, the spectra were all calibrated to the carbonyl oxygen position at 531.2 eV. The apparent shift in the position of the gas phase peak, is therefore equivalent to the level of charging in the sample.

4.5 Conclusions

With respect to the aims of this chapter, the determination of an appropriate solvent for removing contamination from organic crystal surfaces, DCM is an appropriate solvent to use. The AFM and optical microscopy data presented clearly show that DCM treatment has a minimal impact on the surface micro structure. It also shows that such treatment results in minimal variations of adhesion force across the surface of the sample after treatment. The NAP-XPS data, shown in the laboratory methods section of this chapter, shows a marked reduction in the levels in the adventitious carbon post-DCM treatment. A reduction in total overall carbon signal of 44% in the DCM treated sample compared to the 'as received' sample, and a 15% reduction compared to the ultra pure water cleaned sample shows that DCM is indeed removing the majority of the contamination from the surface of the crystals, and is doing so in such a way as to not disturb the surface topography. The synchrotron data show that this stands up to a cleaning regime that does not involve immersing the crystal into DCM. However, there appears to be a reduction in the efficacy of the DCM treatment. The synchrotron data also show that the reduction in contamination is still efficacious though. Whilst it would be ideal from a surface analysis perspective to remove 100% contamination from the surface of the crystals, the objective of this work is to make determinations related to real world systems.

Chapter 5

Tergitol Deposition Structure & Quantification on a Clean Paracetamol Single Crystal Surface

5.1 Introduction

5.1.1 Motivation

In the previous chapters of this work it has been established that paracetamol single crystals can be analysed by near-ambient pressure XPS, and that density functional theory gives a theoretical basis for the analysis of the resultant data. Evidence was presented that adsorbed surfactant can be detected at the surface of the crystals and optimal exposure to surfactant is 1.6 wt.% over the experiments performed. Finally, surface cleaning was shown by use of a dichloromethane treatment of the surfaces, applied via precision lens cleaning tissues. With these pieces of evidence collected, it is feasible to both adsorb surfactant molecules to a clean paracetamol surface, and to detect the levels of adsorbed surfactant. One idea is to quantify by determining the number of surfactant molecules that are adsorbed per unit area of the crystal surface. This is of interest to researchers, as it would open up new applications in the field of organic surface analysis. It is also of interest in industrial research, as it would allow for the fine tuning of both formulations in particulate products and the processes used to create them.

5.1.2 Aims

The aims of this package of work are as follows:

- To detect adsorbed surfactant at the surface of a clean paracetamol single crystal.
- To quantify the level of adsorbed surfactant at the surface of a clean paracetamol single crystal.

5.2 Materials and Methods

Synchrotron work was carried out at the B07 'VERSOX' bending magnet beamline at the Diamond Light Source (Didcot, UK). The end station was equipped with a SPECS Phoibos 150 NAP electron analyser and a multichannel channel detector. Experiments were performed with pressure created by ultra-pure water at ~6 mbar. A large paracetamol single crystal was crystallised from ethanol solution by using the slow evaporation method. This involved dissolving an excess of paracetamol (BioXtra, Sigma-Aldrich) in ethanol (>99.9% Ethanol Absolute, Fischer Scientific) and leaving covered with parafilm overnight, subject to agitation. This was to ensure complete saturation of the ethanol with paracetamol. The resultant suspension was then passed through a glass fibre filter via Büchner filtration and the supernatant collected. The supernatant was then decanted into a number of clean glass petri dishes. These were covered with parafilm and small holes pierced in the film to allow for ethanol evaporation. Surface cleaning and XPS data analysis were performed using the exact same methods detailed in the previous chapter, with the exception of sample mounting procedures. The crystal was mounted to a sample holder by means of tantalum foil that had holes punched in it with a standard office hole punch. That is, the sample was placed onto the sample holder and the tantalum foil placed over the crystal with the holes exposing the surface of interest. The edges of the foil were then held in place by means of clips built into the sample holder. After initial analysis of a clean paracetamol crystal, the crystal was removed from the beamline end station and cleaned as before the analysis. The crystal was then exposed to ultra-pure water containing 1.6 wt.% Tergitol NP-9 surfactant (>99.9%, Sigma-Aldrich). This mixture also contained paracetamol, dissolved to saturation. The paracetamol saturated solutions were made up by adding an excess of paracetamol to ultra-pure water and stirring for 24 hours to ensure complete dissolution. The resultant ultra-pure water/paracetamol suspension was then filtered through a glass fibre filter and the paracetamol saturated supernatant collected. This was then partitioned into four beakers. One of these beakers was then dosed with Tergitol NP-9 to a total of 1.6 wt.%. The surfactant exposure was performed by first immersing the crystal into the Tergitol containing saturated solution using a pair of tweezers, and agitating for 1 second. The crystal was then rapidly immersed into a succession of three solutions composed of ultra-pure water saturated with dissolved paracetamol. The crystal was then rapidly dried by blasting with N_2 gas. Figure 5.1 shows a diagram of this process, in which a clean paracetamol single crystal (grey), is first exposed to a 1.6 wt.% Tergitol NP-9 containing solution (green arrow) and agitated for ~1 second (yellow arrows). The crystal is then removed and sequentially exposed to three beakers containing only paracetamol saturated ultra-pure water (blue arrows).

The crystal was then reintroduced to the end station and the analysis repeated with the surfactant exposed crystal on the same facet as before the surfactant exposure.

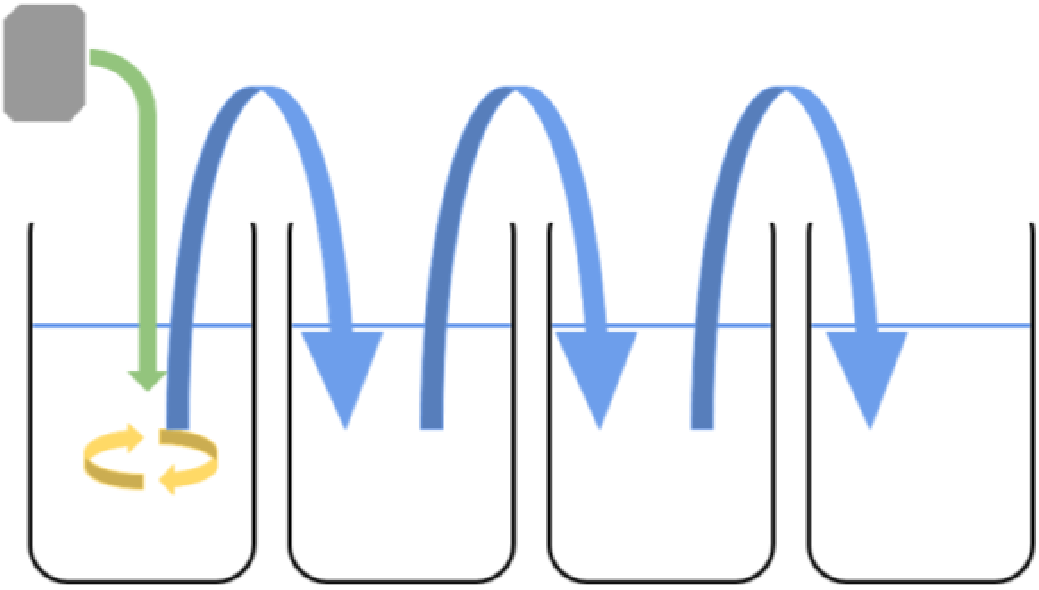

Figure 5.1: Schematic diagram of paracetamol exposure to Tergitol NP-9

Determination of the number of surfactant molecules on the surface of the crystals was carried out according to a layers on a plane model [120], in which the intensity of functions fitted to the C1s XPS spectra were partitioned according to the molecule they originated from. It should be noted here, that it was assumed all carbon intensity was a result of either paracetamol or Tergitol NP-9. It was also assumed that in the case of the methyl carbon peak, if no low binding energy paracetamol peak could be identified, intensity equal to the paracetamol carbonyl shoulder was subtracted from the Tergitol contributions and added to the paracetamol contributions. The layers on a plane model states that the intensities of photoelectrons of atom *i* in a two layer sample, that is, the bulk crystal, and a single overlayer of atom *k* can be calculated with the following equations [120]:

For the substrate

$$I_i = N_i \lambda_i \cos\Theta \exp\left(\frac{-S}{\lambda_i}\cos\Theta\right)\left[1-\exp\left(\frac{-B}{\lambda_i}\cos\Theta\right)\right] \tag{5.1}$$

and for the overlayer

$$I_k = N_k \lambda_k \cos\Theta\left[1-\exp\left(\frac{-S}{\lambda_k}\cos\Theta\right)\right] \tag{5.2}$$

where I_x is the intensity of the photoelectron line from atom x, N_x is the number of photoelectrons per unit area emitted from atoms of x, λ_x is the IMFP of a photoelectron emitted from an atom x, S is the thickness of a surface overlayer, B is the thickness of the bulk being analysed, and Θ is the angle between the escaping photoelectrons and the surface normal. The IMFP of the photoelectrons, the number of atoms in each layer, and the thickness of the layers are the unknown quantities. The first parameter N_x can be calculated by dividing the intensity of the photoelectron peak detected by the photoionisation cross section of the atom (σ) at the beam energy used multiplied by the IMFP of the escaping photoelectron (eq. 5.3).

$$N_x = \frac{I_x}{\sigma_x \lambda_x} \tag{5.3}$$

Photoionisation cross sections in this analysis were interpolated from literature values published by Yeh and Lindau [56]. The IMFP of the escaping photoelectrons was calculated using the CS2 method of Cumpson and Seah [120]:

$$\lambda_x = 0.316 a^{\frac{3}{2}} \left(\frac{E}{Z^{0.45} \left[\ln \left(E/27 \right) + 3 \right]} + 4 \right) \tag{5.4}$$

in which E is the kinetic energy of the photoelectrons, Z is the mean atomic number of the atoms in the molecule from which the photoelectron was ejected, and a is a lattice parameter. The lattice parameter is calculated with equation 5.5.

$$a = \sqrt[3]{\frac{M}{\rho \cdot 602}} \tag{5.5}$$

Here, M is the mean molecular mass of the molecule from which the photoelectron was ejected, and ρ is the density of the material in g/cm^3. Given that N_x and λ_x can now be calculated, the remaining parameters to be determined are S and B. Therefore, if the surface overlayer thickness is calculated first, both equations can be rearranged. To solve for S in the case of eq. 5.2 and then knowing S, for B in the case of eq. 5.1 rearranging 5.2 to solve for S yields;

$$S = -\frac{\lambda_k \ln \left(-\frac{I_k - \lambda_k N_k \cos \Theta}{\lambda_k N_k \cos \Theta} \right)}{\cos \Theta} \tag{5.6}$$

with S now known, eq. 5.1 can now be rearranged to solve for B;

$$B = -\frac{\lambda_i \ln \left(-\frac{I_i - N_i e^{-\frac{S \cos \Theta}{\lambda_i}} \lambda_i \cos \Theta}{N_i e^{-\frac{S \cos \Theta}{\lambda_i}} \lambda_i \cos \Theta} \right)}{\cos \Theta} \tag{5.7}$$

The results from each photon energy were then tabulated and both the relative intensity of the Tergitol carbon signal, and the relative intensity of the paracetamol carbon signal were calculated. The total paracetamol carbon signal was then divided by the number of carbon atoms in a paracetamol molecule. The same was done for Tergitol. This yielded a relative intensity from surfactant molecules, and a relative intensity from paracetamol molecules. Any outliers in the number of molecules were identified as being values that were greater than two standard deviations from the mean.

A matrix of variable photon energy experiments was carried out as described in chapter 4. Unfortunately, some of the lower photon energy experiments were unsuccessful due to flux limitations at the B07 beamline end station. These were the 435 eV, 550 eV, and 585 eV experiments. However, more than sufficient data were collected over the other nine photon energies used. Representative data are discussed from 1132 eV and 1000 eV photon energies.

5.3 Results

Quantification of Paracetamol and Tergitol NP-9 Across All Photon Energies Used

The relative intensity of the carbon signal from both paracetamol and Tergitol NP-9 were calculated according to equations 5.1 and 5.2, where the relative intensity is the N_x term in each equation and is further calculated by equation 5.3. The results are shown in table 5.1.

The relative intensity of paracetamol molecules detected at each photon energy was calculated to decrease in accordance with an exponential decay function, with decreasing photon energy. No outliers were found in either the paracetamol quantification or the Tergitol NP-9 quantification.

Table 5.1: Quantification of Paracetamol and Tergitol NP-9 at Various Photon Energies

Photon Energy (e.V.)	**N_{NP-9} (a.u.)**	**$N_{Paracetamol}$ (a.u.)**	**Ratio Tergitol:Paracetamol (%)**
1132	32	1446	2.21
1000	19	652	2.91
982	31	540	5.74
885	29	475	6.11
850	35	401	8.73
832	25	382	6.54
735	19	149	12.75
700	18	110	16.36
682	17	62	27.42

1132 eV Photon Energy

In the absence of surfactant, the C1s spectrum at 1132 eV photon energy contained a slightly higher ratio of non-paracetamol C-C carbon to carbonyl carbon. This was recorded to be 1.1:1 non-paracetamol C-C to carbonyl. In the 1132 eV spectrum of the surface after exposure to the surfactant, the ratio of non-paracetamol C-C carbon to carbonyl carbon was increased to ~1.8:1. Figure 5.2 shows both fitted spectra. Before exposure to Tergitol NP-9 surfactant (figure 5.2 B), the paracetamol peaks were as expected with the paracetamol C-C peak at the lowest binding energy (blue), followed by the aromatic peak (orange), amide (brown), hydroxyl (purple), and carbonyl (green). The non-paracetamol C-C peak (magenta), in this instance is attributed to adventitious carbon. Also shown but not pointed out is the shake-up function (red). After exposure to Tergitol NP-9 (figure 5.2 A), the only major change in the spectrum is shown in the non-paracetamol C-C function, which has increased in intensity from approximately 1:1 relative to the carbonyl function, to approximately 2:1 (magenta). The remaining functions, aromatic (brown), paracetamol C-C (purple), amide (red), hydroxyl (green),

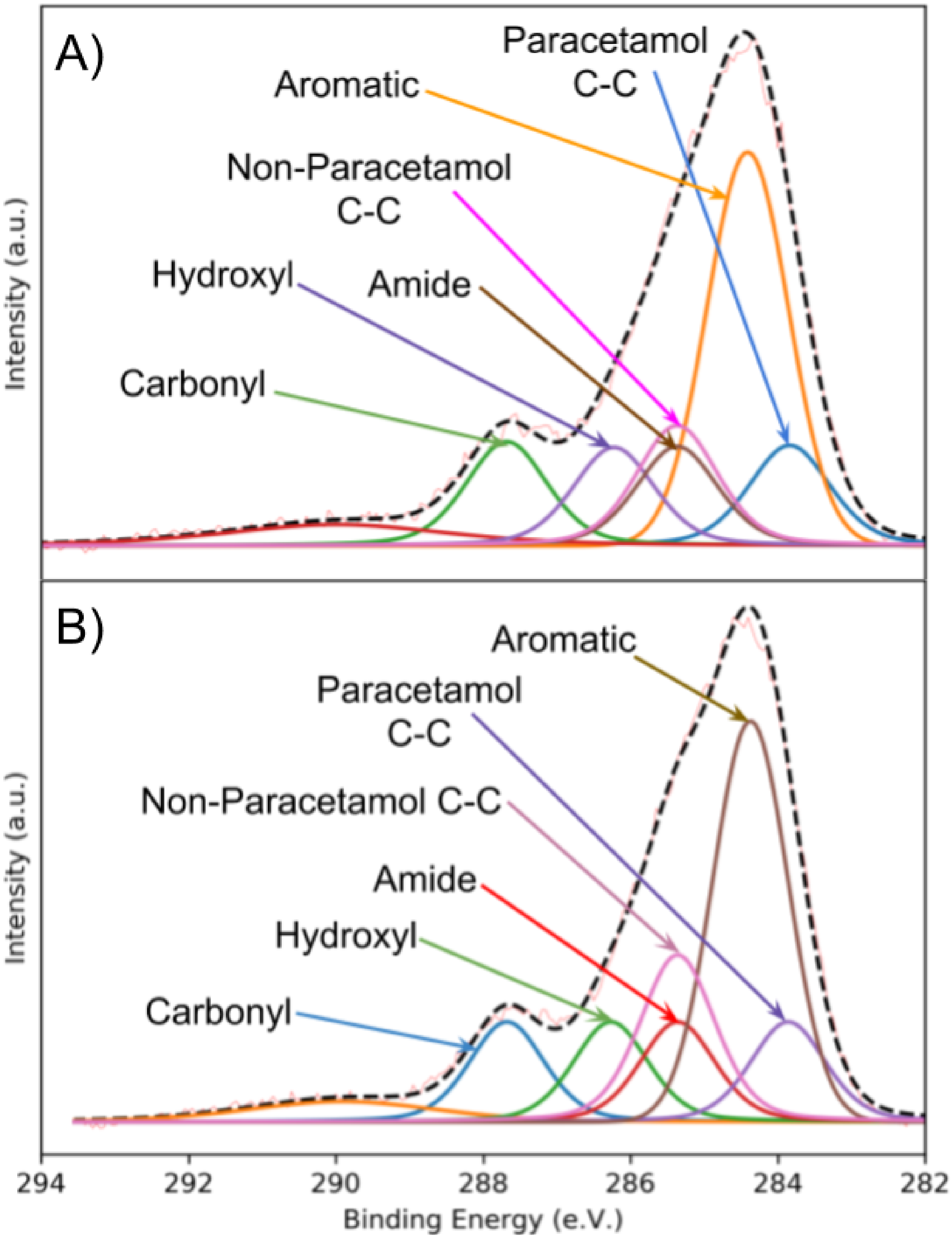

Figure 5.2: C1s XPS spectrum paracetamol before (B) and after (A) exposure to Tergitol NP-9 at 1132 eV photon energy

and carbonyl (blue) remained relatively unchanged. The total number of molecules calculated to be present at this photon energy was 32 Tergitol NP-9 molecules and 1446 paracetamol molecules.

Table 5.2: Fit parameters for Tergitol on paracetamol at 1132 eV

	Assignment (e.V.)	**Position (e.V.)**	**Relative Area (e.V.)**	**FWHM (e.V.)**
After Tergitol Exposure	C=O	287.7	1	1.2
	C-OH	286.3	1	1.2
	C-N	285.4	1	1.2
	C-C	283.9	1	1.2
	Adventitious	285.4	2	1.2
	Aromatic	284.4	4	1.2
Before Tergitol Exposure	C=O	287.7	1	1.3
	C-OH	286.2	1	1.3
	C-N	285.4	1	1.3
	C-C	283.9	1	1.3
	Adventitious	285.4	1.3	1.3
	Aromatic	284.4	4	1.3

1000 eV Photon Energy

At 1000 eV photon energy, in the pre-surfactant spectrum there was a noticeable reduction in contamination relative to the 1132 eV photon energy spectrum at ∼25% the intensity of the carbonyl function. In the spectrum acquired after surfactant deposition, there was a large increase in the amount of carbon detected from non-paracetamol sources. The low binding energy C-C peak from paracetamol could not be fit, and an additional peak had to be fitted at the high binding energy side of the paracetamol shoulder. This was assigned to beam damage in the ethoxylate chain of the Tergitol NP-9 surfactant. The relative intensity of Tergitol NP-9 molecules was calculated to be 19, with the relative intensity of paracetamol at 652 molecules. Figure 5.3 shows the spectra at 1000 eV photon energy, before exposure to Tergitol NP-9 surfactant (B), the paracetamol peaks were as expected with the paracetamol C-C peak at the lowest binding energy (purple), followed by the aromatic peak (brown), amide (red), hydroxyl (green), and carbonyl (blue). The non-paracetamol C-C peak (magenta), in this instance is attributed to adventitious carbon. After exposure to Tergitol NP-9, the low binding energy paracetamol C-C peak could not be fitted in the spectrum. There was also a large rise in the intensity of the non-paracetamol C-C peak (magenta), and the appearance of an as yet unseen function at the high binding energy side of the carbonyl shoulder (green). This was attributed to beam damage in the Tergitol NP-9 ethoxylate chain. The remaining paracetamol peaks were amide (purple), carbonyl (blue), and hydroxyl (green).

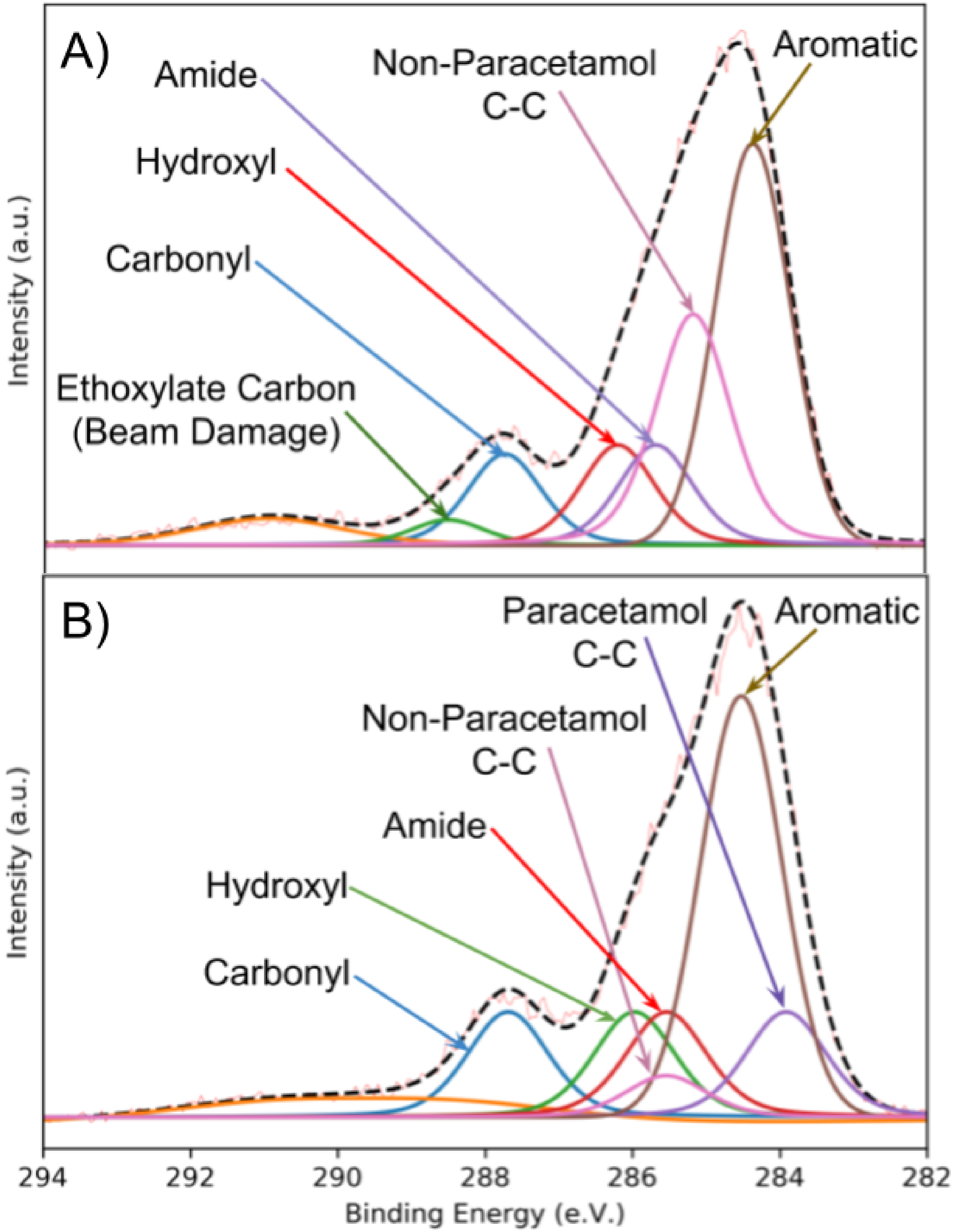

Figure 5.3: C1s XPS spectrum of paracetamol before (B) and after (A) exposure to Tergitol NP-9 at 1000 eV photon energy

Table 5.3: Fit parameters for Tergitol on paracetamol at 1000 eV

	Assignment (e.V.)	**Position (e.V.)**	**Relative Area (e.V.)**	**FWHM (e.V.)**
After Tergitol Exposure	C=O	287.7	1	1.2
	C-OH	286.2	1	1.2
	C-N	285.6	1	1.2
	C-C + Adventitious	285.1	2.5	1.2
	Aromatic	284.3	4	1.2
	C-C-O (Beam Damage)	288.5	0.3	1.2
Before Tergitol Exposure	C=O	287.7	1	1.3
	C-OH	286.0	1	1.3
	C-N	285.6	1	1.3
	C-C	283.9	1	1.3
	Adventitious	285.6	0.5	1.3
	Aromatic	284.5	4	1.3

5.4 Discussion

Figure 5.4 shows multiple plots of comparisons between paracetamol before and after exposure to Tergitol NP-9 at various photon energies. The spectra shown have been normalised to the intensity of the carbonyl carbon function. The spectra shown in blue are of paracetamol after Tergitol NP-9 exposure, while the spectra shown in red are of paracetamol before exposure. As can be seen, a reduction in photon energy (labelled), leads to a reduction in the level of paracetamol detected.The key message being that as the photon energy is decreased, Tergitol NP-9 makes up a much larger proportion of the spectrum than paracetamol. This is exactly what is expected from these experiments. Figure 5.5 shows the number of paracetamol molecules detected in spectra from samples that had been exposed to Tergitol NP-9. The red line represents a fit of the data. An exponential fit could be achieved with $R^2 = 0.968$. The equation for the fit being;

$$y = 3.92 \cdot e^{0.00521x} \tag{5.8}$$

which is again, the expected result from the experiments performed. Table 5.4 shows the calculated thickness of the paracetamol substrate and the Tergitol overlayer at various energies. The nonyl tail group of the Tergitol surfactant measures 10.3 Å when extended. The nine membered ethoxylate group is 31.5 Å. As can be seen from table 5.4 the maximum calculated depth at any photon energy was 1.9 Å. At higher photon energies, the IMFP of escaping carbon photoelectrons was much greater than the calculated layer thickness. This means it is highly unlikely that the configuration of Tergitol molecules adsorbed to the surface is of a linear nature, it is more likely that they are collapsed into globular coiled configuration. The separation between the carbon environments in pure Tergitol NP-9 was measured in chapter 3 and found to be 1.6 eV. In these experiments the separation between the carbon environments was much closer at 0.8 eV. The indication

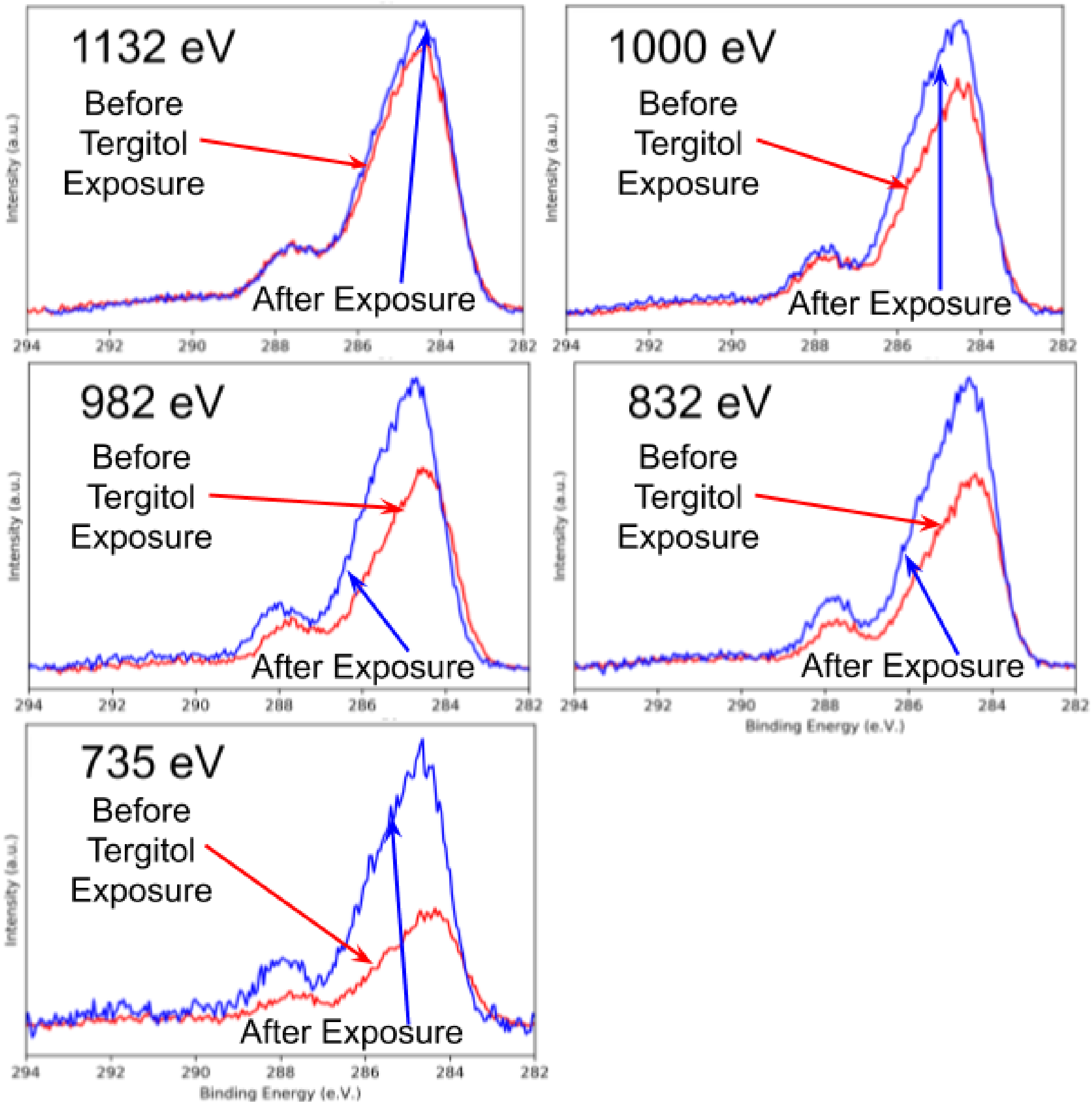

Figure 5.4: C1s XPS spectra at different photon energies before and after exposure to Tergitol NP-9

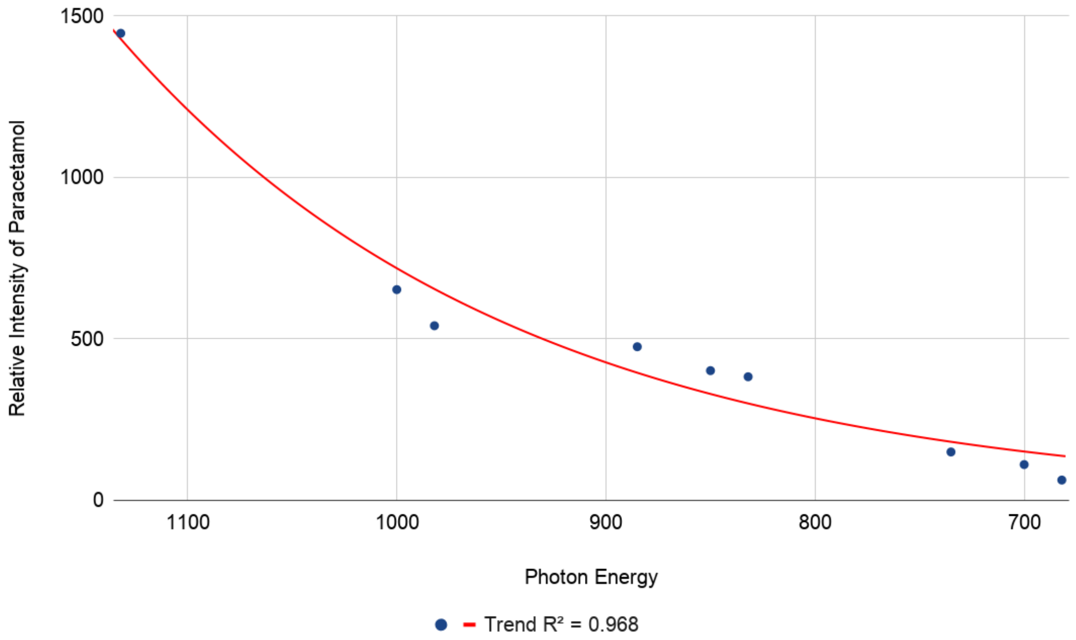

Figure 5.5: Graph Showing Number of Paracetamol Molecules vs. Photon Energy

here being that the oxygen atoms in the ethoxylate head group are hydrogen bonded to the water in the atmosphere. This is not dissimilar to so called "hydrophobic collapse" in protein molecules [121].

Table 5.4: Measured Surface Parameters

Photon Energy (e.V.)	**IMFP Paracetamol (nm)**	**Layer Thickness Paracetamol (Å)**	**IMFP Tergitol NP-9 (nm)**	**Layer Thickness Tergitol NP-9 (Å)**
1132	13.93	75.44	28.02	0.82
1000	12.61	66.46	24.83	1.02
982	12.43	65.26	24.39	1.06
885	11.43	58.85	21.98	1.27
850	11.07	56.56	21.10	1.35
832	10.88	55.41	20.65	1.40
735	9.85	49.25	18.12	1.70
700	9.47	47.08	17.24	1.83
682	9.27	45.98	16.76	1.90

5.5 Conclusions

Deposition of surfactant on the surface of the paracetamol single crystal was successful. Furthermore, the calculated ratio of Tergitol molecules present on the paracetamol surface was observed to increase exponentially and inversely proportional to the photon energy. This was the expected result and gives confidence in the data. In terms of the aims of this package of work, Tergitol NP-9 surfactant was detected at the surface of a paracetamol single crystal. The level of Tergitol NP-9 could also be quantified, with the sense check on the determined levels being the number of paracetamol molecules decreasing according to an exponential decay model, with decreasing photon energy. Furthermore, the Tergitol molecules were determined to be adsorbed to the crystal by the hydrophobic tail group, with the hydrophilic head group exposed to the aqueous atmosphere. In addition, this head group is likely to be in a coiled configuration, rather than an elongated configuration.

Chapter 6

General Discussion and Conclusions

The first data chapter was intended to provide a baseline against which all future experimental methodology and data analysis would be undertaken. It was considered by the author to be of paramount importance that an ultra clean paracetamol spectrum was obtained, and that the interpretation of this spectrum be fully backed up with theory. As later chapters attest, this was critical in developing a detailed understanding of surfactant adsorption at individual facets of paracetamol crystals. Indeed, it is likely that this will be critical for the through understanding of any surface phenomena on any organic compound. Vacuum deposition was shown to be an ideal method for the production of ultra clean organic samples. Whilst this was valuable, the method also suffers from serious limitations. First and foremost, if organic crystal surfaces of industrial interest are the subject of study, one cannot produce bulk commodity crystals using this method. Which also means that the spectra alone are of little value when used in comparison to those from specific facets. The reason for this, is that at individual facets of an organic crystal, there is no guarantee the the atomic ratios will be the same from one facet to another. There is even less guarantee that those ratios will be comparable to those determined from a vacuum deposited film. This is where theory must be used in the interpretation of the spectrum. For if the peaks in the vacuum deposited film can be rationally assigned, this understanding can then be translated to other spectra. In order to do this, atom centred density functional theory (DFT), the so called linear combination of atomic orbitals method (LCAO), was selected the most efficient method of generating useful results. It could be argued that for solid form calculations, plane-wave methods would be more appropriate. If information about bulk properties were sought, then this would indeed be a correct argument. In the case of this work however, it was the *edge* cases that were of interest. Quite literally in fact, given it is surface properties that are of interest. The results from chapter 2 were the interpretation of XPS peaks in the paracetamol spectra, aided by DFT. The DFT calculations had to be set up in such a way that they were representative of surface molecules, but not of the bulk properties of the system. The results from the XPS experiment showed that the aromatic peak could be found at 284.6 eV binding energy, the amide carbon at 285.1 eV, the hydroxyl carbon at 285.8

eV, and the methyl carbon at 283.6 eV. Initially, this was surprising, as the likelihood of a methyl carbon having greater electron density than an aromatic ring is low. This was initially thought to be an artefact of the data analysis, but further calculations involving the systematic removal of intermolecular interactions showed that when certain hydrogen bonds are missing from the crystal structure, the calculated binding energy of 1s electrons in the methyl carbon drops significantly, on the order of 1 eV. This is more representative of the surface structure, given that at the interface between the crystal surface and its surroundings, there will be molecules with unsatisfied intermolecular interactions. This is most obviously shown in the graph in figure 2.18. Chapter three builds on these results by determining whether or not it is possible to both adsorb a surfactant of interest, in this case the nonylphenl ethoxylate surfactant *Tergitol NP-9*, onto paracetamol for further analysis. A number of concentrations were used ranging from 0% (w/w) to 1.6% (w/w). These concentrations were all applied to paracetamol powders that had been carefully washed in paracetamol saturated ultra-pure water. The unwashed powder (as received) and neat liquid surfactant were also used for comparisons. As can be seen in figure 3.9 there was no correlation between the level of surfactant the crystals were exposed to, and the levels of carbon detected in the XPS spectra. This is also highlighted in an overlay of all normalised spectra (see figure 3.6). The concentration determined to have been the most appropriate for use in further study was that which resulted in the lowest ethoxylate carbon count. This was tied between the lowest Tergitol concentration used, and the highest. Therefore, the next factor used was that which resulted in the lowest C-C count. The 1.6% (w/w) Tergitol concentration was therefore decided to be the most appropriate. These results can be seen in figure 3.11. It should be pointed out at this stage, that by most appropriate, the meaning is, the most appropriate of those tested. It is entirely possible that an even higher concentration of tergitol may have lead to a more appropriate concentration. However, given the constraints of time and regents, this was not possible to test. The focus of chapter four, was the development of a method to clean the crystals. Typical methods of surface cleaning are inappropriate for samples such as paracetamol, as heating to temperatures in excess of 170°C causes the crystal to melt. Exposure to Ar sputtering damages the fragile surfaces, and controlled deposition of liquid surfactant is challenging under vacuum. This work was a collaborative effort involving the use of atomic force microscopy (AFM) for rapid screening of solvents. This was combined with XPS for a more detailed chemical analysis of the best candidate solvent identified by AFM.
The AFM work was done by Alexandru A. Moldovan, and a full description can be found in the PhD thesis 'Interfacial Interactions of Faceted Organic Crystals – An in-silico study with Atomic Force Microscopy'. [117]

The solvent that showed the most promise was dichloromethane (DCM), as this showed the least physical damage to the crystal when examined in the AFM. This was also the expected result, given the chemical nature of DCM and the knowledge that paracetamol shows extremely limited solubility in DCM [85], initial survey scans were carried out on the clean crystal to determine whether any residual DCM was depositing and adsorbing to the surface of the crystal. No chlorine peaks were detected in the survey spectra (200 eV binding energy). This showed that no DCM was present on the crystal after the cleaning process. Figures 4.6, 4.7 and 4.8, 4.9 show the C1s spectrum of paracetamol with more surface sensitive measurements in the case of the first two, and the more bulk sensitive in the case of the second two. These figures show that there is a marked reduction in adventitious carbon when comparing the post-DCM treated spectra, to those taken prior to cleaning. They also show that the methyl carbon at the low binding energy side of the envelope could be detected in the treated sample, and not in the untreated samples. The oxygen spectra show like results, in which the ratio of hydroxyl carbon to carbonyl carbon drops from 2:1 in the case of the pre-DCM treated samples, to the expected 1:1 in the DCM treated samples. The final data chapter brings together the preceding chapters. Whereby single crystals of paracetamol were exposed to 1.6% (w/w) Tergitol NP-9 aqueous mixture. The surfaces of which was cleaned following the procedures in chapter 4. The crystals were then analysed by NAP-XPS and the level of surfactant at the surface quantified by application of the layers on a plane model [120]. This is most aptly shown by figure 5.4, in which five spectral comparisons are made between crystals exposed to Tergitol NP-9 (blue spectra) and crystals prior to Tergitol exposure. The most bulk sensitive measurement made at 1132 eV photon energy, shows that there is some increase in the C1s intensity after exposure. As the photon energy decreases, and hence the surface sensitivity of the measurements increases, one can immediately see the decrease in paracetamol contributions, and the increase in Tergitol contributions. The total relative intensity from paracetamol molecules calculated using the layers on a plane model was then plotted against the photon energy used and an attempt made to fit an exponential function to these data. This yielded a fit of $y = 3.92 \cdot e^{0.00521x}$ with an R^2 value of 0.97. This was primarily a check step to ensure that data were in accordance with the expectation of an exponential decrease in the number of bulk molecules detected with decreasing photon energy. The mean relative intensity from Tergitol surface molecules was therefore computed to be 25 ± 2. This was with a range of 18. Given the lack of outliers and the large range, it is likely that the variation observed is due to the method of surfactant deposition. Furthermore, the configuration of the adsorbed Tergitol molecules was determined to be in a collapsed state on the surface of the paracetamol crystal, as opposed to an elongated state. With the adsorption occurring with the nonyl tail in contact with the paracetamol surface and the ethoxylate head group forming the interface with the environment.

The aim of this project was to determine if *The Detection and Quantification of Nonyl Phenyl Ethoxylate Surfactant on Paracetamol Single Crystal Surfaces* is possible to do by X-ray photoelectron spectroscopy (XPS).

This work has shown that it is indeed possible given some prior conditions are met. First and foremost, paracetamol, and indeed many organic crystalline compounds, are electrical insulators. Therefore some method of charge neutralisation is required in order to make use of XPS for these studies.

The method used in this work was principally gas ion pairing in a near-ambient pressure XPS instrument (NAP-XPS) [122] using either argon gas or water vapour.

Secondly, simply relying on tables in the literature or websites is insufficient for assigning peak positions, especially when fitting the components of a given peak, for example the carbon 1s peak. In order to do this accurately, it is essential that there be some grounding in theory for the assignment of these positions. Density functional theory (DFT), in this work proved essential to this use case. It must be strongly noted at this point, that attempting to geometry optimise the DFT input structure resulted in wildly incorrect outputs with respect to the real system.

Rather, until *ab initio* models are sufficiently advanced to the point that crystal structures of organic compounds can be calculated routinely, high quality structures must be provided to the DFT calculations as inputs. In this work, one of the principal reasons for the selection of paracetamol as a model compound, was the degree to which it has been previously characterised. Hence, high quality crystal structures already exist. When attempting these analyses on novel compounds, it is essential that this same characterisation work be carried out.

Finally, the specific chemical nature of the compound of interest may prove challenging in the removal of contaminants from the surface of the crystals. Should the material of interest be highly soluble in solvents such as DCM, this exact protocol will not be useful.

Chapter 7

Future Directions

In the first instance, a more robust method of surfactant deposition would likely lead to far less variable results in the quantification of that which was deposited. For example, the development of protocol using a langmuir trough for surfactant deposition.

Furthermore, the recent improvements in both the application and economic cost of gas cluster ion beam (GCIB) technology, may prove a valuable tool in the cleaning of organic crystal surfaces. It is the author's belief that this will open up an entire new avenue for the use of XPS analysis, and if successful, will bring its application evermore so into the development of formulated products, by allowing extreme high quality formation tailoring to aid in both the stability of formulated products and in bringing down the costs of manufacturing them.

This work should also lead into the analysis and development of protocols for more organic compound scenarios. For example, the use of ionic surfactants or other adsorbing materials, as well as the aforementioned crystals are that are not amenable to DCM cleaning. In effect, a new field of research, that of atomic resolution organic crystal surface analysis. New laboratory equipment, in the form of the EnviroESCA, and hopefully competitors have the potential to open up this nascent field to more and more researchers. Concurrently, interesting research into reducing the photon flux of modern synchrotron beamlines would be ideal. This would allow modern facilities to engage in organic crystal surface analysis more easily, and with less beam damage.

Furthermore, building on the density functional theory analyses presented in this work, and developing more rapid, more robust methodologies for generating computational models of organic surfaces should be explored. Along with this, there are additional techniques that could readily be used to complement the NAP-XPS and DFT analyses. The most obvious to the author being NEXAFS, this has already been explored to some extent in the development of this work, and by others in the SLMS lab [123].

Chapter 8

References

[1] E L Cussler and G D Moggridge. *Chemical Product Design*. Cambridge University Press, Cambridge, 2011.

[2] Johannes A Wesselingh, Soren Kill, and Martin E Vigild. *Design & Development of Biological, Chemical, Food and Phramaceutical Products*. Wiley, Chichester, 2007.

[3] R Flarend, T Bin, D Elmore, and S L Hem. A preliminary study of the dermal absorption of aluminium from antiperspirants using aluminium-26. *Food Chem. Toxicol.*, 39(2):163–168, February 2001.

[4] D F Swaile, L T Elstun, and K W Benzing. Clinical studies of sweat rate reduction by an over-the-counter soft-solid antiperspirant and comparison with a prescription antiperspirant product in male panelists. *Br. J. Dermatol.*, 166 Suppl(SUPPL.1):22–26, March 2012.

[5] G E Piérard, P Elsner, R Marks, P Masson, and M Paye. EEMCO guidance for the efficacy assessment of antiperspirants and deodorants. *Skin Pharmacol. Physiol.*, 16(5):324–342, August 2003.

[6] P&g. Annual report. Technical report, Cincinnati, 2016.

[7] Pfizer. Appendix a 2015 financial report. Technical report, New York, 2016.

[8] PPG Industries. Annual review 2015. Technical report, Pittsburgh, 2016.

[9] Syngenta. Our industry. Technical report, Basel, 2016.

[10] Unilever. Annual report and accounts 2015. Technical report, London, 2016.

[11] Nestle. Annual review 2015. Technical report, Vevey, 2016.

[12] Burkhard Hinz and Kay Brune. Paracetamol and cyclooxygenase inhibition: is there a cause for concern? *Ann. Rheum. Dis.*, 71(1):20–25, January 2012.

[13] Ying Hong, Fran M Gengo, Michelle M Rainka, Vernice E Bates, and Donald E Mager. Population pharmacodynamic modelling of aspirin- and Ibuprofen-Induced inhibition of platelet aggregation in healthy subjects. *Clin. Pharmacokinet.*, 47(2):129–137, 2008.

[14] Yihong Qiu, Yisheng Chen, Geoff G Z Zhang, Lawrence Yu, and Rao V Mantri. *Developing Solid Oral Dosage Forms: Pharmaceutical Theory and Practice*. Academic Press, November 2016.

[15] Cátia G Abrantes, Dinah Duarte, and Catarina P Reis. An overview of pharmaceutical excipients: Safe or not safe? *J. Pharm. Sci.*, 105(7):2019–2026, July 2016.

[16] Lillian C Becker, Ivan Boyer, Wilma F Bergfeld, Donald V Belsito, Ronald A Hill, Curtis D Klaassen, Daniel C Liebler, James G Marks, Ronald C Shank, Thomas J Slaga, Paul W Snyder, and F Alan Andersen. Safety assessment of alumina and aluminum hydroxide as used in cosmetics. *Int. J. Toxicol.*, 35(3_suppl):16S–33S, November 2016.

[17] Mohammad Azad, Colby Arteaga, Beshoy Abdelmalek, Rajesh Davé, and Ecevit Bilgili. Spray drying of drug-swellable dispersant suspensions for preparation of fast-dissolving, high drug-loaded, surfactant-free nanocomposites. *Drug Dev. Ind. Pharm.*, 41(10):1617–1631, October 2015.

[18] Kunkun Zhu, Ting Ye, Jinjin Liu, Zheng Peng, Shasha Xu, Jieqiong Lei, Hongbing Deng, and Bin Li. Nanogels fabricated by lysozyme and sodium carboxymethyl cellulose for 5-fluorouracil controlled release. *Int. J. Pharm.*, 441(1-2):721–727, January 2013.

[19] Sheree E Cross, Brian Innes, Michael S Roberts, Takuya Tsuzuki, Terry A Robertson, and Paul McCormick. Human skin penetration of sunscreen nanoparticles: In-vitro assessment of a novel micronized zinc oxide formulation. *Skin Pharmacol. Physiol.*, 20(3):148–154, January 2007.

[20] A P Popov, A V Priezzhev, J Lademann, and R Myllylä. TiO 2 nanoparticles as an effective UV-B radiation skin-protective compound in sunscreens. *J. Phys. D Appl. Phys.*, 38(15):2564–2570, August 2005.

[21] Matthew S Bennett, Frank Wien, John N Champness, Thilina Batuwangala, Thomas Rutherford, William C Summers, Hongmao Sun, George Wright, and Mark R Sanderson. Structure to 1.9 å resolution of a complex with herpes simplex virus type-1 thymidine kinase of a novel, non-substrate inhibitor: X-ray crystallographic comparison with binding of aciclovir. *FEBS Lett.*, 443(2):121–125, January 1999.

[22] Tharwat F Tadros. *Dispersion of Powders in Liquids and Stabilization of Suspensions*. Wiley-VCH Verlag GmbH & Co. KGaA, Weinheim, Germany, June 2012.

[23] T Young. An essay on the cohesion of fluids. *Philosophical Transactions of the Royal Society of London*, 95(0):65–87, January 1805.

[24] W A Zisman. Relation of the equilibrium contact angle to liquid and solid constitution. In F M Fowkes, editor, *Advances in Chemistry: Contact Angle, Wetability and Adhesion*, pages 1–51. ACS, Washington D.C., January 1964.

[25] Frederick M Fowkes. Attractive forces at interfaces. *Ind. Eng. Chem. Res.*, 56(12):40–52, December 1964.

[26] D K Owens and R C Wendt. Estimation of the surface free energy of polymers. *J. Appl. Polym. Sci.*, 13(8):1741–1747, August 1969.

[27] Jerry Y Y Heng and Daryl R Williams. Wettability of paracetamol polymorphic forms i and II. *Langmuir*, 22(16):6905–6909, 2006.

[28] Jerry Y Y Heng, Alexander Bismarck, Adam F Lee, Karen Wilson, and Daryl R Williams. Anisotropic surface energetics and wettability of macroscopic form I paracetamol crystals. *Langmuir*, 22(6):2760–2769, March 2006.

[29] J W Mullin. *Crystallization, Fourth Edition*. Butterworth-Heinemann, Oxford, 4 edition, 2001.

[30] Roger J Davey and John Garside. *From Molecules to Crystallizers*. Oxford University Press, Oxford, 2000.

[31] Tharwat F Tadros. *An Introduction to Surfactants*. DeGruyter, Berlin, 2014.

[32] Rui Zhang and P Somasundaran. Advances in adsorption of surfactants and their mixtures at solid/solution interfaces. *Adv. Colloid Interface Sci.*, 123-126:213–229, November 2006.

[33] Albert Thompson, David Attwood, Eric Gullikson, Malcolm Howells, Kwang-Je Kirn, Janos Kirz, Jeffery Kortright, Ingold Lindau, Yanwei Liu, Piero Pianetta, Arthur Robinson, James Scofield, James Underwood, Gwyn Williams, and Herman Winick. *X-ray Data Booklet*. Lawrence Berkeley National Laboratory, Berkley, CA, 3 edition, 2009.

[34] C Kunz. Synchrotron radiation: third generation sources. *J. Phys. Condens. Matter*, 13:7499–7510, 2001.

[35] K Wille. Synchrotron radiation sources. *Rep. Prog. Phys.*, 54(54), 1991.

[36] Donald H Bilderback, Pascal Elleaume, and Edgar Weckert. Review of third and next generation synchrotron light sources. *J. Phys. B At. Mol. Opt. Phys.*, 38(9):S773–S797, May 2005.

[37] Brookhaven National Laboratory.

[38] Michael C Hettrick. High resolution gratings for the soft x-ray. *Nucl. Instrum. Methods Phys. Res. A*, 266(1-3):404–413, April 1988.

[39] Robert Lawrence Johnson. Grazing-incidence diffraction gratings. *Nuclear Instruments and Methods*, 152(1):117–122, June 1978.

[40] M Neviere and J Flamand. Electromagnetic theory as it applies to x-ray and XUV gratings. *Nuclear Instruments and Methods*, 172(1-2):273–279, May 1980.

[41] Joachim Stöhr. *NEXAFS Spectroscopy*, volume 25 of *Springer Series in Surface Sciences*. Springer Berlin Heidelberg, Berlin, Heidelberg, 1992.

[42] Akihiro Koide, Takashi Fujikawa, and Nobuyuki Ichikuni. Recent progress in EXAFS/NEXAFS spectroscopy. *J. Electron Spectrosc. Relat. Phenom.*, 195:375–381, 2014.

[43] Kathrin M Lange, E Suljoti, and Emad F Aziz. Electronic structure of ions and molecules in solution: a view from modern soft x-ray spectroscopies. *Chem. Soc. Rev.*, 42(16):6840, 2013.

[44] John C. Vickerman and Ian Gilmore. *Surface Analysis - The Principal Techniques*. John Wiley & Sons, Ltd, Chichester, UK, April 2009.

[45] Iupac. *IUPAC Compendium of Chemical Terminology*. IUPAC, Research Triagle Park, NC, June 2009.

[46] Pierre Victor Auger. Sur les reyons B secondaires produits dans un gaz par des reyons X. *Comptes Rendues Hebdomadaires des Seances de l'Academie des Sciences*, 180:65–68, 1925.

[47] Marc F Tesch, Ronny Golnak, Felix Ehrhard, Daniela Schoen, Jie Xiao, Kaan Atak, Annika Bande, and Emad F Aziz. Analysis of the electronic structure of aqueous urea and its derivatives: A systematic soft X-Ray TD-DFT approach. *Chemistry - A European Journal*, 22(34):12040–12049, 2016.

[48] Georg Hähner. Near edge x-ray absorption fine structure spectroscopy as a tool to probe electronic and structural properties of thin organic films and liquids. *Chem. Soc. Rev.*, 35(12):1244–1255, 2006.

[49] Heiko Wende. Recent advances in x-ray absorption spectroscopy. *Rep. Prog. Phys.*, 67:2105–2181, 2004.

[50] Frank Neese. The ORCA program system. *Wiley Interdiscip. Rev. Comput. Mol. Sci.*, 2(1):73–78, January 2012.

[51] M Valiev, E J Bylaska, N Govind, K Kowalski, T P Straatsma, H J J Van Dam, D Wang, J Nieplocha, E Apra, T L Windus, and W A de Jong. NWChem: A comprehensive and scalable open-source solution for large scale molecular simulations. *Comput. Phys. Commun.*, 181(9):1477–1489, September 2010.

[52] Kai Siegbahn. Electron spectroscopy for atoms, molecules, and condensed matter. *Proceedings of the Physical Society. Section A*, 63(9):960–986, September 1950.

[53] M P Seah and W A Dench. Quantitative electron spectroscopy of surfaces: A standard data base for electron inelastic mean free paths in solids. *Surf. Interface Anal.*, 1(1):2–11, February 1979.

[54] D A Shirley. High-Resolution X-Ray photoemission spectrum of the valence bands of gold. *Phys. Rev. B: Condens. Matter Mater. Phys.*, 5(12):4709–4714, June 1972.

[55] J T Grant. Methods for quantitative analysis in XPS and AES. *Surf. Interface Anal.*, 14(6-7):271–283, June 1989.

[56] J J Yeh and I Lindau. Atomic subshell photoionization cross sections and asymmetry parameters: 1 ¡ Z ¡ 103. *At. Data Nucl. Data Tables*, 32(1):1–155, January 1985.

[57] Mark J Jackman, Andrew G Thomas, and Chris Muryn. Photoelectron spectroscopy study of stoichiometric and reduced anatase TiO 2 (101) surfaces: The effect of subsurface defects on water adsorption at Near-Ambient pressures. *J. Phys. Chem. C*, 119(24):13682–13690, June 2015.

[58] Alexander Yu Klyushin, Tulio C R Rocha, Michael Hävecker, Axel Knop-Gericke, and Robert Schlögl. A near ambient pressure XPS study of au oxidation. *Phys. Chem. Chem. Phys.*, 16(17):7881, 2014.

[59] V V Kaichev, G Ya Popova, Yu A Chesalov, A A Saraev, D Y Zemlyanov, S A Beloshapkin, A Knop-Gericke, R Schlögl, T V Andrushkevich, and V I Bukhtiyarov. Selective oxidation of methanol to form dimethoxymethane and methyl formate over a monolayer V2O5/TiO2 catalyst. *J. Catal.*, 311:59–70, March 2014.

[60] T Kendelewicz, S Kaya, J T Newberg, H Bluhm, N Mulakaluri, W Moritz, M Scheffler, A Nilsson, R Pentcheva, and G E Brown. X-ray photoemission and density functional theory study of the interaction of water vapor with the fe 3 O 4 (001) surface at Near-Ambient conditions. *J. Phys. Chem. C*, 117(6):2719–2733, February 2013.

[61] Adéla Křepelová, Thorsten Bartels-Rausch, Matthew A Brown, Hendrik Bluhm, and Markus Ammann. Adsorption of acetic acid on ice studied by Ambient-Pressure XPS and Partial-Electron-Yield NEXAFS spectroscopy at 230–240 K. *J. Phys. Chem. A*, 117(2):401–409, January 2013.

[62] Koji Honda, Masamichi Morita, Hideyuki Otsuka, and Atsushi Takahara. Molecular aggregation structure and surface properties of poly(fluoroalkyl acrylate) thin films. *Macromolecules*, 38(13):5699–5705, June 2005.

[63] Joanna S Stevens, Stephen J Byard, Evgeny Zlotnikov, and Sven L M Schroeder. Detection of free base surface enrichment of a pharmaceutical salt by x-ray photoelectron spectroscopy (XPS). *J. Pharm. Sci.*, 100(3):942–948, March 2011.

[64] Peter J. Cumpson, Martin P. Seah, and Steve J. Spencer. Calibration of auger and x-ray photoelectron spectrometers for valid analytical measurements. 1998.

[65] ISO 15472:2010(en). Surface chemical analysis - x-ray photoelectron spectrometers - calibration of energy scales. Technical report, International Organization for Standardization, May 2010.

[66] G. Greczynski and L. Hultman. X-ray photoelectron spectroscopy: Towards reliable binding energy referencing. *Progress in Materials Science*, 107:100591, 2020.

[67] Grzegorz Greczynski and Lars Hultman. Reliable determination of chemical state in x-ray photoelectron spectroscopy based on sample-work-function referencing to adventitious carbon: Resolving the myth of apparent constant binding energy of the C 1s peak. *Appl. Surf. Sci.*, 451:99–103, 2018.

[68] Grzegorz Greczynski and Lars Hultman. C 1s peak of adventitious carbon aligns to the vacuum level: Dire consequences for material's bonding assignment by photoelectron spectroscopy. *Chemphyschem*, 18(12):1507–1512, June 2017.

[69] Sabrina Tardio and Peter J Cumpson. Practical estimation of XPS binding energies using widely available quantum chemistry software. *Surf. Interface Anal.*, 50(1):5–12, January 2018.

[70] M P Seah. Xps reference procedure for the accurate intensity calibration of electron spectrometers - results of a bcr intercomparison co-sponsored by the vamas sca twa. *Surf. Interface Anal.*, 20(3):243–266, March 1993.

[71] P J Cumpson, M P Seah, and S J Spencer. Simple procedure for precise peak maximum estimation for energy calibration in aes and xps. *Surf. Interface Anal.*, 24(10):687–694, 1996.

[72] W Smekal W. S. M. Werner and C J Powell. *Simulation of Electron Spectra for Surface Analysis (SESSA) - 2.1.1.* National Institute of Standards and Technology, 2018.

[73] C Scheuerlein and M Taborelli. The assessment of metal surface cleanliness by XPS. *Appl. Surf. Sci.*, 252(12):4279–4288, April 2006.

[74] J D Herbert and R J Reid. A study of cleaning agents for stainless steel for ultra high vacuum use. part 2: ESD results. *Vacuum*, 47(6):693–695, June 1996.

[75] K J Middleman, J D Herbert, and R J Reid. Cleaning stainless steel for use in accelerators—phase 1. *Vacuum*, 81(6):793–798, February 2007.

[76] Erik Brachmann, Marietta Seifert, Steffen Oswald, Siegfried B Menzel, and Thomas Gemming. Evaluation of surface cleaning procedures for CTGS substrates for SAW technology with XPS. *Materials*, 10(12), November 2017.

[77] R V Ghita, C Logofatu, C Negrila, A S Manea, M Cernea, V Ciupina, and M F Lazarescu. XPS study of ti/oxidized GaAs interface. *J. Optoelectron. Adv. Mater.*, 8(1):31, 2006.

[78] Ramón Escobar Galindo, Raul Gago, David Duday, and Carlos Palacio. Towards nanometric resolution in multilayer depth profiling: a comparative study of RBS, SIMS, XPS and GDOES. *Anal. Bioanal. Chem.*, 396(8):2725–2740, April 2010.

[79] Rong Yan, Lucas Moser, Baoguo Wang, Jiao Peng, Christian Vorpahl, Frank Leipold, Roger Reichle, Rui Ding, Junling Chen, Lei Mu, Roland Steiner, Ernst Meyer, Mingzhong Zhao, Jinhua Wu, and Laurent Marot. Plasma cleaning of ITER edge thomson scattering mock-up mirror in the EAST tokamak. *Nucl. Fusion*, 58(2):026008, December 2017.

[80] L Moser, L Marot, R Steiner, M Newman, A Widdowson, D Ivanova, J Likonen, P Petersson, G Pintsuk, M Rubel, E Meyer, and JET Contributors. Plasma cleaning of beryllium coated mirrors. *Phys. Scr.*, 2016(T167):014069, January 2016.

[81] H Y Yu, X D Feng, D Grozea, Z H Lu, R N S Sodhi, A-M Hor, and H Aziz. Surface electronic structure of plasma-treated indium tin oxides. *Appl. Phys. Lett.*, 78(17):2595–2597, April 2001.

[82] Michitaka Yamamoto, Takashi Matsumae, Yuichi Kurashima, Hideki Takagi, Tadatomo Suga, Toshihiro Itoh, and Eiji Higurashi. Comparison of argon and oxygen plasma treatments for ambient Room-Temperature Wafer-Scale Au-Au bonding using ultrathin au films. *Micromachines (Basel)*, 10(2), February 2019.

[83] S Yamamoto, H Bluhm, K Andersson, G Ketteler, H Ogasawara, M Salmeron, and A Nilsson. In situ x-ray photoelectron spectroscopy studies of water on metals and oxides at ambient conditions. *J. Phys. Condens. Matter*, 20(18):184025, May 2008.

[84] M P Seah and S J Spencer. Ultrathin SiO 2 on si. i. quantifying and removing carbonaceous contamination. *J. Vac. Sci. Technol. A*, 21(2):345–352, 2003.

[85] Roger A Granberg, A C Rasmuson, and Åke C Rasmuson. Solubility of paracetamol in pure solvents. *J. Chem. Eng. Data*, 44(6):1391–1395, 1999.

[86] C Sudha and K Srinivasan. Supersaturation dependent nucleation control and separation of mono, ortho and unstable polymorphs of paracetamol by swift cooling crystallization technique. *CrystEngComm*, 15(10):1914–1921, 2013.

[87] Y Nakai, M S Zei, D M Kolb, and G Lehmpfuhl. A LEED and RHEED investigation of cu on au(111) in the underpotential region. *Berichte der Bunsengesellschaft f?r physikalische Chemie*, 88(4):340–345, April 1984.

[88] T E Oliphant. Python for scientific computing. *Computing in Science Engineering*, 9(3):10–20, May 2007.

[89] Eric Jones, Travis Oliphant, Pearu Peterson, and Others. SciPy: Open source scientific tools for Python.

[90] S van der Walt, S C Colbert, and G Varoquaux. The NumPy array: A structure for efficient numerical computation. *Computing in Science Engineering*, 13(2):22–30, March 2011.

[91] Wes McKinney. Data structures for statistical computing in python. In Stéfan van der Walt and Jarrod Millman, editors, *Proceedings of the 9th Python in Science Conference*, pages 51–56, 2010.

[92] J D Hunter. Matplotlib: A 2D graphics environment. *Computing in Science Engineering*, 9(3):90–95, May 2007.

[93] M Jung, U Baston, T Porwol, H J. Freund, and E Umbach. The XPS peak structure of condensed aromatic anhydrides and imides. August 2004.

[94] Hamizah Mohd Zaki. *Spectroscopy Surface Analysis of Paracetamol and Paracetamol and Excipient Systems*. PhD thesis, (THESIS) University of Manchester, 2011.

[95] Jerry Y Y Heng, Alexander Bismarck, and Daryl R Williams. Anisotropic surface chemistry of crystalline pharmaceutical solids. *AAPS PharmSciTech*, 7(4):E12–E20, December 2006.

[96] Frank H Allen. The cambridge structural database: a quarter of a million crystal structures and rising. *Acta Crystallogr. B*, 58(3):380–388, June 2002.

[97] Joanna M Bąk, Paulina M Dominiak, Chick C Wilson, and Krzysztof Woźniak. Experimental charge-density study of paracetamol – multipole refinement in the presence of a disordered methyl group. *Acta Crystallogr. A*, 65(6):490–500, November 2009.

[98] Clare F Macrae, Ian J Bruno, James A Chisholm, Paul R Edgington, Patrick McCabe, Elna Pidcock, Lucia Rodriguez-Monge, Robin Taylor, Jacco van de Streek, and Peter A Wood. Mercury CSD 2.0 – new features for the visualization and investigation of crystal structures. *J. Appl. Crystallogr.*, 41(2):466–470, April 2008.

[99] Marcus D Hanwell, Donald E Curtis, David C Lonie, Tim Vandermeersch, Eva Zurek, and Geoffrey R Hutchison. Avogadro: an advanced semantic chemical editor, visualization, and analysis platform. *J. Cheminform.*, 4(1):17, 2012.

[100] Marcel Giesbers, Antonius T M Marcelis, and Han Zuilhof. Simulation of XPS c1s spectra of organic monolayers by quantum chemical methods. *Langmuir*, 29(15):4782–4788, April 2013.

[101] Florian Weigend and Reinhart Ahlrichs. Balanced basis sets of split valence, triple zeta valence and quadruple zeta valence quality for H to rn: Design and assessment of accuracy. *Phys. Chem. Chem. Phys.*, 7(18):3297, 2005.

[102] Stefan Grimme, Jens Antony, Stephan Ehrlich, and Helge Krieg. A consistent and accurate ab initio parametrization of density functional dispersion correction (DFT-D) for the 94 elements H-Pu. *J. Chem. Phys.*, 132(15), 2010.

[103] Frank Neese, Frank Wennmohs, Andreas Hansen, and Ute Becker. Efficient, approximate and parallel Hartree–Fock and hybrid DFT calculations. a 'chain-of-spheres' algorithm for the Hartree–Fock exchange. *Chem. Phys.*, 356(1-3):98–109, February 2009.

[104] Paolo Giannozzi, Stefano Baroni, Nicola Bonini, Matteo Calandra, Roberto Car, Carlo Cavazzoni, Davide Ceresoli, Guido L Chiarotti, Matteo Cococcioni, Ismaila Dabo, Andrea Dal Corso, Stefano de Gironcoli, Stefano Fabris, Guido Fratesi, Ralph Gebauer, Uwe Gerstmann, Christos Gougoussis, Anton Kokalj, Michele Lazzeri, Layla Martin-Samos, Nicola Marzari, Francesco Mauri, Riccardo Mazzarello, Stefano Paolini, Alfredo Pasquarello, Lorenzo Paulatto, Carlo Sbraccia, Sandro Scandolo, Gabriele Sclauzero, Ari P Seitsonen, Alexander Smogunov, Paolo Umari, and Renata M Wentzcovitch. QUANTUM ESPRESSO: a modular and open-source software project for quantum simulations of materials. *J. Phys. Condens. Matter*, 21(39):395502, September 2009.

[105] Stewart J Clark, Matthew D Segall, Chris J Pickard, Phil J Hasnip, Matt I J Probert, Keith Refson, and Mike C Payne. First principles methods using CASTEP. *Zeitschrift für Kristallographie - Crystalline Materials*, 220(5/6):191, January 2005.

[106] D Vanderbilt. Soft self-consistent pseudopotentials in a generalized eigenvalue formalism. *Phys. Rev. B Condens. Matter*, 41(11):7892–7895, April 1990.

[107] Joanna S Stevens, Stephen J Byard, Colin C Seaton, Ghazala Sadiq, Roger J Davey, and Sven L M Schroeder. Proton transfer and hydrogen bonding in the organic solid state: a combined XRD/XPS/ssNMR study of 17 organic acid-base complexes. *Phys. Chem. Chem. Phys.*, 16(3):1150–1160, 2014.

[108] Joanna S Stevens, Che R Seabourne, Cherno Jaye, Daniel A Fischer, Andrew J Scott, and Sven L M Schroeder. Incisive probing of intermolecular interactions in molecular crystals: Core level spectroscopy combined with density functional theory. *J. Phys. Chem. B*, 118(42):12121–12129, 2014.

[109] M J Thomason, C R Seabourne, B M Sattelle, G A Hembury, J S Stevens, A J Scott, E F Aziz, and S L M Schroeder. Self-association of organic solutes in solution: a NEXAFS study of aqueous imidazole. *Faraday Discuss.*, 179:269–289, 2015.

[110] K Schwarz, P Mohn, V L Sliwko, and P Blaha. Calculations for martensitic phase transformations by quantum mechanics and thermodynamics. *Le Journal de Physique IV*, 05(C2):C2–47–C2–52, February 1995.

[111] Roberto Dovesi, Alessandro Erba, Roberto Orlando, Claudio M Zicovich-Wilson, Bartolomeo Civalleri, Lorenzo Maschio, Michel Rérat, Silvia Casassa, Jacopo Baima, Simone Salustro, and Bernard Kirtman. Quantum-mechanical condensed matter simulations with CRYSTAL. *WIREs Comput Mol Sci*, 8(4):e1360, July 2018.

[112] Nouzha Bouhmaida, François Bonhomme, Benoît Guillot, Christian Jelsch, and Nour Eddine Ghermani. Charge density and electrostatic potential analyses in paracetamol. *Acta Crystallogr. B*, 65(3):363–374, June 2009.

[113] DOW Chemical Company. *TERGITOL NP-9 - Technical Data Sheet*, November 2019.

[114] Stuart Davidson. A review of surface contamination and the stability of standard masses. *Metrologia*, 40(6):324, November 2003.

[115] Shannon B Hill, Nadir S Faradzhev, and Cedric J Powell. Quantitative analysis of trace levels of surface contamination by x-ray photoelectron spectroscopy part i: statistical uncertainty near the detection limit. *Surf. Interface Anal.*, 49(12):1187–1205, December 2017.

[116] Nadir S Faradzhev, Shannon B Hill, and Cedric J Powell. Quantitative analysis of trace levels of surface contamination by x-ray photoelectron spectroscopy. part II: Systematic uncertainties and absolute quantification. *Surf. Interface Anal.*, 49(12):1214–1224, December 2017.

[117] Alexandru A Moldovan. *Interfacial Interactions of Faceted Organic Crystals – An in-silico study with Atomic Force Microscopy*. PhD thesis, University of Leeds, 2019.

[118] Frank A Momany. Determination of partial atomic charges from ab initio molecular electrostatic potentials. application to formamide, methanol, and formic acid. *J. Phys. Chem.*, 82(5):592–601, 1978.

[119] Thomas Fransson, Yoshihisa Harada, Nobuhiro Kosugi, Nicholas A Besley, Bernd Winter, John J Rehr, Lars G M Pettersson, and Anders Nilsson. X-ray and electron spectroscopy of water. *Chem. Rev.*, 116(13):7551–7569, July 2016.

[120] P. J. Cumpson and M. P. Seah. Elastic scattering corrections in aes and xps. ii. estimating attenuation lengths and conditions required for their valid use in overlayer/substrate experiments. *Surface and Interface Analysis*, 25(6):430–446, 1997.

[121] Mateusz Banach, Piotr Fabian, Katarzyna Stapor, Leszek Konieczny, Roterman, and Irena. Structure of the hydrophobic core determines the 3D protein Structure-Verification by single mutation proteins. *Biomolecules*, 10(5), May 2020.

[122] D. A. Moncrieff, V. N. E. Robinson, and L.B. Harris. Charge neutralisation of insulating surfaces in the sem by gas ionisation. *Journal of Physics D: Applied Physics*, 11(17):2315–2325, dec 1978.

[123] Laila Al-Madhagi. *Core Level Spectroscopy of Organic Systems - Experimental Studies and Development of Data Analysis Techniques*. PhD thesis, University of Leeds, 2019.